The Dissertation Committee for Egleide Yaneth Elenes Certifies that this is the approved version of the following dissertation:

An Arborizing, Multiport Catheter for Maximizing Drug Distribution in the Brain via Convection Enhanced Delivery

Committee:

Christopher G. Rylander, Supervisor

Manuel K. Rausch

John Rossmeisl

James W. Tunnell

Thomas Yankeelov

An Arborizing, Multiport Catheter for Maximizing Drug Distribution in the Brain via Convection Enhanced Delivery

by

Egleide Yaneth Elenes

Dissertation

Presented to the Faculty of the Graduate School of

The University of Texas at Austin

in Partial Fulfillment

of the Requirements

for the Degree of

Doctor of Philosophy

The University of Texas at Austin

August 2018

Dedication

To Cristian and Adelyn. May the doors be wide open for you, your future cousins and all the future generations to come.

Acknowledgements

I am forever grateful for the many blessings that God has granted me and for the strength to complete this journey. It's been a huge blessing to have the loving support of my family and friends every step of the way. Victor, you're next! Thank you for being my biggest supporter these past nine months and for gifting me a "best-case-scenario" to strive for. Thank you to the many members of the SHCC community that opened their hearts to me and gave me a second home. Especially, thank you Eva for your friendship and prayers. I also want to thank Chris and Jason for helping me problem-solve when I got stuck, for listening to my concerns, and for their overall camaraderie and moral support, which motivated me to keep pushing forward.

To my advisor, Dr. Christopher Rylander, thank you for offering me the opportunity to relocate to UT and for your direction, technical expertise and encouragement throughout my work. I am very appreciative of my committee members, Dr. Manuel Rausch, Dr. John Rossmeisl, Dr. Thomas Yankeelov and Dr. James Tunnell for their efforts and contribution to this research. Specifically, thank you to Dr. Rausch for his mentoring, patience and enthusiastic involvement that was the impetus for the progress of the computational work. Dr. Rossmeisl's invaluable instruction undoubtedly saved me many futile trials and made the animal tissue experiments possible. Thank you to Dr. Matthew Colbert, David Edey and Dr. Jessie Maisano at UTCT for all their help and for scanning the specimens. Additionally, I am very grateful to Dr. Waldemar Debinski for believing in the arborizing catheter and coordinating the efforts that led to the the National Institute of Health/ National Cancer Institute grant that supported this research.

An Arborizing, Multiport Catheter for Maximizing Drug Distribution in the Brain via Convection Enhanced Delivery

Egleide Yaneth Elenes, PhD

The University of Texas at Austin, 2018

Supervisor: Christopher G. Rylander

Glioblastoma (GBM) is a high-grade malignant glioma with a mortality rate that exceeds 95% despite over eight decades of medical research dedicated to improve outcomes. GBM is extremely difficult to treat and practically incurable with standard treatment involving surgical resection, radiation, concomitant and/or adjuvant chemotherapy. Therefore, convection enhanced delivery (CED) was developed to improve therapeutic outcomes. CED involves intraparenchymal delivery of drugs into diseased tissue via a small catheter. CED has proven to bypass the blood brain barrier and achieve better drug distribution than diffusion-based therapies. Nevertheless, the large volumes necessary to target entire tumors and peritumor volumes have been previously unachievable with currently-available catheters.

This dissertation describes the development of a multiport, arborizing catheter designed specifically for improving drug distribution in the brain. The performance of early-stage arborizing catheter prototypes was compared to single-port catheters in infusion studies using agarose brain phantoms. Volume dispersed (V_d) and mean distribution ratios (V_d:V_i) were quantified and compared between the two catheters. The arborizing catheter produced higher V_d values; however, it did not exhibit the greatest V_d:V_i, likely due to overlapping distribution volumes from the multiple individual ports.

Following infusion in brain phantoms, a biotransport study of the arborizing catheter was conducted using a multiphasic finite element framework. The model was used to predict dispersion volume of a solute in a permeable hyperelastic solid matrix as a function of separation distance between adjacent ports. Results show that increasing port distance can increase V_d; however, infusion time also increases significantly with greater port distance. One way to mitigate increased infusion times is to employ higher infusion flow rates.

Finally, the performance of improved arborizing catheters was compared to reflux-preventing single-port catheters in excised pig brains. CT scans were used to quantify V_d and V_d:V_i of infused iohexol (contrast-enhancing agent). The average volume dispersed for the arborizing catheter was 5.8 times greater than the single-port catheter. Mean distribution ratios for both catheters were similar. Using the multiple ports of the arborizing catheter, high V_d was achieved at a low infusion rate with negligible reflux. Given that previous attempts of CED reported poor drug distribution, the arborizing catheter may help overcome the limitations of CED.

Table of Contents

List of Tables

List of Figures

Chapter 1: Introduction and Overview

MOTIVATION

Cancer remains the number two killer in modern society [1]. Each year in the United States, 600 thousand deaths are caused by cancer. The Center for Disease Control National Health Report predicts that due to the steady increase in deaths associated with cancer, it will soon dethrone heart disease as the leading cause of death [1, 2]. Yet, advances in medical technology have contributed to significantly reducing overall national mortality rates for the most common types of cancers including breast, lung, prostrate and colorectal cancers. However, since the war on cancer, marked by the inauguration of the National Cancer Institute 80 years ago, the landscape concerning malignant brain tumors has remained relatively unaltered. Brain and central nervous system (CNS) cancers are increasing by an average of 0.5% annually [3]. For glioblastoma (GBM), the most aggressive and unfortunately the most common type of brain tumor, median overall survival (OS) is 12 to 15 months [4], with five-year survival rates of less than 5% [5]. Standard treatment consists of surgery, radiation and chemotherapy; however, it remains palliative at best, as recurrence is inevitable [6-8]. Despite the many years of research and resources dedicated to GBM and other brain cancers, the discovery of effective treatment modalities remains an unmet clinical need.

PRIMARY MALIGNANT BRAIN TUMORS

Epidemiology

Brain tumors can be defined as a collection of intracranial neoplasms, predominantly arising from brain tissue [9]. Each year in the United States, the number of newly diagnosed cases of primary malignant brain and other nervous system cancer is ~ 7.0 per 100,000 people, of which gliomas are the most common [3, 10]. Gliomas are tumors of the CNS arising from glial cells as well as their precursors. Ependymomas emerge from ependymal cells, which line the ventricular spaces of the brain and spine. These cells create and circulate cerebrospinal fluid (CSF). Oligodendrogliomas arise from oligodendrocytes, which normally function to produce myelin and improve nervous signaling via insulating neuronal axons. Astrocytomas originate from astrocytes, the cells that are responsible for providing nutrients to the surrounding neurons. These cells are part of the neurovascular protective unit that forms the blood brain barrier (BBB) [11]. The most common sites for gliomas are the frontal, temporal and parietal lobes (Figure 1.1).

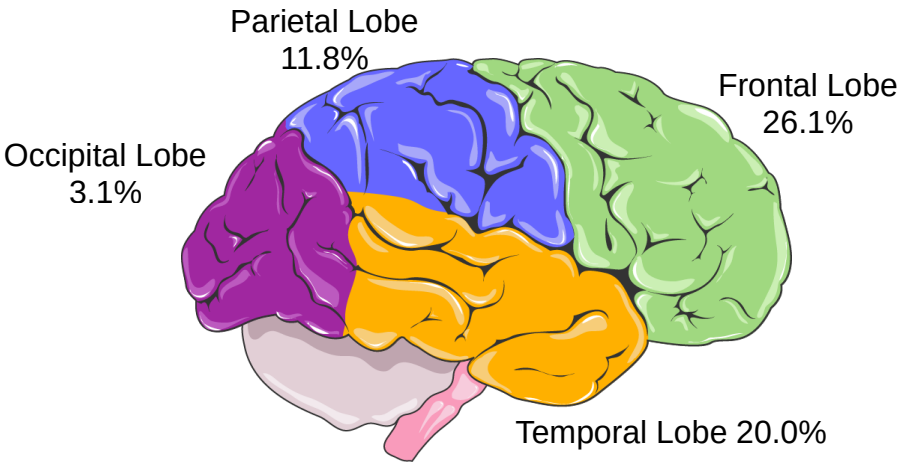

Figure 1.1: Common sites of gliomas. Data from CBTRUS Statistical Report [5]. This figure was developed using Servier Medical Art under a Creative Commons attributi0n 2.0 Unported License (https://smart.servier.com/smart_image/brain-15/).

Unlike other cancers, brain tumors are not classified by staging, but rather the World Health Organization (WHO) classifies CNS tumors using a grade system from grade I-IV based on histopathology [5]. Anaplastic astrocytoma (grade III) and GBM (grade IV) are considered malignant gliomas (MGs) [4]. The most common MG is GBM, accounting for 60-70% overall [5], followed by anaplastic astrocytomas (AA) at 10-15%, anaplastic oligodendrogliomas and anaplastic oligoastrocytomas at 10%. The remaining MGs consist of much rarer tumors such as anaplastic ependymomas and anaplastic gangliogliomas [4]. For AA, the expected age of onset ranges from 40-50 years, while GBM present later in life, around 60-70 years [9]. The underlying cause of MGs is unknown, and the only established risk factor is prior exposure to ionizing radiation (even at low doses), particularly in childhood, for treatment of an unrelated disease [12-14].

The incidence of MGs is increasing slightly, especially in the elderly. This is most likely attributed to improved diagnostic methods [4], better access to healthcare [13] and improved healthcare that has extended life span allowing for the emergence of brain tumors in the elderly [9]. Prevalence of MGs is 40% higher in men than in women [13]. The incidence of GBM in Caucasians are two-times greater than in blacks and higher in non-Hispanics (3.26 per 100,000) than in Hispanics (2.42 per 100,000).

Symptoms

Symptoms commonly associated with MGs include headaches, seizures, loss of consciousness, confusion, memory loss and personality changes [4, 15]. Although presentation and type of symptoms vary with type and location of the tumor, progression of symptoms is often inevitable [10]. Especially during the last week of life, manifestation of symptoms and neurological deficiency increase dramatically [16]. For

focal manifestations of the disease, neurological deficits are associated with the region of the tumor and can include hemiparesis or aphasia (i.e. inability to speak) [17]. Edema (i.e. swelling) surrounding the tumor mass can increase with tumor growth, and this mass effect can lead to headaches, visual obscurations and lightheadedness associated with increased intracranial pressure [10].

Diagnosis

Computer tomography (CT) or magnetic resonance imaging (MRI) with gadolinium enhancement is used to diagnose MGs, and can demonstrate a heterogeneously enhancing mass surrounded by edema [9]. GBMs frequently exhibit a necrotic core surrounded by more extensive peritumoral edema, hyper-vascularity, and tumor cell proliferation compared to anaplastic gliomas [4]. Enhancement of the tumor by leakage of the contrast agent through the BBB is common in MGs, such as GBM, however, about one-third of MGs are non-enhancing [10].

Although contrast-enhanced MRI can imply distinct tumor margins typically involving white matter, the tumors can be highly infiltrative and diffuse. Commonly, extension of the tumor beyond the apparent border are non-enhancing in MRI. GBM cells use surrounding blood vessels and white matter tracts to migrate several centimeters into the surrounding healthy brain tissue [11, 18]. In some cases, tumor cells can infiltrate throughout the entire hemisphere or spread across corpus callosum to the contralateral hemisphere [9]. These infiltrative malignant cells are believed to be responsible for recurrence, which typically occur within 1-2 centimeters (cm) of the original tumor site [19]. However, MRI is limited in accurately differentiating between recurrence of the tumor and tumor response to treatment. Final tissue diagnosis can be obtained with a

stereotactic biopsy, which can be taken at the time of surgical resection, or can be performed as a standalone procedure if the tumor cannot be safely resected [10].

Prognosis

In general, older age at diagnosis is associated with the poorer prognosis. Mean OS, post-diagnosis, ranges from 4.3 months, without treatment, to 7.5 months with surgery and radiation and 12.5 months with the addition of chemotherapy [11]. Due to the nature of the disease involving one of the most important organs of the body, its complex pathobiology, and highly infiltrative form, GBM is extremely difficult to treat and essentially incurable [20]. Less than 5% of patients with GBM reach the five-year survival mark [5]. Due to the dismal outcome for GBM patients, various investigations have studied the prognostic determinants of GBM and have found that factors such as > 55 years of age, poor Karnofsky Performance Status (KPS) scores (< 70), unresectable tumors, greater residual tumor volume, larger preoperative tumor size and greater necrosis shown on MRI are linked with poor prognosis [9, 21-23]. In addition, greater OS (17 months) was reported for patients with tumors located in the frontal lobe (11.4 months), compared to those with tumors in the temporal lobe (9.1 months) or parietal lobe (9.6 months), implying anatomical location may also be a prognostic factor [24].

Treatment

In newly diagnosed MGs, standard of care usually involves surgical resection followed by radiotherapy and chemotherapy. Additionally, patients generally receive medical attention to control problems related to the associated seizures, peritumoral edema, fatigue and loss of cognitive function. Thromboembolism from leg and pelvic veins is common and must be managed to prevent further complications [4].

Surgery

The common recommendation from neurosurgeons is maximal, safe surgical resection; however, the benefit of maximal resection in improving survival is controversial [25]. Lack of objective and standard quantification methods for assessing tumor resection volume have obscured end results and inhibit comparisons across studies [21]. However, various retrospective studies suggest correlations between greater tumor resection, low residual tumor volume and improved survival [21, 26-28]. Nevertheless, surgical debulking mitigates symptoms associated with the growing tumor mass and mass effects [10]. MRI-guided surgical planning, as well as advances in functional MRI and intraoperative MRI, have increased the safety and extent of surgical resections specifically for tumors located in critical areas (e.g. eloquent cortex) [10]. Furthermore, awake craniotomy has demonstrated to be a useful surgical approach for preserving functional areas while maximizing safe MG resection [29].

Radiotherapy

Seminal clinical studies have established that patients receiving external beam radiation therapy following resection survived longer than patients treated with surgery alone [30, 31]. Early practice of whole brain irradiation was performed with the assumptions of multifocal MGs and tumor recurrence beyond the delineated tumor margins. However, later studies concluded that multifocal MGs accounted for approximately only 10% of cases and tumor recurrence occurred within 1-2 cm from the original tumor site in 80-90% of cases [32, 33]. Adjuvant focal radiotherapy following surgical debulking has demonstrated to increase patient survival ranging from 3-12 months [11, 34]. Patients are typically treated with a 60 Gy dose of radiation distributed once a day over a course of five days per week [4, 9]. However, for the elderly, radiation

use remains controversial. The dosage is spread over a three-week period for patients over 70 years of age as they are not able to tolerate radiation as well as younger patients and seem to only confer a three month survival benefit [4].

Chemotherapy

Early studies using cytotoxic drugs like nitrosoureas (e.g. 1,3-bis(2-choloroethyl)-1-nitrosourea; BCNU) failed to improve median survival. However, in the last two decades, more recent chemotherapeutic agents have played a larger role in treatment of MGs [30]. Meta-analyses have revealed that chemotherapy has an increase, albeit modest benefit in one-year patient survival rate (6% to 10 %) and two month increase in OS [35, 36]. Furthermore, a Phase III clinical study conducted by The National Cancer Institute of Canada (NCIC) and the European Organisation for Research Treatment of Cancer (EORTC) showed that median OS increased to 14.6 months for newly diagnosed GBM patients treated with radiotherapy and concomitant temozolomide (TMZ, Temodar^{TM}), followed by adjuvant TMZ therapy. Comparatively, OS in patients treated with radiotherapy alone was only 12.1 months. Additionally, the two-year survival rate was two-fold higher (26.5% versus 10.4%) in the group that received the concomitant and adjuvant TMZ [34]. TMZ is an oral alkylating agent with a small molecular weight (194 Da) and lipophilic properties; thus, it is thought to be able to cross the BBB [37]. TMZ has demonstrated anti-tumor qualities by depleting O^6-methylguanine-DNA methyltransferase (MGMT), a DNA-repair enzyme [34]. The MGMT promoter controls the activity of MGMT. Methylation of the promoter silences the MGMT gene, thus reducing DNA repair. Patients with MGMT promoter methylation seem to respond more favorably to TMZ with median OS of 21.7 months compared to 12.7 months for patients without MGMT promoter methylation [38, 39].

Another approach involves carmustine-impregnated biodegradable polymer implants, known as Gliadel Wafers, that are embedded in the tumor resection cavity. As the implant degrades, carmustine is released and diffuses into the tumor tissue with the goal of treating the remaining malignant cells. The addition of these implants demonstrated a 2.3-month median OS advantage sustained at two and three years [40, 41]. A limitation of this approach is that it relies on passive transport of carmustine, which results in the drug only diffusing a couple of millimeters (mm) into the surrounding tissue. However, malignant glioma cells may penetrate centimeters into the peritumoral margins, thus remain unaffected by such an approach [32].

Externally Applied Electric Fields

The most recently developed treatment modality for MGs, which has been called the "fourth standard treatment" by some, is externally applied tumor treating fields (TTF). TTF involves an array of electrodes on transducer pads adhered to the shaved scalp that apply, low-intensity, 200kHz alternating electric fields to the full brain. In vitro studies suggest that TFF kills tumor cells by disturbing various processes during cell division [15]. A randomized clinical trial, comparing TTF to common chemotherapy regimens for patients with recurrent GBM, concluded TTF produced similar mean OS and progression free survival (PFS) to chemotherapy [42]. In an open label Phase III clinical trial for patients with newly diagnosed GBM, TTF in combination with TMZ, was evaluated for efficacy after patients were initially treated with radiation and concomitant chemotherapy. The TTF/TMZ group demonstrated higher two-year OS of 46% compared to only 29% in the group receiving TMZ alone [43]. These results encouraged FDA approval of TTF for recurrent GBM in 2011 and for newly diagnosed GBM in 2015. No additional systemic toxicity is associated with TTF, although some

patients have reported adverse skin reactions. It should be noted that the cost of the treatment is high ($21,000 /month), which presents a serious barrier to its current accessibility [44]. One challenge unique to TTF therapy is patient compliance given that the electrodes must be worn at least 18 hours a day.

Recurrence

Regardless of treatment, MG recurrence is inevitable, with 90% recurring within a 1-2 cm vicinity of the original tumor site [33, 45]. For the most aggressive tumors (i.e. GBMs), median time to progression is just six to nine months following treatment [46]. At recurrence, surgical debulking may be recommended to reduce mass effect symptoms, however survival benefit is modest for recurrent MGs. Additional conventional treatments following recurrence is limited and at best, modest. In general, usefulness of conventional chemotherapy is slightly better in recurrent anaplastic gliomas than GBMs [47]. Results of a Phase II clinical trials evaluating the administration of TMZ in patients with histologically confirmed, recurrent AA or anaplastic mixed oligoastrocytomas, indicated objective response rates of 35% (evaluated by gadolinium-enhanced MRI), six-month rate of PFS of 46%, and median OS of 13.6 months [48]. Comparatively, a similar Phase II clinical study evaluating TMZ for relapse of GBM, reported objective response rates of only 5.4% and 21% six-month PFS [49]. Ultimately, most patients succumb to MGs, with median OS of about three years for AA and 14 months for GBM [9]. The few long-term survivors are typically young, otherwise healthy adults that can undergo aggressive therapy consisting of gross total surgical resections, radiotherapy and adjuvant chemotherapy. It should be noted that disabling dementia is a common side-effect caused by radiotherapy among these survivors [50].

METASTATIC BRAIN TUMORS

Epidemiology

Approximately 150,000 patients who die from cancer annually have CNS metastases detected at autopsy. Of these metastases, 15% involve the brain, and 10% are exclusive to the brain only [51]. The incidence of brain metastases is reported to be 9-17% based on various studies, although the exact incidence is thought to be higher [52]. This is because medical advances can detect primary neoplasms earlier leading to earlier treatment. Thus, these patients survive longer and increase the time they're vulnerable to development of brain metastases [53]. The most common primary tumors to metastasize to the brain are lung cancer, breast cancer, and melanoma, which combined account for 67-80% of brain metastases [52]. Approximately 10-15% of patients with small-cell lung cancer (SCLC) have brain metastases at diagnosis, and such metastases develop in 30-43% of patients with non-small-cell lung cancer (NSCLC) [54, 55]. In the case of HER2-positive breast cancer cases, up to one-third of patients experience metastasis to the brain [56]. Typical drugs to treat this type of cancer cannot cross the BBB, thus the brain is a safe location for metastases to thrive [57]. The relative low incidence of melanoma, testicular and renal carcinomas (compared to breast and lung cancer) is proportional to the low incidence of brain metastases originating from these primary sites. However, these cancers have the greatest propensity to metastasize to the brain [58]. Using the total number of patients with the five most common cancer primaries in the US estimated for 2018 (lung, breast, prostrate, colorectal and melanoma: total of 898,910 reported by NCI) and a conservative incidence rate of 6% [51], result in approximately 54,000 new cases of brain metastases for this year. This is triple the estimated number of primary gliomas (i.e.~18,000) [5].

Although many clinicians presume that all brain metastases are multifocal, it is suspected that 26-47% are unifocal [51]. These unifocal lesions are potentially amenable to focal therapies. In general, lung cancer and melanoma are more likely to be associated with multiple brain metastases, whereas breast, renal, and colorectal cancers have a slightly higher likelihood of developing as single brain metastases [53, 59].

Diagnosis

Similar to a primary brain tumor, the radiographic appearance of a brain metastasis is an enhancing mass, extending into the white matter and surrounded by edema as shown on MRI or CT. Unlike primary brain tumors, metastatic lesions rarely involve the corpus callosum or cross the midline. The radiographic appearance of brain metastases is nonspecific and may mimic other pathological processes, such as infection [58]. Brain metastases mimic the histology of the primary cancer and pathologists can pinpoint the underlying primary in patients presenting with metastatic disease [60].

Treatment

Surgery

Feasibility of surgical debulking is based on the number of manifested metastases and overall systemic status of the patient. Typically only patients younger than 60 years, who present a single lesion and otherwise have controlled primary disease, are considered for more aggressive treatment including surgery followed by radiotherapy [61]. This approach can achieve survival ranges of 3-13 months for SCLC and prostate carcinoma, respectively [53]. In the US from 1988 to 2000, there has been a 79% increase in annual number of surgical resections for brain metastases, possibly due to advances in surgical technology increasing safety of surgery [52]. Although surgery for multifocal disease is only considered to relieve symptoms due to mass effect, studies have indicated that

surgical removal of multiple metastatic lesions exhibit identical survival rates to those patients with a surgically resected single metastasis [62]. For 20% of long-term survivors, recurrence is expected, and a second surgery may be necessary [58]. Surgery is avoided when metastases have spread extensively to other organs and palliative radiation is the only option. Median OS for patients with brain metastases is only four to six months after treated with whole-brain radiotherapy, compared to one month if left untreated [60].

Radiosurgery

Radiosurgery is often considered an alternative to standard surgical resection. It is an aggressive local therapy using highly-targeted radiation in a single dose, and produces superior survival and quality of life in patients with only one to three brain metastases compared to surgery alone [51]. Unlike MGs, metastatic brain tumors are non-infiltrative and tend to have well-defined borders making them very suitable for focal therapies. Radiosurgery of brain metastases less than 1 cm in diameter result in a two-year local tumor control rates of 78% compared to only 24% for lesions greater than 1 cm. Median OS from the time of radiosurgery is 6-15 months, and some patients can live for years without recurrence [58].

Chemotherapy

Chemotherapy for the treatment of brain metastases has garnered less attention than radiotherapy, possibly attributable to limited BBB penetration. However, in some cases, systemic chemotherapy shows activity against brain metastases given the disruptions of BBB (due to compromise of tight junctions and/or accumulation of growth factors such as VEGF and pro-inflammatory cytokines) and leaky vasculature associated with brain tumors [63]. A Phase II clinical study of NSCLC patients with brain metastases treated with irinotecan and carboplatin showed an overall response rate of

65% and a median OS of six months indicating a positive result of systemic chemotherapy [64]. Furthermore, encouraging results have been demonstrated when systemic chemotherapy based on the primary tumor is administered to patients. For example, capecitabine (Xeloda) in conjunction with lapatinib, has shown some activity against brain metastases from HER2-positive breast cancer [58]. Furthermore, TMZ has shown positive results against brain metastases particularly in patients with NSCLC primaries [65].

Chapter 2: Convection Enhanced Delivery (CED)

THE BLOOD-BRAIN BARRIER

It is clear that treating MGs is still a difficult clinical challenge and success of standard treatment modalities is limited. Surgery and radiotherapy are incapable of eradicating the non-enhancing disease that has infiltrated the surrounding healthy tissue. Furthermore, only a few drugs delivered systemically have demonstrates various levels of success in treating MGs. Most chemotherapeutic agents are non-targeted and have been associated with systemic toxicity. Additionally, the BBB hinders drugs from reaching the CNS in sufficient quantities [66].

With over 100 billion capillaries and a total capillary length of 400 miles, the human brain is the best-perfused organ of the body. The total surface area of the brain capillary endothelium, which forms the BBB, is 20 m^2 [67]. The BBB is a protective, filtering mechanism present only in the vasculature of the brain, which prevents access of noxious substances to the brain. It consists of a continuous layer of endothelial cells (only ~ 200 nm thick) joined by tight junctions and surrounded by a basal membrane [63] (Figure 2.1). Embedded within the basal membrane are pericytes, which are supportive cells that regulate BBB permeability, maintain capillary blood flow and clear cellular debris [68]. Additionally, the feet-like projections of astrocytes also cover 95% of the basement membrane to maintain BBB integrity and may play a role in regulation of capillary blood flow [69].

Transport across the BBB involves movement across the luminal (blood) and abluminal (brain) membranes of the capillary endothelium. The tight junctions of the BBB prevents para-cellular transport of solutes from the blood into the brain interstitium. Therefore, solutes in the bloodstream can only gain access to the brain via transcellular transport. Small, lipid-soluble molecules unbound to plasma proteins may gain access to

the brain by lipid-mediated free diffusion. Otherwise, circulating molecules may gain access to brain only via endogenous transport systems within the brain capillary endothelium, which can be classified into three broad types: 1) carrier-mediated transport; 2) active efflux transport and 3) receptor-mediated transport, which is initiated from specific ligand interaction [67].

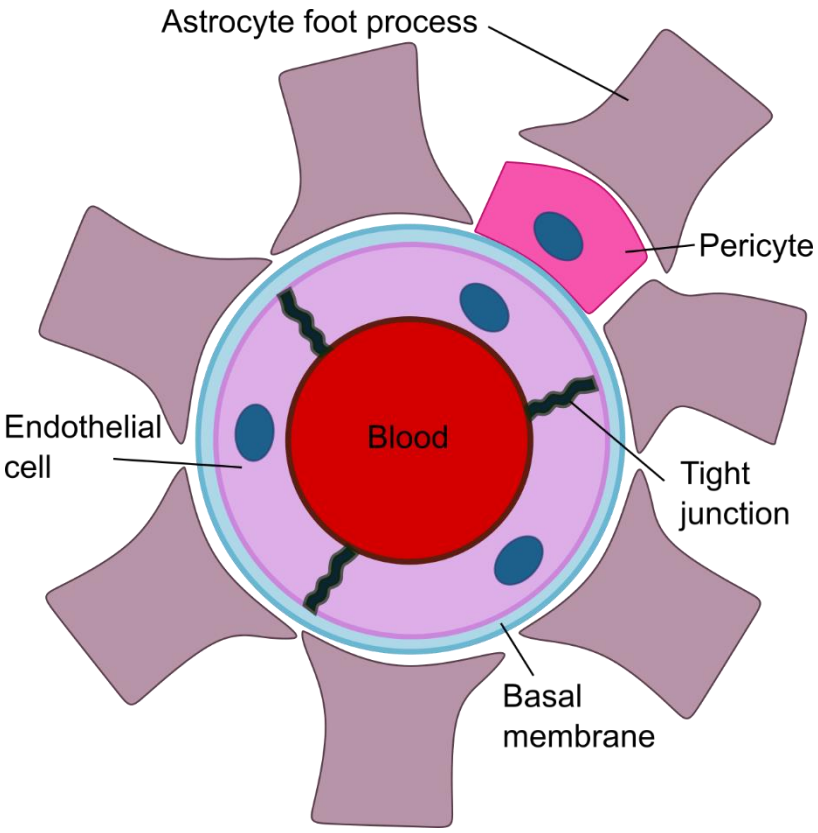

Figure 2.1: Schematic of cross-sectional view of a neurovascular unit comprising the BBB in brain capillaries. The basal membrane surrounds a continuous layer of endothelial cells secured by tight junctions. Pericytes and foot processes of astrocytes extend to the basal membrane. Illustration adapted from Regina *et al.* 2001 [71].

In order for drugs to be efficacious against MGs, they must enter the brain, which means facing the challenge of crossing the BBB. A common belief is that for drugs to cross the BBB in sufficient quantities, molecular mass of the compounds must fall below

400-500 Da. Additionally, they must have high lipid solubility (i.e. form less than 8-10 hydrogen bonds with solvent water) [67]. Even though TMZ fits the criteria as a small, lipophilic molecule, concentrations of TMZ in the brain reach only 30% of plasma concentrations [37]. Findings support that the BBB is actually impenetrable to approximately 98% of small molecules and 100% of macromolecules [67]. Hence, very few drugs are available for CNS treatments. One study reported that only 5% of the over 7600 drugs listed in the Comprehensive Medical Chemistry (CMC) database were active in the CNS. Average molecular weight for these drugs was 316 Da and their indication was for treatment of depression, schizophrenia and insomnia, not neoplasms [70]. Moreover, recent studies have shown that the drug efflux pump, P-gp, is highly expressed in the BBB. These multidrug transporters contribute to the impenetrability of the BBB and is linked to multidrug resistance in a variety of cancers, including primary brain tumors [71].

THE BLOOD BRAIN TUMOR BARRIER (BBTB)

Alterations in the BBB elicited by neoplasm growth result in the formation of the BBTB. The BBTB consists of capillary populations, including existing and newly formed capillaries, which deliver nutrients and oxygen to the rapidly growing tumor [72]. High grade MGs are associated with necrotic cores that induce expression of VEGF and angiogenesis resulting in abnormal capillary populations. Abnormalities in the capillary architecture can include capillary fenestrations (with pores ~ 12 nm in size) that increase permeability to small molecules resulting in a "leaky" BBTB as manifested in contrast-enhanced MRI [73]. Further development of the tumor triggers the formation of interendothelial gaps (as large as 1 μm) that non-selectively increase permeability to all water-soluble compounds [74]. Furthermore, Liebner *et al.* associated the downregulation

of the tight junction protein, claudin-1, with aberrant tight junction morphology and enhanced permeability in GBM microvessels [75]. Collectively, such disruptions to the BBB and BBTB amount to the enhanced permeability and retention (EPR) effect, which is characterized by accumulation and retention of nanoscale particles (e.g. liposomes, nanoparticles, and macromolecular drugs) in the solid tumor [76]. Therapies that can exploit the EPR effect, such as nano-drug delivery systems, may gain better penetration of the BBTB and preferred accumulation in tumor tissue compared to normal brain. However, the EPR effect in tumors of the brain is reportedly less pronounced and more restrictive to transvascular transport of large therapeutic molecules, compared to the EPR effect in solid tumors of other organs [77].

Nevertheless, a large population of capillaries in the BBTB resemble the continuous non-fenestrated capillaries of the intact BBB. Within a few millimeters of the tumor margin, the vasculature is more organized and less leaky compared to the core of the tumor. Therefore, the BBTB is still an obstacle for efficient delivery of drugs especially to the infiltrative GBM cells that may reside within brain tissue with a less disrupted BBTB [78].

ACCESSING THE CNS

Distribution of therapeutic agents within the central nervous system (CNS) is limited and challenging with existing drug-delivery techniques. Technologies such as catheters and pumps, bolus and intrathecal injections, drug-impregnated polymers, nanoparticles and biomaterials have all been investigated for accessing the CNS [40, 79-85]. Drawbacks of these techniques include poor bio-distribution due to limitations in diffusivity and molecular weight of the agent, neurotoxicity, and poor selectivity and/or

retention. A summary of advantages and disadvantages associated with selective technologies compared to the gold standard treatments for MGs are listed in Table 2.1.

The Ommaya reservoir is a plastic pump implanted under the scalp for intermittent injections of chemotherapeutic agents into the resection cavity or the CSF. This device has been used for many years to deliver methotrexate, doxorubicin, bleomycin, cisplatin and interferon-γ. Advantages of this technique include: multiple rounds of chemotherapy can be given through a single access site; it can be used for sampling CSF; and it can be implanted long-term. Given the limited bulk flow between the CSF and the intercellular space, chemotherapeutic agents via intrathecal delivery is not able to diffuse into the brain parenchyma to reach GBM. This technique is better suited for diseases localized in the leptomeningeal space (composed of pia matter and arachnoid matter) such as primary CNS lymphoma and various metastases [86]. Additional limitations associated with the Ommaya reservoir include increase in intracranial pressure resulting in high clinical incidence of hemorrhage, CSF leaks, neurotoxicity and infections [87].

The FDA-approved Gliadel Wafer is an adjunct therapy consisting of a polymer wafer impregnated with carmustine. Implanted into the resection cavity of gliomas, the Wafer circumvents the BBB delivering sustained local concentrations of carmustine, and is associated with increased survival in MG patients [40, 41]. However, distribution of the therapeutic is dependent on diffusion, resulting in distribution distances of only millimeters. Migration of the implant is associated with complications such as increased risk of seizures, cerebral edema and impaired wound healing [41, 88].

Method	Advantage	Disadvantage
Alternative Technologies		
Lipophilic drug	Rapid widespread penetration	Peripheral distribution/ exclusive to larger molecules/increased plasma-protein binding
Liposomes/immunoliposomes	Capable of receptor-mediated transport	Transport can be poor without vector mediation
Pro-drugs	Improved residence time	Poor selectivity and retention/ possible toxic metabolites
Carrier-mediated	Controlled delivery and retention	Drug structures must resemble endogenous nutrient
Vector/receptor- mediated	Works with many drug classes/ many linkers available	Saturable process/ often subject to enzyme dependent release
Osmotic BBB disruption drugs & contrast agents	Promising with range of vectors/ renders brain susceptible to circulating agents	Non-selective/ slow to reverse/ poor therapeutic/ toxic index
Biochemical opening of BBB	Can be selective for tumor vessels	Subject to infections/ lowers defense mechanisms
Bolus injection (intraventricular or intrathecal)	Bypass barrier/ rapid high CSF drug levels/ bypass enzymatic degradation	Poor tissue penetration/ surgical complications
Catheters and pumps	Prolonged/ controlled drug levels	Poor drug distribution
Drug-impregnated polymers & microspheres	Bypass BBB/ controlled prolonged delivery/ local delivery	Drug penetration very limited
Nanoparticles	Small enough to cross BBB, delivery of range of drugs	Unknown toxicological profiles
Focused ultrasound	Focal and transient BBB disruption.	Signal attenuation and distortion through skull/ inflammation
Electroporation	Significant and transient BBB disruption	Permanent tissue damage may occur depending of electrical parameters used
Gold Standard		
Surgery	Debulk to alleviate certain symptoms and allows for other treatments to proceed	Invasive/ limited to resectable tumors/ does not remove infiltrative malignant cells
Radiation	Can be used alone or in combination with other treatments/ no hospital stay is required/ brief sessions lasting only 15 min - 1hr	Side effects
Systemic chemotherapy	Minimally invasive	Challenged by BBB/ side Effects
Tumor-treating fields	Minimally invasive/ few adverse effects	Skin reactions/ costly/ requires continuous use (18 hrs/day)

Table 2.1: Methods of drug delivery to the CNS versus gold standard MG treatment. Portions of the table were adapted from Orive *et al.* 2010 [84].

Other methods employ disruption of the BBB, either permanently or reversibly, to increase permeability and access of therapeutics to the brain. These techniques involve electroporation, focused ultrasound, and osmotic disruption (e.g. infusion of mannitol to shrink endothelial cells). The advantages of these technologies include disruption to the BBB integrity, which increases permeability of water-soluble drugs, and chemo-sensitization. However, further development of these technologies is warranted to prevent structural damage and address inconsistencies in the results. For example, osmotic disruption is non-selective, which renders the brain vulnerable to substances in the blood leading to complications such as seizures, neurotoxicity and increased fluid in the brain [80, 89]. Focused ultrasound provides more targeted disruption of the BBB and can be used in combination of existing FDA-approved chemotherapeutic agents delivered intravenously [90, 91]. This combination therapy is currently in the preclinical stage. However, signal attenuation and distortion through the human skull and the inflammatory response associated with this technique require further investigation [92]. Finally, reversible electroporation can temporarily permeabilize the BBB and can be used to introduce drugs into the brain that would otherwise be impermeant [93]. This technique requires careful treatment planning to optimize the degree of electroporation and minimize permanent tissue damage. Factors to consider include electrical impedance and electric field distribution, tissue and electrode geometry, and pulsing parameters [94].

CED AS A MEANS FOR BYPASSING THE BBB

In an effort to address the challenges of current drug delivery methods, convection enhanced delivery was pioneered at the National Institute of Neurological Disorders and Stroke approximately 25 years ago. CED is an alternate approach to deliver large concentrations of macromolecules directly into the brain parenchyma and

effectively circumvent the BBB and BBTB [95, 96]. The technique relies on pressure driven bulk flow of fluid, pushed primarily through the interstitial space, via a small cannula. CED demonstrated high concentrations of macromolecules actively distributed centimeters into the tissue, an order of magnitude greater than with diffusion alone [95, 97].

In a seminal study, Bobo *et al.* investigated the distribution of two compounds administered to cat brains via a 26-gauge stainless steel cannula inserted into the white matter through a burr hole created in the skull and dura (Figure 2.2). Flow of ^{111}In-labeled transferrin (^{111}In-Tf; 80,000 Da) and [^{14}C]sucrose (359 Da) was controlled with a syringe pump. Administered flow rate was increased from 0.5 to 4.0 μL/min to maintain the pressure gradient measured in the infusion line. After two hours of continuous infusion, the distance of distribution (measured from source of infusion), defined with a concentration threshold of ≥ 1%, was 1.5 cm and 2.0 cm for ^{111}In-Tf and [^{14}C]sucrose, respectively. Given that the diffusion of ^{111}In-Tf during a two-hour time frame is negligible, the distribution was attributed to convective flow. The ratios of volume distribution (V_d) to volume infused (V_i) for ^{111}In-Tf was 6.0 and 13.0 for [^{14}C]sucrose. Although the majority of the infusion volume was maintained within white matter, extensive distribution of large molecules into grey matter, at relative homogeneous concentrations in the perfused region, can be achieved with CED [98].

Bobo *et al.* ascertained that stability was maintained throughout the infusion with no significant adverse effects. Moreover, additional studies concluded that CED does not lead to cerebral edema and is unaffected by capillary loss or metabolism of the macromolecule [99]. Furthermore, comparisons of CED against intravenous delivery of [^{14}C]sucrose showed that sucrose concentrations in the rat brain was 10, 000 times greater with CED than intravenously [100]. With these initial studies, CED was established as a

viable alternative method for providing regional distribution of large molecules, such as proteins and some conventional chemotherapeutic agents, to target areas within the brain [101-104]. Compared with other therapies, CED minimizes systemic and CNS toxicity due to local delivery, and infused doses need not be as high [105]. Furthermore, histological evidence demonstrate that tissue inflammation around the catheter is confined to a 50-µm radius [106]. For these reasons, CED has treatment applications in several cerebral disorders, including Parkinson's [107, 108], epilepsy [109], Alzheimer's [110, 111] and malignant gliomas [85, 86, 97, 99, 112-116].

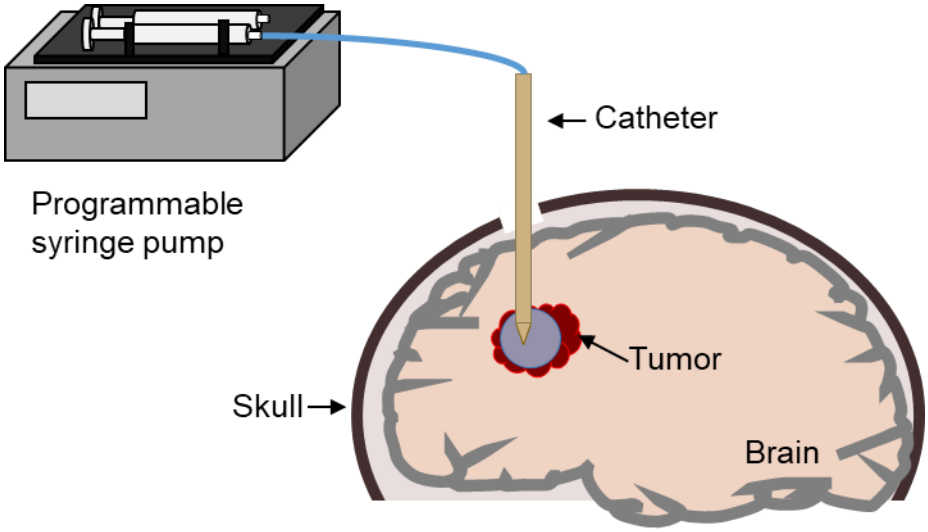

Figure 2.2: Schematic showing the premise of CED. The infusate is delivered locally to the brain parenchyma via a small catheter inserted through a burr hole. A programmable syringe pump is used to maintain the flow rate of the infusate.

CED for MG: Efficacy Studies

Distribution of macromolecules is more effective with CED than diffusion-based therapies and positive results in pre-clinical and early clinical trials for MGs showed promise of this technique [102, 103, 114, 117-119]. Early preclinical models performed by Bruce *et al.* investigated the therapeutic efficacy of BCNU and topotecan in a rat

glioma model. These experiments demonstrated adequate concentrations of the chemotherapeutics in the brain tumor and peripheral tissue. Furthermore, a 6-fold reduction in tumor cross-sectional area and longer survival was observed in rats receiving the infused agents, versus rats that had the agent via intraperitoneal administration [120, 121]. These favorable results led to a dose-escalating, Phase Ib clinical trial of 18 patients with recurrent MGs treated with CED of topotecan. The study concluded that topotecan had significant anti-tumor activity and showed progression-free and OS rates of 23 weeks and 60 weeks, respectively [122]. Additional conventional chemotherapeutic agents, such as paclitaxel and carboplatin have been infused directly into GBM tumors and/or surrounding tumor infiltrated brain successfully [114-116]. The initial success in preclinical/clinical trials with existing agents led to years of investigation of numerous anti-neoplastic agents using the CED technique including immunotoxins, radioisotopes [99, 103], gene therapies [123, 124], and nanoparticle conjugates [125]. Numerous clinical trials have been and are currently investigating CED for the treatment of neoplasms.

Targeted Therapy

Target toxins standout among the many new agents being developed with the goal of differentiating between normal and malignant cells to minimize collateral damage. The premise of these two-part macromolecules, also known as ligand-toxin, is that one part of the agent will “identify”, or target, the cancerous cell and the other part induces cellular death. Various clinical trials using targeted toxin and CED have been performed or are currently underway (Table 2.2).

To design ligand-toxins, the first component involves identifying cellular markers or internal proteins that are overexpressed in malignant cells, but not in normal cells. The

interleukin 13 receptor alpha 2 (IL-13RA2) was discovered to be overexpressed in 60-80% of patients with GBM and proved to be an attractive target in GBM [126-128]. The first generation of IL-13 based cytotoxins, increased patient survival by an average of 15 more weeks compared to the typical median survival for these patients [129]. Other targeting ligands include IL-4, epidermal growth factor (EGF) and transferrin (Tf) [100].

Trial Name	Targeting Agent	Toxin	Trial Phase
Cotara (NABTT-0404)	chTNT-1/B mAb	Iodine 131	I/II
IL13-PEI-106-R01	IL-13	PE	I
IL 4-PE (NBI-3001)	IL-4	PE	I
TranMID (KSB-311R/CIII/001)	Tf	DT	III*
PRECISE (IL13-PEI-301-R03)	IL-13	PE	III

Table 2.2: Clinical trial investigations of CED and targeted therapy.*Study was withdrawn.

The tumorcidal segment can be derived from multiple sources and take many forms. The most common bacterial-derived toxins are pseudomonas endotoxin (PE) and diphtheria toxin (DT), which are single chain proteins containing binding chains and catalytic domains [113]. The most common plant toxin is ricin [100]. The mechanism of cell death begins with the targeting-segment binding to the cell's surface. Upon entering the cytosol, the toxin inhibits catalysts involved in protein synthesis inducing cellular

death. Additionally, radioisotopes can also be combined with a targeting segment (e.g. monoclonal antibodies) for local, selective delivery of radiotherapy to brain tumors [117].

In the Cotara trial, ^{131}Iodine conjugated to a universal monoclonal antibody targeting necrotic cores of tumors, was infused in patients with recurrent or newly diagnosed GBM and AA [117]. Cotara was infused via cardiac/peritoneal catheters and SPECT scanning was performed two weeks after the infusion to determine the spatial distribution of the agent. Of the patients with recurrent GBM, 13.5% survived for 12 months and 5.4% survived for up to 24 months. One patient achieved long-term survival beyond five years [99].

The agent TranMID consisted of transferrin, which is expressed on all rapidly dividing cells, and a CRM107 molecule, which was modified from DT toxin to decrease non-specific binding. In the Phase II trials, patients with recurrent GBM and AA were treated with two infusions of TranMID. Radiographic complete and partial response were demonstrated in 15.2% and 21.2%, respectively. The median OS for these responders was 68 weeks, compared to only 27 for the patients that showed no response. Thirty percent of the patients were still alive 12 months after the first infusion [99]. Favorable results warranted Phase III of TranMID, however the study was withdrawn because of possible side-effects due to systemic toxicity associated with the DT toxin [113].

A Phase I trial investigating IL13-PE38QQR followed by radiation therapy with and without TMZ in patients with newly diagnosed MGs was completed in 2011. The goal of the study was to determine the highest dose of IL13-PE38QQR that can be safely administered via CED around the resected cavity. However, results are yet to be posted in the U.S. National Library of Medicine.

The PRECISE Trial

Progress towards clinical translation of CED has been challenged by inadequate results in a high profile, randomized Phase III efficacy trial, specifically known as the PRECISE trial. The trial was conducted worldwide in over 52 clinical centers. Patients with recurrent GBM were treated with a tumor-targeting agent made from combining the human protein IL-13 with a *pseudomonas*-based exotoxin, cintredekin besudotox (CB) (a.k.a IL13-PE38QQR), delivered intracranially using two to four commercially-available, single-port catheters. Median survival for the 183 patients treated with CED, compared to the survival of 93 patients treated with FDA-approved carmustine-impregnated implants (Gliadel Wafer), showed no significant OS improvement (36.4 weeks compared to 35.3 weeks, respectively) [85]. In the trial, the control arm exceeded its previous performance by 40%. Furthermore, it is noteworthy to point out that the company chose a survival endpoint of 50% longer survival than the historical controls. However, not a single drug in oncology has exhibited this kind of efficacy [85].

Retrospective Analyses of the PRECISE Trial

Retrospective investigations of the PRECISE trial have revealed that overly ambitious study endpoints, inaccurate catheter positioning and poor drug distribution are likely explanations behind the PRECISE trial's failure to meet clinical endpoints [130]. Although neurosurgeons were trained and guided in positioning catheters according to protocol, only 68% of catheters were protocol-compliant [85]. Mueller *et al.* reported even lower percentages of protocol-compliant catheter positioning in their retrospective study based on CT scans taken prior to the infusion of CB [131]. Their report highlighted the highly specialized nature of CED that requires strict technical guidelines to achieve consistent results. In ad hoc analyses of the PRECISE trial restricted to clinical centers that enrolled ≥ 6 patients, median OS of patients in the CB group is more favorable (46.8

weeks versus 41.6 for control arm) [130]. Nevertheless, inadequate catheter positioning alone cannot fully explain the response to CB in the PRECISE trial. Patients with good overall catheter placement scores had only a median OS of 38.1 weeks [131].

Further retrospectives studies were performed by Sampson *et al.*. They performed computational analyses of the drug distribution using catheter positioning data and the computational flow software, iPlan Flow (Brainlab AG, Feldkirchen, Germany). Results of the simulations revealed that the predicted coverages were well below the intended volume target. On average, only 20% of a 2-cm penumbra surrounding the resection cavity was targeted with the drug [130]. Therefore, Sampson *et al.* identified poor drug distribution as a possible explanation for the inadequate results of the PRECISE trial.

The inability of CED to perfuse drugs over large volumes, including margins beyond the primary enhancing tumor detected by MRI, is highly problematic as these margins contain infiltrative malignant cells that may be responsible for regrowth of the tumor. Thus, the suboptimal outcomes of the trial were linked to the poor coverage achieved during the infusions, suggesting that better delivery of the drug to the target tissue volume may improve CED. In the PRECISE trial, investigators were limited to using commercially-available catheters not designed for use in the brain parenchyma or brain tumors. These catheters were incapable of distributing drugs over large tissue volumes necessary for complete coverage of the tumor margins [130]. Thus, infiltrative GBM cells potentially residing in the primary tumor periphery (non-enhancing tumor) were left untreated [32].

Limitations of CED

Catheters

In light of the results of various clinical trials, it is warranted to examine whether the available technology used to perform CED is suited to overcome the unique challenges hindering drug distribution in the brain. The anatomical heterogeneity of the brain and tumor tissue and differences in permeability between white and gray matter can all inhibit drug distribution with CED. Specifically, the design of the catheters used to perform the infusions requires scrutiny [132-135].

The lack of CED-specific tools to perform the therapy in the PRECISE trial could have contributed to its suboptimal results. The catheters used in the study had a single port for infusion. These catheters were highly prone to reflux, or back-flow, along catheter walls and air-embolization [136]. Therefore, multiple catheters were required to attempt larger distributions in the brain. Multiple insertion tracts not only can increase the risk of trauma to healthy neurological tissue, but also increase the probability of cell-seeding healthy tissue with cancer cells along the multiple tracts [137, 138]. Similarly, various other CED studies were limited to "off-label" use of commercial catheters that may not possess the capability to effectively perfuse drugs over large tissue volumes (see Table 1). Therefore, there is a clear clinical need for improved catheters that address the drug delivery limitations of CED [113].

Reflux

A common drawback of CED is reflux of drug along the insertion tract, which results in ineffective drug distribution and premature termination of the CED therapy. Recognizing this need, catheter are now being developed to incorporate reflux-arresting properties, such as a "step-change", in which the diameter size of the catheter changes

along the distal tip of the catheter. Other designs and features added to cannulas to mitigate backflow include the "bullet-nose", or rounding of the cannula tip and the "recessed tip", an indentation on the distal end of the cannula [132, 133, 139-141].

Catheter	Company	Trial
Barium-impregnated one-port catheter	Medtronic® PS Medical (Goleta, CA, USA)	Phase I/II [142]
Barium-impregnated one-port catheter	Vygon US LLC (Valley Forge, PA, USA)	Phase III (PRECISE) [131]
Reflux-preventing neuro ventricular cannula	SmartFlow® MRI Interventions (Irvine, CA, USA)	Phase I [143]
Cleveland Multiport Catheter™	Infuseon Therapeutics, Inc. (Cleveland OH, USA)	Early Phase I [144]

Table 2.3: Examples of commercial catheters used in CED studies

Drug Distribution

Another major challenge of treating GBM is the highly infiltrative nature of the disease. Malignant cells extend centimeters beyond the resolvable tumor mass deep into the surrounding healthy tissue. Clinical recurrences of the primary tumor in the adjacent areas necessitate extended delivery to treat these infiltrative cells [9]. Recognizing this need, Infuseon Therapeutics, Inc. designed a catheter (Cleveland Multiport Catheter™) that offers multiple ports of infusion originating from a single insertion tract to extend the dispersal volume of the infusate for CED [144]. This approach may reduce the risk of trauma to healthy neurological tissue and probability of seeding malignant cells given it requires a single trajectory for insertion and removal. In addition, Vogelbaum *et al.* has demonstrated the Cleveland Multiport Catheter to successfully deliver high volume therapeutics during intra and perioperative infusions in recurrent GBM and AA [145]. Their catheter supports the concept of using multiple ports for achieving high volumes of

distribution, specifically in the non-enhancing tumor-infiltrated brain tissue. Others have opted for a different approach and are investigating intermittent, chronic delivery of therapeutics using catheters that are permanently implanted and accessed via a port on the side of the cranium [146].

Leakage

Leakage of the therapeutic into CSF spaces, such as the ventricles or sulci, are frequent (more than 20% of CED attempts) [147]. These structures act as low-pressure "sinks" and result in waste of the therapeutic and loss of pressure gradient driving fluids to the target tissue areas. One study found that leakage, not only prevented concentration of the infused agent to increase in the target tissue, but concentration started to drop in these areas once leakage occurred [148]. Furthermore, this opens the possibility of additional adverse effects from circulation of the therapeutic in the CSF affecting normal tissue. This study stressed the importance of monitoring the infusion to visualize the transport of the infusion agent. Imaging feedback opens the possibility of making adjustment during the infusion (e.g. changing catheter position) and may provide opportunities "to correct" the infusion.

Chapter 3: The Arborizing Catheter for Convection Enhanced Delivery

The "arborizing catheter" was developed to maximize drug dispersal in the brain [149, 150]. The arborizing catheter consists of multiple infusion ports or "microneedles" originating from within a rigid cannula, thus requiring one insertion path. Each microneedle individually arborize (branch-out) from the primary cannula to enhance drug delivery to desirable margins surrounding GBM. Risk of complications (e.g. mechanical damage) could be reduced due to the small diameter of microneedles. Additionally, because the microneedles are fully retracted back into the cannula prior to extraction of the catheter, the surface of the microneedles in contact with tumor tissue remain completely covered within the cannula, thereby reducing the probability of tumor cell-seeding in healthy brain tissue. Furthermore, the arborizing catheter design introduces a step change at the cannula-microneedle interface, a concept that has been demonstrated to mitigate reflux in the literature [86, 139, 151]. In this chapter, the components of the catheter are described in detail, including their design and fabrication process.

INTRODUCTION TO FIBEROPTIC MICRONEEDLES

Needles with dimensions in the order of micrometers offer clinical utility for minimally invasive delivery of fluid into tissue [152-155]. Microneedles made from flexible, light-guiding fused-silica capillary tubing, termed "fiberoptic microneedles" were used to simultaneously deliver laser energy and fluid agents in rat brains [156]. Introducing hyperthermia to CED demonstrated significantly, greater volume dispersal relative to infusion-only controls (approximately 60-80% greater) [157]. Given that microneedles are approximately 10-fold smaller than conventional catheters, they can potentially reduce mechanical trauma, bleeding, risk of stroke, and cerebral edema.

Additionally, smaller cannula diameters have been demonstrated to help mitigate backward flow or reflux [158, 159].

Nevertheless, the small lumen of microneedles are associated with high hydraulic resistance limiting the fluid delivery to small volumes [160]. However, this limitation can be mitigated by introducing the fluid through a system of microneedle arrays [161, 162]. Motivated by the limited volumetric dispersal of therapeutics in CED, an array of microneedles is proposed to deliver fluids to multiple regions of the brain and increase distribution of the infusate.

INVENTION OF THE ARBORIZING CATHETER

Proof-of-concept prototypes were originally fabricated from twisting six polyetheretherketone (PEEK) tubing (794 um OD, 381 um ID) around a seventh PEEK tube and bonded with a commercially-available cyanoacrylate epoxy to create a 10-cm long cannula for the arborizing catheter (Figure 3.1) [149]. This manufacturing process resulted in the outer diameter for the cannulas of less than 2.5 cm. The twisting of the PEEK tubing resulted in microneedles exciting out of the tubing at an angle. The microneedles were fabricated from 14-cm long pieces of fused-silica capillary tubing (TSP150375, Polymicro Technologies, Phoenix, AZ) epoxied to 22 G dispensing needle with a Luer lock. This initial prototype were evaluated in 0.6% (w/w) agarose brain tissue phantoms and one ex-vivo canine brain. Computer tomography imaging showed that the microneedles were successfully deployed in the brain and MRI demonstrated the distribution of the infused glowing gad-albumin along white-matter tracts with negligible reflux. The mean distribution ratio for the infusion was calculated to be 2.45. These initial infusion experiments were promising in establishing the feasibility of using the arborizing catheter (with microneedles) to deliver fluids into brain tissue.

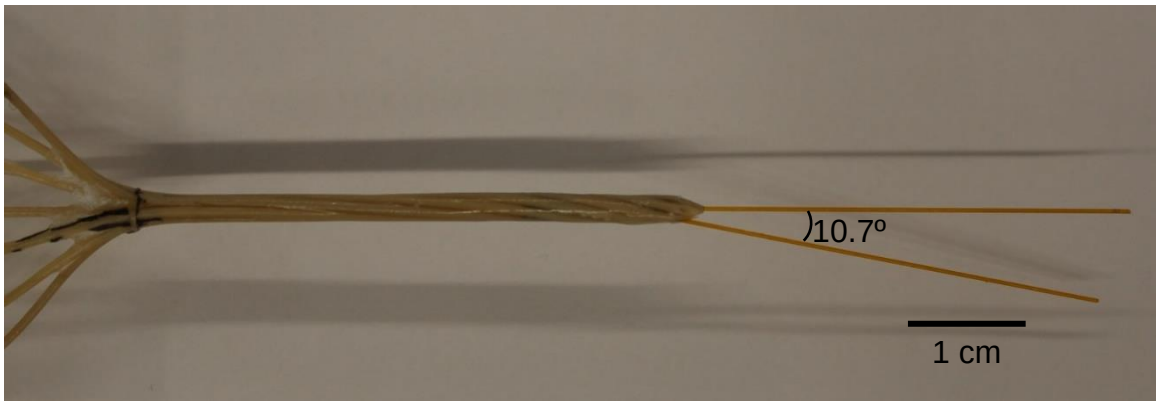

Figure 3.1: Proof-of-concept prototype. Microneedle deflection angle of 10.7º was measured from the axis of the cannula.

However, initial experiments also highlighted the drawbacks of the manufacturing method, material selection and functionality in the proof-of-concept catheters. These catheters were time consuming to manufacture, considering the non-biocompatible cyanoacrylate epoxy, which required 24 hours to fully cure. The twisting of the PEEK tubing throughout the length of the cannula provided resistance during microneedle deployment. Additionally, the deflection angle for the microneedles was only approximately 10º, which left room for improvement for these catheters.

FABRICATION OF ARBORIZING CATHETER BETA PROTOTYPES

Beta prototypes of the arborizing catheter consisted of a primary cannula with an outer diameter of 3 mm. The cannula was manufactured by bonding seven aligned biocompatible PEEK tubes (41568-L4, Analytical Sales & Services; OD 794 µm x ID 381 µm) with a light-cured medical grade adhesive (3972, Loctite®) (Figure 3.2A). A custom-designed fixture was used to twist and bend the PEEK tubes at the distal end of the cannula (Figure 3.2A-B). The twist at the end of the cannula caused the microneedles to branch out at an angle of up to 20° (angle of peripheral needles from cannula axis) when they were deployed (Figure 3.3A). Once the adhesive was cured, the distal end of

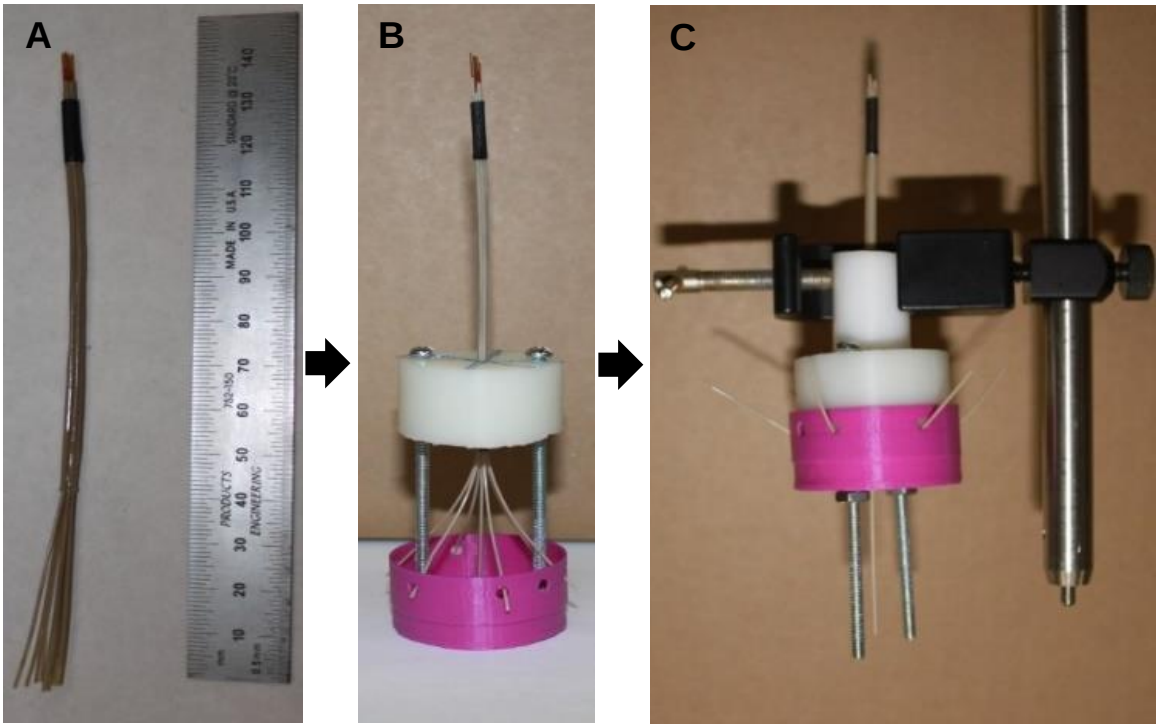

Figure 3.2: A) Six PEEK tubes aligned parallel to each other and concentrically around a seventh tube were bonded with adhered with light-cured adhesive. The last 40 mm of the tubing were left unglued B) The bonded portion of the cannula was attached to proximal end of fixture and the free tubing ends were threaded through equally spaced holes of cylindrical fixture. C) The free ends were twisted, bent and fixed in place with adhesive.

the cannula was polished to a smooth conical tip (Figure 3.3B). The cannula was made to house seven microneedles made from flexible, hollow silica optical fibers (TSP180375, General Separation Technologies) (OD 375 µm x ID 180 µm) polished to a smooth bevel tip (Figure 3.3C). The distal end of each microneedle was attached to a 22G hypodermic needle with a Luer lock adapter to allow for easy connection to small bore extension tubing. When deploying the microneedles, the small diameter of the microneedles compared to the primary cannula created a step change that helped to arrest reflux as demonstrated in other catheters with an incorporated step change [139, 141]. Unlike initial prototypes, these catheters reduced resistance of the microneedle sliding through

the PEEK tubing given that twisting was limited to the distal end of the cannula. Additionally, the medical grade UV-acrylic glue improved biocompatibility of the arborizing catheter. The performance of the beta arborizing catheter prototypes was compared to the performance of single-port catheters in infusion studies described in Chapter 4 [150].

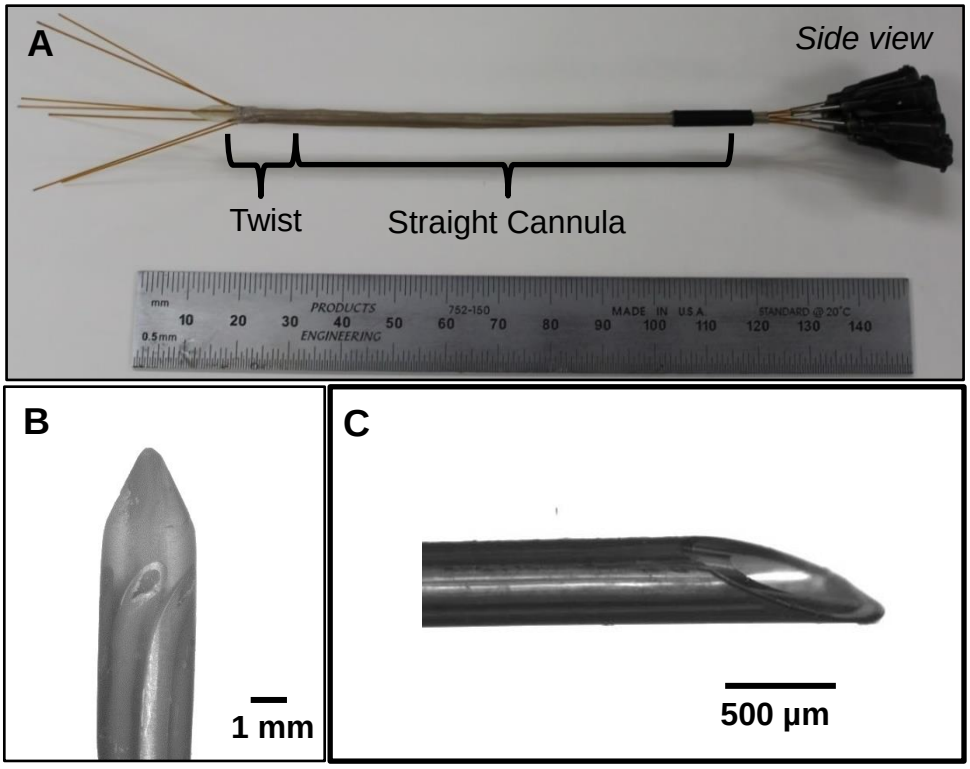

Figure 3.3: Images of the arborizing catheter prototype. A) Side view of the arborizing catheter with deployed microneedles at the distal end of the cannula (left) where the twisted PEEK tubing is labeled. At the proximal end of the cannula (right) the proximal end of the microneedles is shown with attached Luer lock adapters. B) Magnified image showing twisted PEAK tubing at distal end of the cannula, which allowed microneedle deflection. C) Magnified image of a polished, bevel-tipped microneedle. Image adapted from Elenes and Rylander 2017 [150].

DESIGN OF USER-INTERFACE DEVICE

When microneedles are fully retracted into the cannula, a portion of the flexible fused-silica capillary remains exposed. When they are connected to the fluid lines, the added weight can cause them to bend and break. Additionally, when deploying the microneedles, pushing the microneedles through the twist at the distal end of the cannula can cause buckling at the proximal, unsupported end. Therefore, a user-interface was created to hold the main cannula of the arborizing catheter and provide support to the microneedles and prevent them from buckling during deployment. The user-interface was first designed using 3D CAD software, Solidworks (Dassault Systèmes; Waltham, MA). The back-plate (37 x 57 mm) and the front-plate (40 x 55 mm) were first laser-cut from acrylic sheets shown in Figure 3.4 A-B. Mastercam for Solidworks (CNC Software Inc.; Tolland CT) was then used to convert the 3D CAD drawings to G-code for programing a 5-axis CNC mill (MDA Precision; Morgan Hill, CA). A triangular slot was milled into the back-plate for holding the microneedles. The back and front-plates are secured to each other with plastic screws to "sandwich" the cannula between the front and back plates (Figure 3.4 C). The front and back plates hold the cannula and provide the mechanical support required to prevent buckling or breakage of the microneedles.

EVALUATION OF ARBORIZING CATHETERS IN A CANINE MODEL

In vivo evaluation of the beta arborizing catheter prototypes and user-interface was conducted at the Virginia-Maryland Regional College of Veterinary Medicine (Blacksburg, VA) in order to understand user feasibility and functionality of the device. A Large Animal Core Report was provided by John Rossmeisl, DVM. The objective of the pilot study was to use the arborizing catheter to achieve rapid coverage of a tissue target, while tracking the microneedles, deployed using real-time MRI.

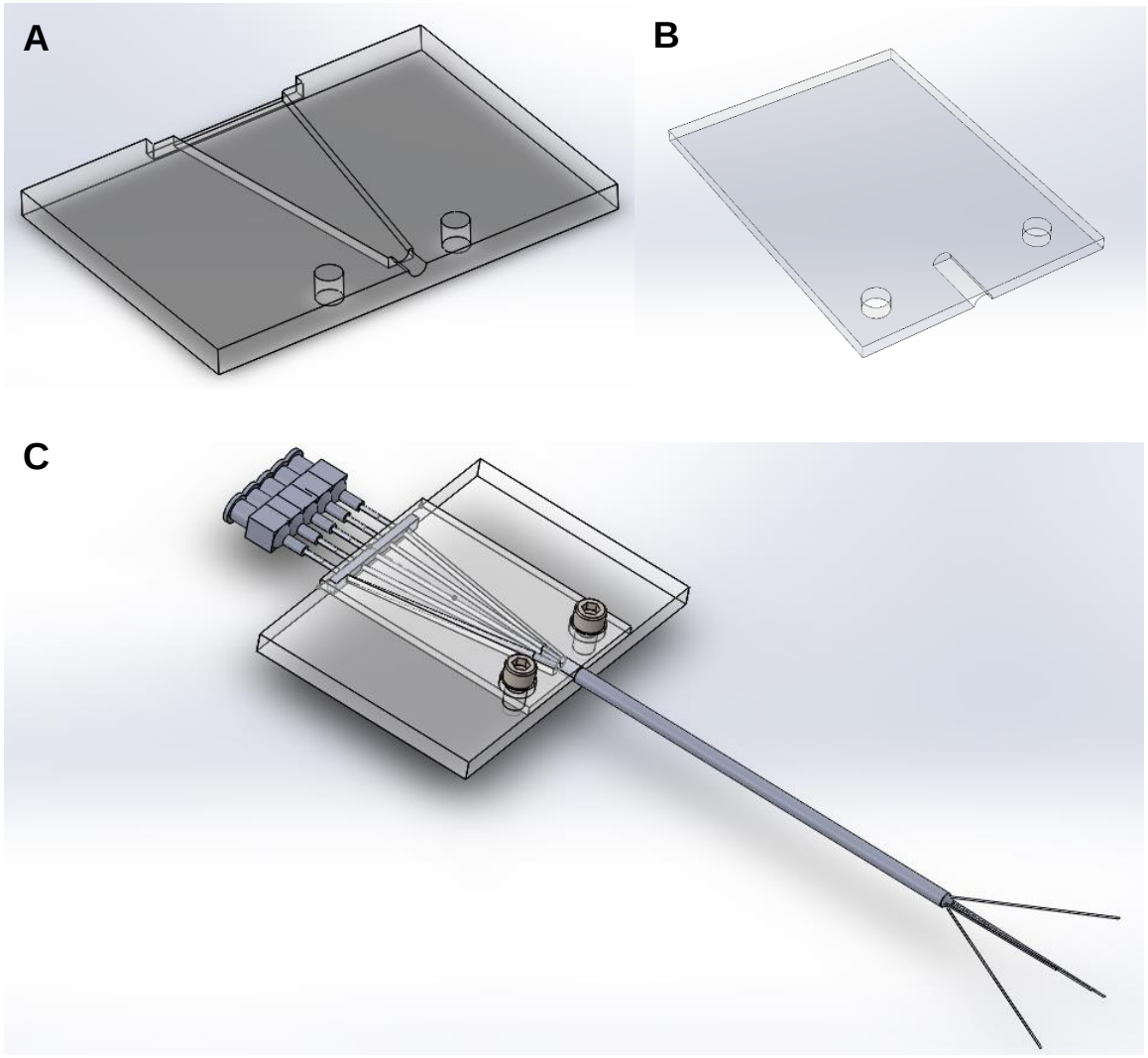

Figure 3.4: CAD illustrations of the user-interface. A) Back-plate B) Front-plate and C) User-interface and arborizing catheter assembly.

Two arborizing catheters were evaluated with bilateral hippocampal infusions (a common site for gliomas in canines) in a 23-kg female canine of mixed breed (Figure 3.5A). The arborizing catheters were deployed each 2.7 cm from the brain surface. The microneedlew were deployed 7 mm from the distal tip of the cannula. Three beveled-tipped microneedles were deployed from each catheter. The contrast agent, gadopentetate

dimeglumine (Magnevist ®), was infused at a rate of 1 μL/min/microneedle for total infusion time of 16 minutes.

Figure 3.5B-D, show MRI images of the canine pre-infusion and at V_i of 9 μL and 21 μL. The total volume infused for the first arborizing catheter (AC-1) was 42 μL, while only 28 μL were infused with the second arborizing catheter (AC-2) due to one microneedle breaking proximal to the Luer lock. Total volume dispersed and mean distribution ratio for AC-1 were 66 mm^3 and 1.57, respectively. Total volume dispersed and mean distribution ratio for AC-2 were 23 mm^3 and 0.82, respectively. The most notable adverse effect observed was intrinsic reflux up the cannula, which resulted in subarachnoid infusion (Figure 3.5E). Additionally, after deployment, the microneedles were not well resolved in the MRI scan. Finally, one microneedle fractured within the proximal aspect of the cannula during deployment (Figure 3.5- black arrow); therefore, only two microneedles were used for AC-2 resulting in poor target coverage. The break also introduced air into the brain and hindered full retraction of the microneedle into the cannula prior to withdrawal from the brain (Figure 3.5 F- red arrow).

The adverse effects encountered in the study highlighted that the beta prototypes needed to be improved to minimize reflux and prevent breakage. Although the user-interface was designed to support the microneedles, it is possible that the lack of familiarity with the new device could contributed to the adverse event. Nonetheless, the pilot study showed that rapid infusions for coverage of a constrained anatomical target using multiple ports were possible with the arborizing catheter.

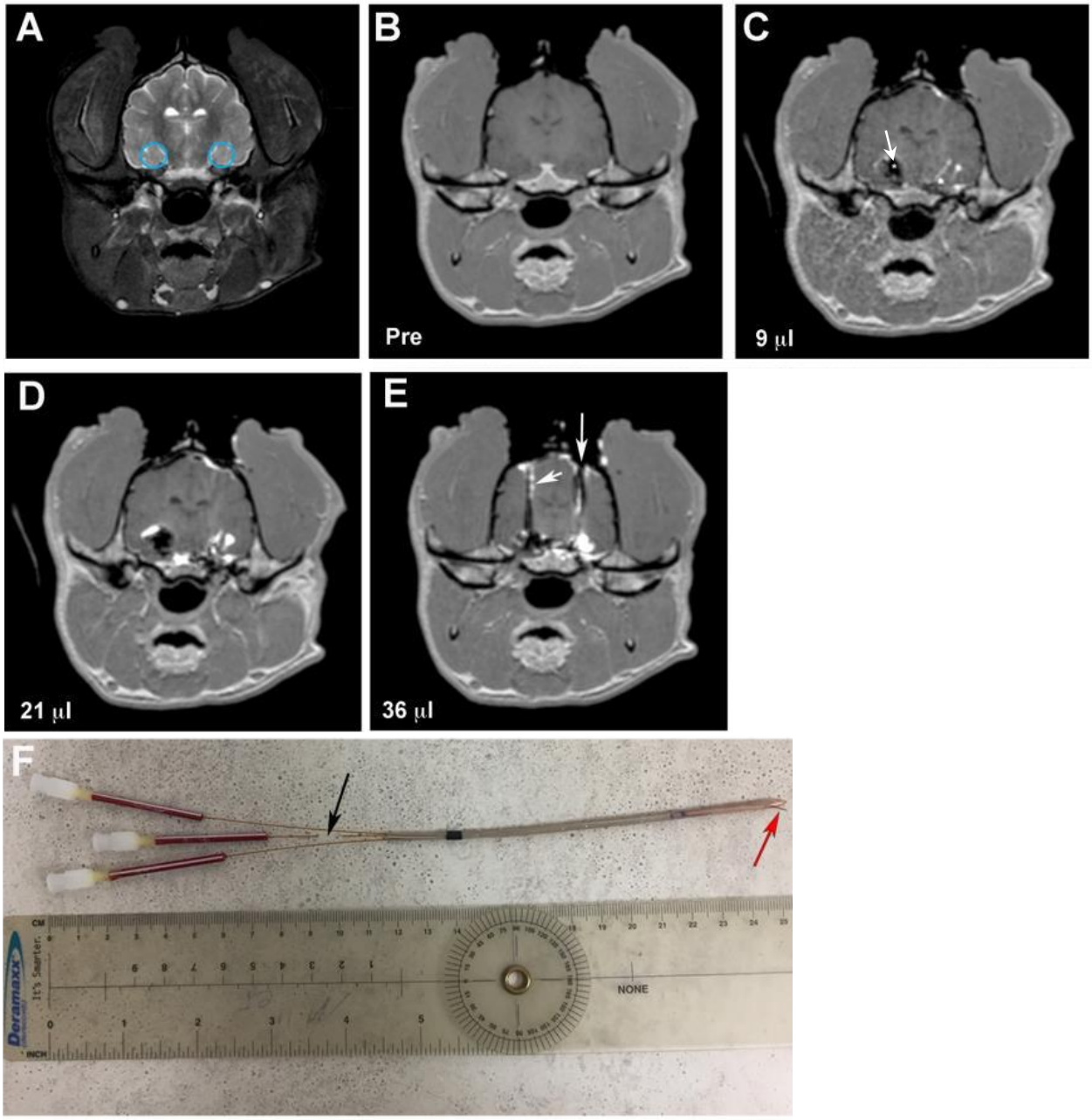

Figure 3.5: Canine CED pilot study. A) MRI scan showing volume targets in the hippocampus (blue circles) for CED infusions with the arborizing catheter. B) MRI scan of a canine patient prior to infusion of Magnevist imaging tracer. C) MRI scan showing V_i of 9 µL. Arrow points to air introduced due to microneedle breakage. D) MRI scan after V_i of 21 µL. E) Image showing reflux of image tracer up the cannula (arrows). F) Fractured microneedle (black arrow) complicated full retraction of the microneedle upon removal (red arrow). Photo credit: Dr. John Rossmeisl.

REFINING THE ARBORIZING CATHETER

The design of the arborizing catheter was re-evaluated and refined prototypes were fabricated following the design specifications established through the discussions within our group involving neurosurgeons (Table 3.1). The key feature of the catheter is the distal end of the primary cannula (3 mm OD) that consists of six biocompatible PEEK tubes (41568-L4, Analytical Sales & Services; OD 794 µm x ID 381 µm) bent at a radius of curvature of 28.3 mm. Deformation of the PEEK tubes was accomplished using a two-piece custom-manufactured fixture (Figure 3.6A). The PEEK tubes were fixed in their bent configuration with UV-cured medical grade adhesive (3972, Loctite®) (Figure 3.6B). Unlike earlier prototypes, only the distal portion of the PEEK tubes were fixed using an adhesive. The free, proximal end of the tubes are inserted in a PEEK 381G medical tube (Nordson Medical; 2.57 mm ID x 3.0 mm OD) to achieve a smooth, uniform cannula (Figure 3.7). Following the curing process, the distal end of the cannula was polished to obtain a smooth conical tip.

Design Criteria	Specification
Max cannula OD	3 mm
Length (for animal model)	13 cm
Max microneedle OD x ID	500 µm x 200 µm
Max microneedle deployment depth	5 cm
No. of ports	> = 5
Microneedle separation distance	>1-1.5cm
Materials	Ceramic, titanium, PEEK

Table 3.1: Design specifications for refining arborizing catheter.

The PEEK tubes guide six microneedles made from small-gauge (OD 375 µm x ID 180 µm) fused-silica capillary fibers (TSP180375, General Separation Technologies). Five microneedles were equally spaced surrounding the sixth microneedle at the center of

the cannula. The proximal end of each microneedle was attached to a 22G plastic dispensing needle with a Luer adapter for connecting to small-bore extension tubing. The flexible plastic dispensing needle was reinforced with PEEK tubing to add rigidity and prevent kinking/buckling during microneedle deployment. The distal ends of microneedles were cleaved flat. Based on infusion experiments comparing flat-polished versus bevel-polished microneedles, flat-tipped microneedles were more favorable at reducing the occurrence of reflux (see next section).

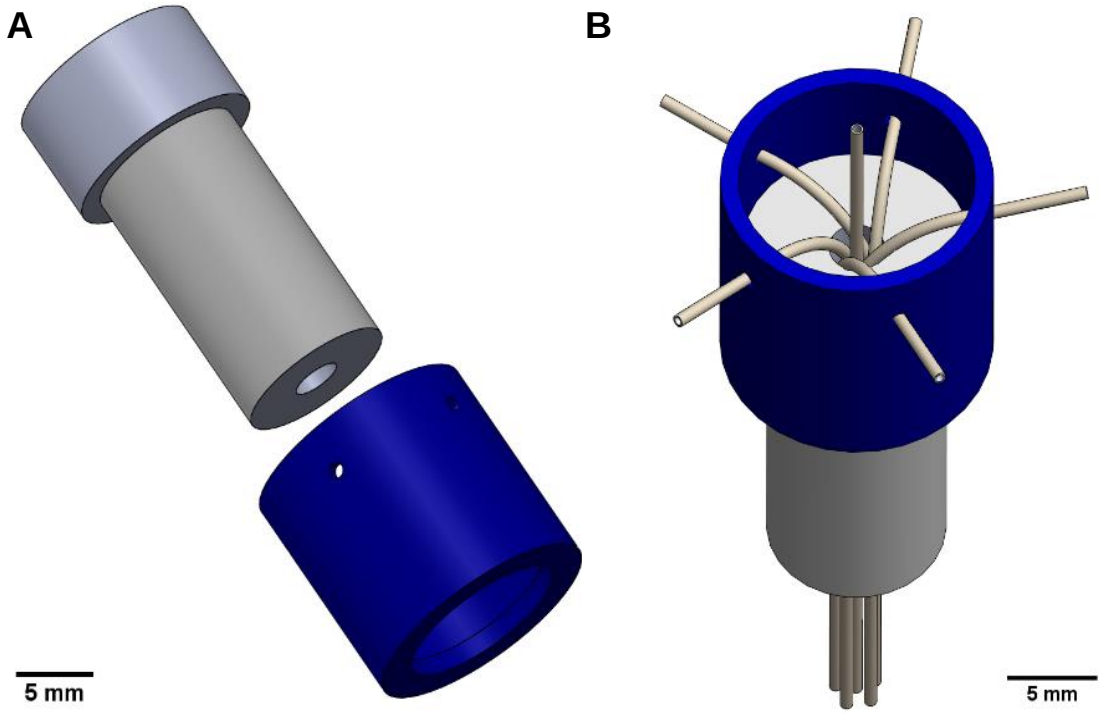

Figure 3.6: A) Drawing of the two components of the fixture for manufacturing the cannula of the arborizing catheter. B) View of assembled fixture holding and bending the PEEK tubing in place for bonding.

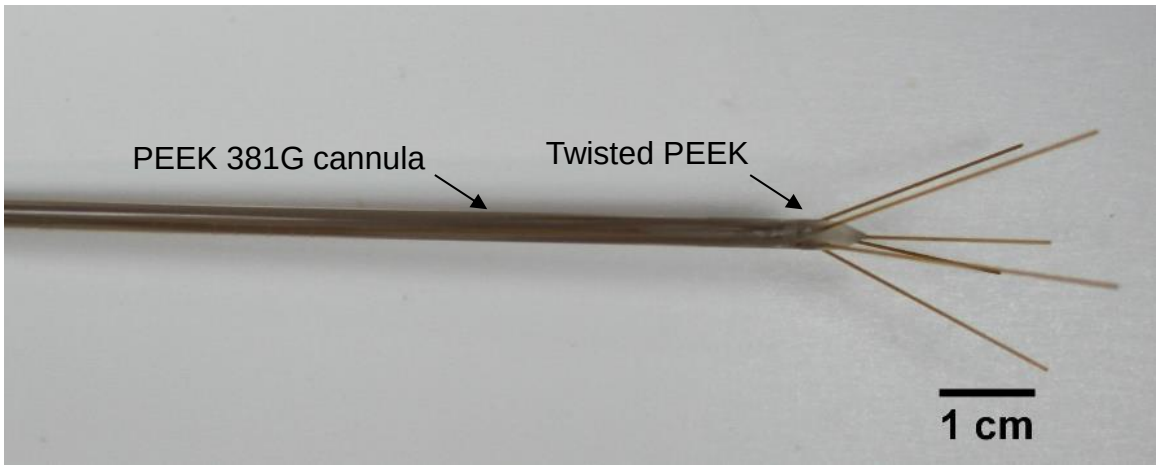

Figure 3.7: Arborizing catheter with six microneedles. The cannula consists of natural PEEK 381G medical tubing.

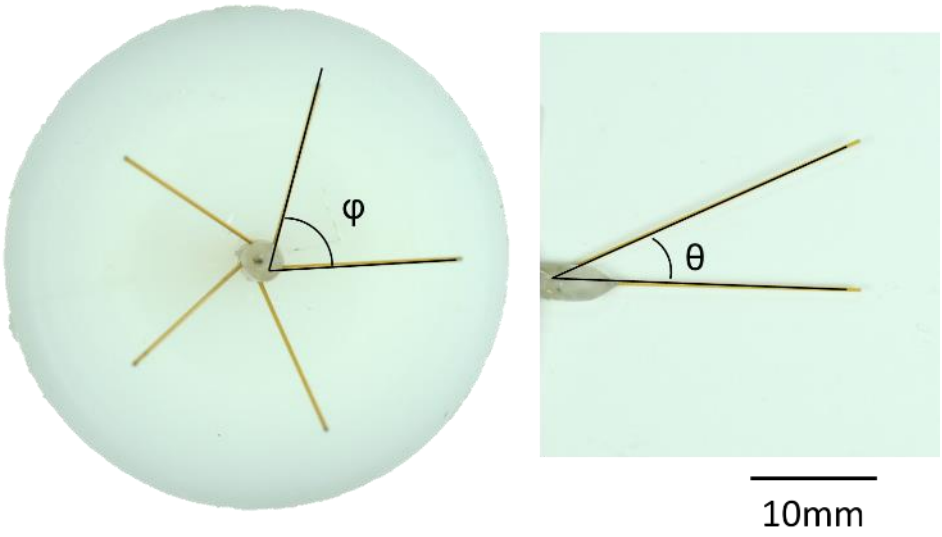

Figure 3.8. Measured angles of arborizing catheter. Phi (φ) was defined as the angle along the axes of two adjacent needles. Theta (θ) was defined as the angle of deflection of each microneedle in reference to the axis of the cannula

The fixture used to manufacture the arborizing catheter was designed to deflect the needles at 25º measured from the axis of the cannula. Images for each microneedle, deployed individually, were taken and imported into Image J to measure the angle of

deflection, θ (Figure 3.8). Transverse images of the distal tip of the cannula, with the microneedles fully deployed were also taken to measure the angle, φ, between two adjacent microneedles. The mean angle (n=10) and standard deviation were 26.6º ± 1.2º and 72.0º ± 3.2º for θ and φ, respectively. With the fixture, good reproducibility was achieved when fabricating the refined arborizing catheter prototypes.

Straight vs Bevel Polished Microneedles

The evaluation of beta prototypes in a pilot CED study in a canine model concluded that reflux needed to be addressed. Even with the inherent step-change at the interface of the 3-mm cannula and 375 μm OD of the microneedles, reflux was apparent. Therefore, the following infusions experiments were performed to compare bevel-polished microneedles versus flat-polished microneedles. The flat-polished microneedles are more similar to the reflux-preventing step catheter by MRI Interventions.

Microneedle Fabrication

The microneedles in these experiments consisted of a 22-gauge, 24 mm long hypodermic needle and a fused-silica capillary, polished at a bevel or flat (Figure 3.9: A). The capillary fiber was cut to 16 mm, and one end was coated with liquid cyanoacrylate adhesive (Loctite) and inserted into the penetrating end of the hypodermic needle. Care was taken to ensure that the end of the fiber was not sealed with glue.

Following full curing of the adhesive, the microneedles were polished using a fiber polishing lapping wheel (Ultrapol 1200) and custom-built fixtures to hold the microneedles. The microneedles were fixed perpendicular to the lapping paper for flat-polished needles (Figure 3.9B). A second fixture was used to hold the needles at ~20º in order to achieved a beveled geometry (Figure 3.9B). The microneedles were imaged with

a Nikon microscope to ensure their geometry. The average length of beveled microneedles was 40±1 mm and 39±1.5 mm for straight microneedles.

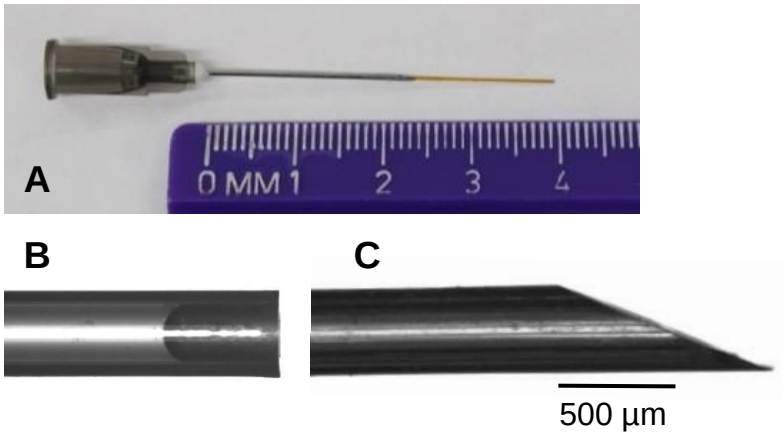

Figure 3.9: A) Microneedle consisting of 22-gauge hypodermic needle and fused-silica capillary tubing. B) Microscope image of flat-polished microneedle. C) Microscope image of beveled-tip microneedle.

Agarose/dye Preparation

For each infusion, 300 mL of agarose gel (0.6% w/w) was prepared by mixing agarose powder with deionized water on a stirring hotplate until it reached a low-boil and the solution became optically transparent. While the solution was still warm (> 50 ºC), it was decanted into a clear container and allowed to gelate. A syringe was filled with indigo carmine dye (2.5% w/w) and primed to ensure that no air bubbles had accumulated, then attached to a three-way stopcock. Infusion tubing and a differential pressure sensor (Omega Engineering) were also attached to the stopcock and similarly primed to remove any air bubbles. The microneedle was then attached to the other end of the fluid line (Figure 3.10A).

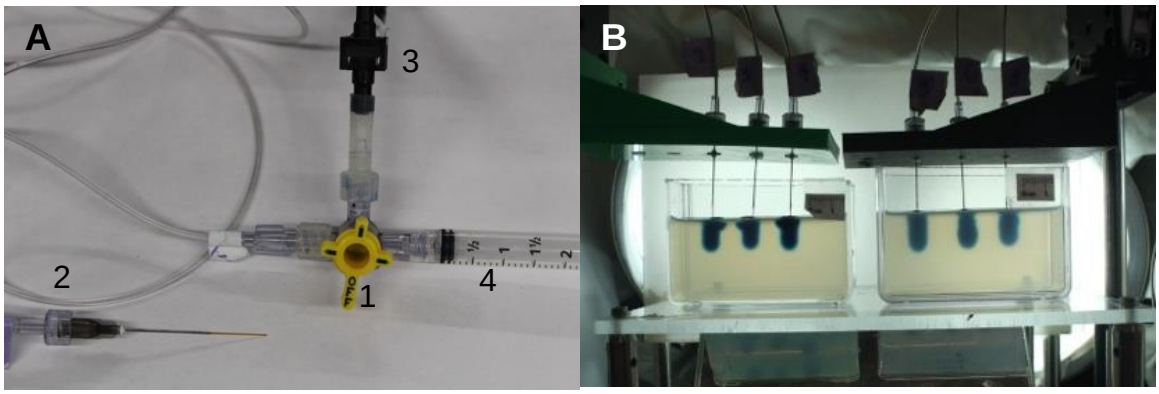

Figure 3.10: A) Infusion line consisting of (1) 3-way stopcock; (2) microneedle attached to catheter tubing; (3) pressure; (4) syringe. B) Shadowgraphy experimental setup.

Experimental Setup

Infusions were performed on a shadowgraphy experimental setup (Figure 3.10B). The microneedles were inserted into the gel using a leveled, linear stage micrometer. Infusion flow rate was controlled with a Harvard Apparatus syringe pump ramping up from 0.1μL/min to 3.0μL/min for 1 minute, then infusing at a constant rate of 3.0μL/min for 45 minutes. Throughout the infusion, the pressure sensors recorded pressure data and images of the infusion were captured at 1 frame/min to monitor the flow of the dye into the gel and any obstructions that occurred. This data was then uploaded into Matlab (Mathworks, Natick, MA) for analysis.

Results

The pressure readings for both straight and beveled microneedles were compared to determine trends in infusion pressure. Increased pressure readings were presumed to correlate to potential clogging (Figure 3.11). Results for the beveled needles (n=21) were very consistent (Figure 3.12A). A total of 20 out of 21 infusions refluxed (the outlier was an Expelled Clog and was not included in the data for that reason). Average pressure recordings did not increase higher than 0.34 psi. Average pressure reading for the straight

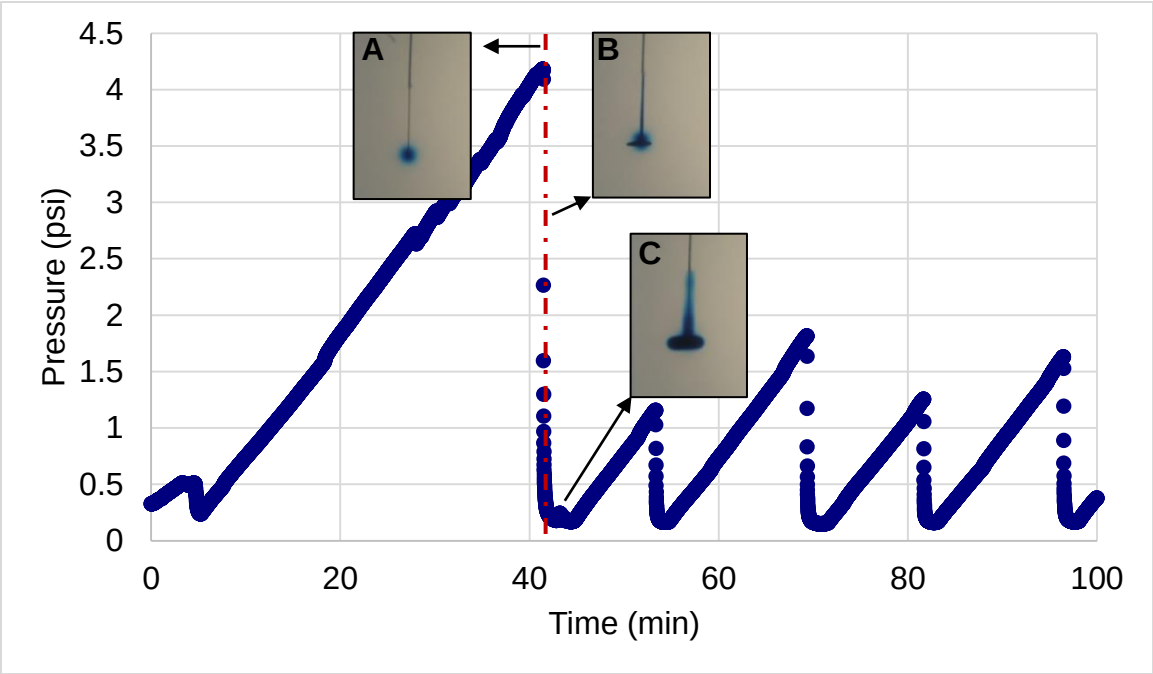

Figure 3.11: Line infusion pressure recorded for single infusion showing potential clogging. Peak pressure was measured at time = 41.4 minutes. A) Infusion image one minute before the peak pressure. B) One minute after the peak pressure indicated a rapid release of dye, suggestion potential clogging. C) Image taken several minutes after the potential clogging event showing dispersal of the dye.

needles (n=21) showed much more variability. Straight needles were further categorize into three group: ideal; refluxed; and expelled clogs (Figure 3.12B). These categories were defined based on the following criteria:

Ideal infusions (n=3) were characterized by maintaining a relatively constant pressure profile with mean pressure value of 0.37 psi. An increase in pressure was observed during the first 10 minutes of the infusion with a maximum average pressure reading of 0.68 psi. In the agarose gel, they formed a teardrop shape indicating forward flow and relatively homogeneous distribution of the dye at the microneedle tip (Figure 3.13A).

Refluxed infusions (n=5) were also characterized by maintaining a relatively constant pressure profile throughout the infusion. The average pressure reading was slightly lower than ideal infusions at 0.34 psi. Max average pressures for all the infusions in this category was 0.46 psi. However, these infusions were most noticeable in the agarose gel, where they would form a cylindrical shape (Figure 3.13B). The dye distribution was greater near the surface of the gel than for ideal infusions. Furthermore, in some cases pooling of dye on the surface of the gel was observed.

Expelled clog infusions (n=13) were characterized by a buildup of pressure (above 1 psi) indicating the presence of a potential clog, and a later drop in this pressure, indicating the possible expulsion of the clog. These infusions were identifiable in the agarose gel by the sudden expulsion of a large volume of dye (Figure 3.11B). Due to variability after the expulsion of the initial clog, these infusions were further categorized into three subcategories. Pressure data for the subcategories are plotted in Figure 3.12C.

a. Expelled Clog, then further Clogging: After the expulsion of the clog, pressure readings continued to rise, potentially indicating further obstruction of the microneedle or only partial expulsion of the clog.

b. Expelled Clog, then Forward Motion: After the expulsion of the clog, pressure readings did not continue to rise. However, the average pressure value did not fall down to magnitudes associated with ideal or reflux infusions. Rather average pressure reading for this subcategory remained within 0.88-1.64 psi.

c. Expelled Clog, then Reflux: After the expulsion of the clog, pressure readings dropped noticeably and plateaued at ~0.38 psi. Images demonstrated the dye flowing back to the surface around the needle shaft (in the direction of least resistance).

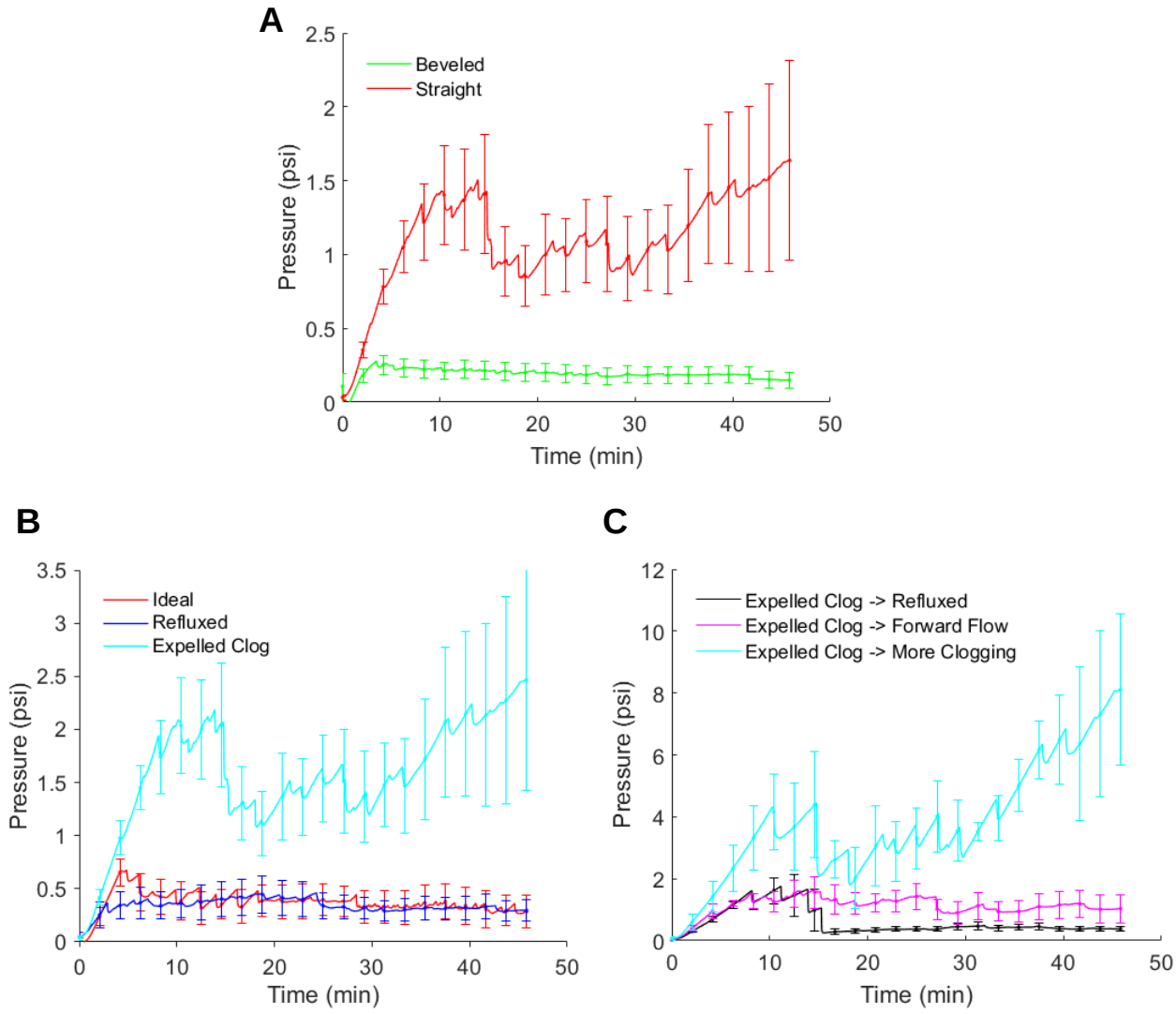

Figure 3.12: A) Mean pressures and standard error for all the beveled-tip microneedles and the straight-tip microneedle infusions. B) Mean pressure and standard error for straight-tip microneedle infusions categorized as ideal, refluxed and expelled clogs. C) Mean pressure and standard error for straight-tip microneedle infusions that demonstrated clogging (pressure spike), which were further subcategorized into events encountered after the clog was expelled.

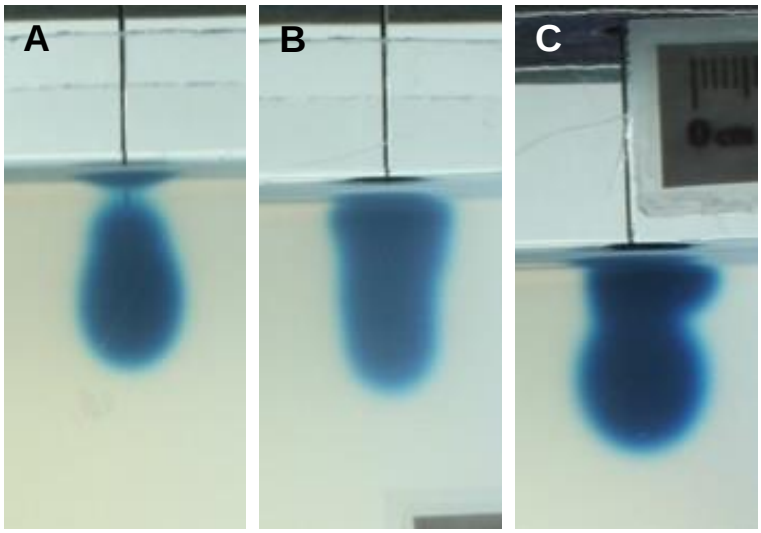

Figure 3.13: Infusions of indigo carmine in agarose gel. A) Ideal infusions were characterized by mostly forward flow. B) Refluxed infusions were characterized by larger infusion volumes towards the proximal end of the needle and surface of agarose gel. C) Infusion shape for expelled clogs were variable and were characterized by pressure build-up in the infusion line.

Conclusion

The beveled-tip microneedles inherently refluxed consistently during 20/21 infusions. These infusions were characterized by average pressure reading below 0.34 psi and backflow of the dye around the microneedle shaft as shown in images. Avoiding beveled-tip microneedles would help mitigate the adverse effects that were observed in the canine pilot study. However, infusion results for the straight-tip microneedles showed more variability. These microneedles had a higher propensity for pressure spikes that may be linked to obstruction of the microneedle when inserting into the agarose gel.

Chapter 4: The Arborizing Catheter for Convection Enhanced Delivery in Tissue Phantoms [1]

INTRODUCTION

CED is an investigational therapy, pioneered approximately 25 years ago, as a means of bypassing the BBB and BBTB to deliver therapeutic agents locally to MGs. By resolving the shortcoming of poor drug distribution highlighted in the PRECISE trial, the success of CED can potentially improve; hence, the arborizing catheter was developed to enhance dispersal of the infusate. In this chapter, the beta prototypes of the arborizing catheter were compared to a single-port catheter using agarose gels as a tissue phantom. Infusion with the two types of catheters were performed and analyzed to determine whether the arborizing catheter with its multiple, separated infusion ports could achieve greater volumetric dispersal (V_d) of the infusate and greater mean distribution ratio (V_d:V_i), compared to a single port catheter.

METHODS

Arborizing Catheter Design and Fabrication

Methods for the design and manufacturing of arborizing catheter are described in full detail in the preceding chapter. Briefly, the arborizing catheter prototype used in these experiments consisted of a primary cannula housing a total of seventh microneedles. Six microneedles were deflected, or arborized, from the seventh, un-deflected microneedle. Each microneedle was able to be individually deployed or retracted to the surrounding tissue.

---

[1] Portions of this chapter were published in: Elenes, E.Y. and C.G. Rylander, Maximizing Local Access to Therapeutic Deliveries in Glioblastoma. Part II: Arborizing Catheter for Convection-Enhanced Delivery in Tissue Phantoms, in S. De Vleeschouwer, Editor. *Glioblastoma*: Brisbane (AU); 2017. E. Y. Elenes conducted the research study and prepared the manuscript under the supervision of C. G. Rylander.

Fabrication of Single-port Microneedle Catheter

Single-port catheters were manufactured in-house. They consisted of a single microneedle (OD 375 μm x ID 180 μm), 3 cm in length, attached to a 22 G hypodermic needle (1.9 cm length) with a Luer lock. The distal end of the single-port catheter was polished to a smooth bevel tip.

Agarose Tissue Phantom Preparation

Agarose tissue phantoms were prepared for infusion studies. An agarose solution was mixed at 0.6% (w/w) by reconstituting agarose powder in deionized water. The solution was heated to a low boil and continuously stirred until all the agarose powder was completely mixed. The agarose was allowed to cool at room temperature and then poured into transparent molds. For all experiments the agarose solution was decanted into the mold and the device of interest (single or arborizing catheter) was inserted in the solution while still liquid (approximately at 50 ^{o}C). The microneedles were deployed approximately 2.5 cm from the exit point of the cannula, which resulted in each microneedle being separated from an adjacent microneedle by distances ranging approximately 0.4-0.6 cm. This casting method allowed a tight seal around the device and helped mitigate reflux. The agarose was allowed to set at room temperature and infusion began when the temperature of the agarose reached 23 $\pm$ 2 ^{o}C. For infusions using a single microneedle, polystyrene molds (1.7 cm x 8.1 cm x 3.9 cm) with an open top were used. For infusions using an arborizing catheter, a 10 cm cubic glass mold was used.

Infusions

The goal of this study was to compare the volume dispersed and mean distribution ratio for a given infusion using a single-port catheter versus the arborizing catheter, which is a multiport catheter consisting of seven microneedles. Using a programmable

pump (PHD ULTRA™ Syringe Pump, Harvard Apparatus) to control volumetric flow rate, 5% (w/w) indigo carmine dye was infused in the agarose gel. As a baseline, the V_d and V_d:V_i for a single-port catheter was determined at a flow rate of 1 µL/min for 100 minutes. A similar infusion was performed using the arborizing catheter. The flow rate for each microneedle was maintained at 1 µL/min/needle. Finally, because the arborizing catheter consists of seven microneedles, each a delivery port, a third set of infusions was performed using a single-port catheter with seven-times higher flow rate in order to compare V_d and V_d:V_i when equal volumes of infusate were delivered to the tissue phantom (i.e. equivalent to the Vi for the arborizing catheter). To summarize, the three experimental groups were: 1) single-port infusions (n=5) at a flow rate of 1 µL/min for a total Vi of 100 µL; 2) single-port infusions (n=5) at a flow rate of 7 µL /min for a total V_i of 700 µL 3) infusion with the arborizing catheter (n=5) performed at 1 µL /min/needle for a total V_i of 700 µL.

Shadowgraphy Technique

To evaluate the prototypes, a shadowgraphy experimental setup was used consisting of a clear stage with reflecting mirror on the left side and bottom (Figure 4.1). For each infusion, the sample was placed on the stage and backlit with various lamps placed behind a light-diffusing sheet. A DSLR camera (Rebel T1i, Cannon) mounted in front of the stage, simultaneously captured images containing three views of the sample (front, side and bottom), within the same frame, which were used to estimate the volume dispersed of the infused dye (Figure 4.2). Images were captured at a rate of one frame per minute for a total of 100 minutes. Metric scale bars were included in each image.

The images were then processed using an algorithm coded in Matlab (Mathworks, Natick, MA). Original images were cropped into three separate view frames: front, side

and bottom. Each cropped frame was then subtracted from the first image in the series to remove the background and thus only show the infusion volume. The differential images were then converted to grayscale and then to binary images by computing the global threshold based on Otsu's method [163]. Otsu's method assumes that the grayscale image is composed of background and foreground pixels. The algorithm iterates through all the possible threshold values that minimizes the intra-class variance, σ_w^2, defined as the weighted sum of the background and foreground variance, σ_b^2 and σ_f^2, respectively:

$$\sigma_w^2 = W_b\sigma_b^2 + W_f\sigma_f^2$$

Pixels with intensity values below the global threshold value were assigned black and pixels with intensity values greater than the threshold value were assigned white.

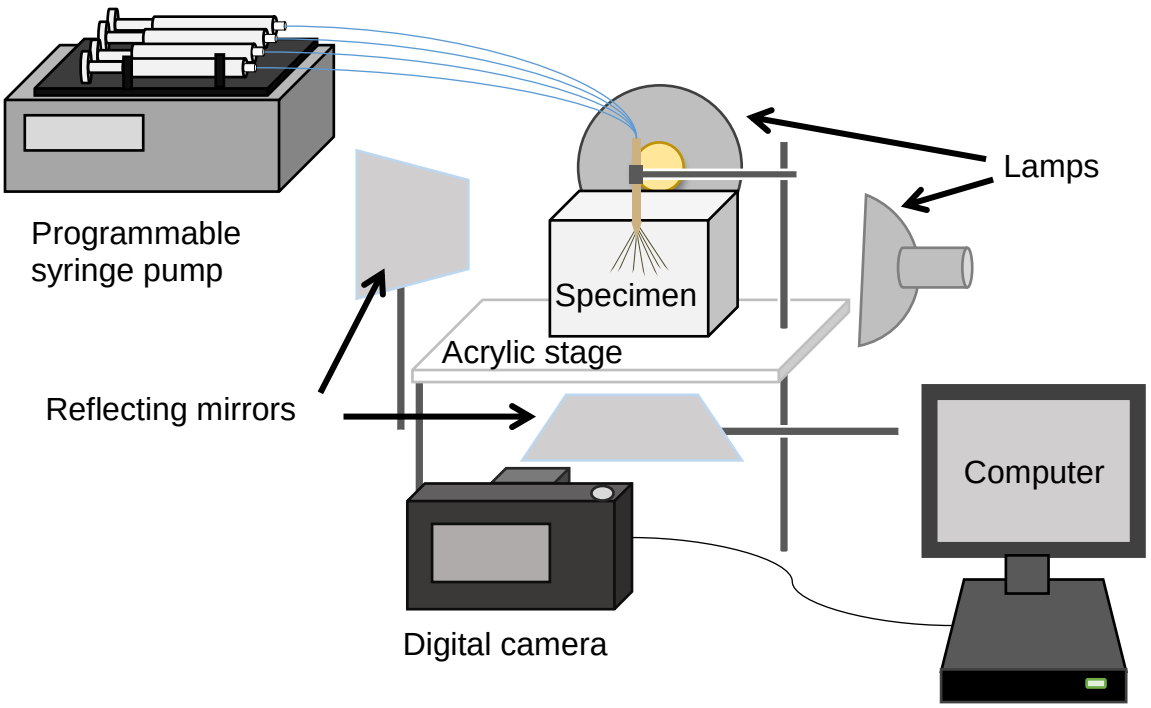

Figure 4.1: Shadowgraphy experimental setup. A programmable syringe pump was used to control the infusion of dye into agarose tissue phantoms placed on a clear acrylic stage backlit by lamps. A DSLR camera controlled by a desktop computer captured images of all three views (front, bottom and side) at a rate of one frame per minute.

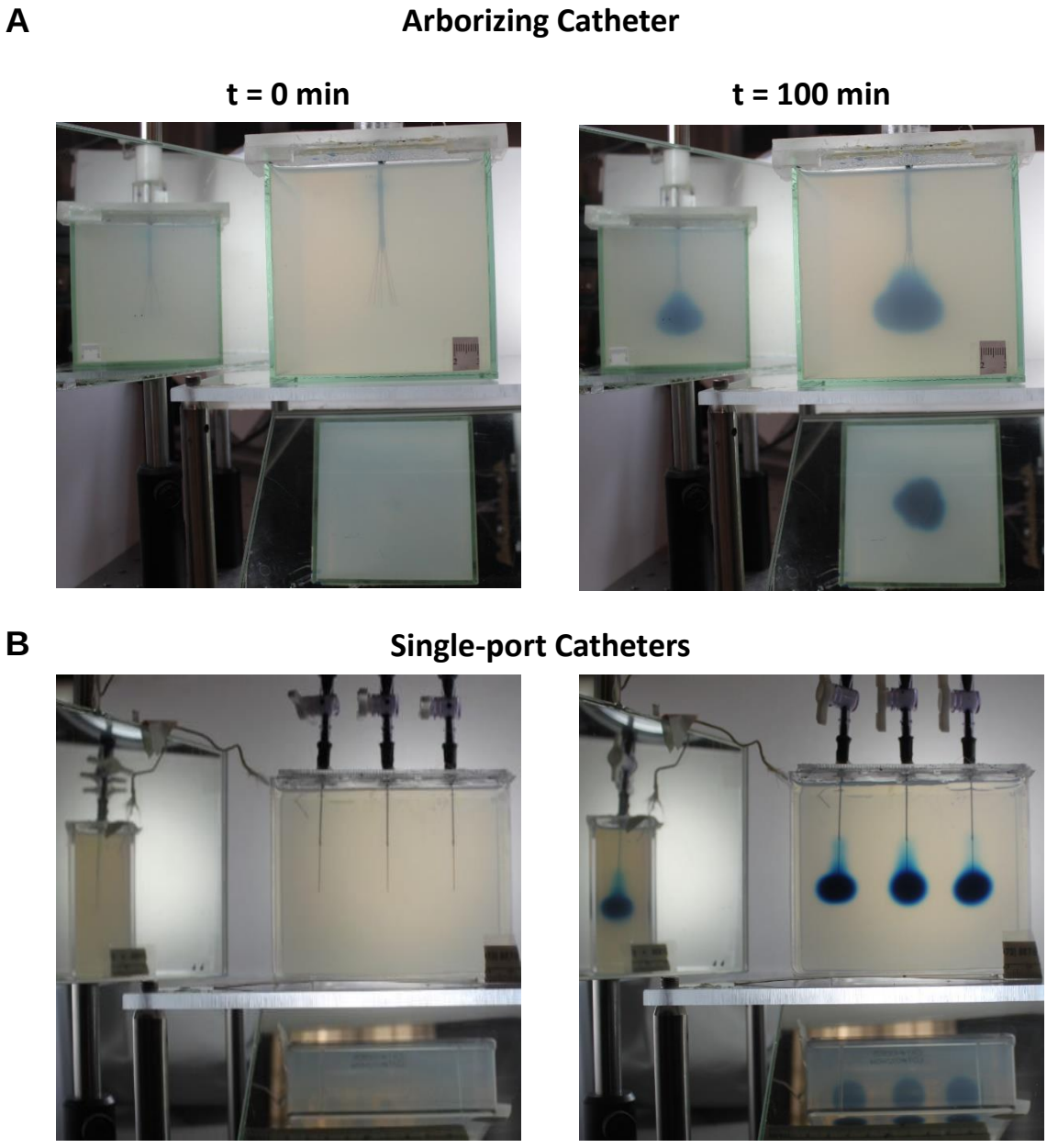

Figure 4.2: A) Images captured using the shadowgraphy experimental setup of the arborizing catheter prototype in agarose tissue phantom prior to infusions (t=0 min) and after 100 minutes of continuous infusion of indigo carmine dye. The front, side and bottom views were captured within a single frame. B) Image of single-port catheters (n=3) in agarose gel captured with experimental setup at t=0 min and t=100 minutes of continuous infusion.

The V_d for each cropped view frame was quantified using an image processing method previously described [164]. Briefly, the method assumes that V_d is axisymmetric, about the axis of single-port catheter or primary cannula of the arborizing catheter. The volume is discretized into elementary frustums of right circular cones (Figure 4.3). The algorithm counts the number of black pixels in each discretized section to calculate the bottom and top diameters of each frustum. A scale factor, extracted from the original image, was used to scale the pixel sizes of each binary image. The final volume was calculated by summing the volume of all the individual frustums:

$$V_d = \sum_{i=1}^{n} \frac{\pi h}{12} (A_i^2 + B_i * A_i + B_i^2)$$

where, h is the pixel height, A is the small diameter of the frustum and B is the larger diameter of the frustum.

The final V_d for an infusion was reported as the average of the three views: (front, side and bottom) of each image. The mean distribution ratio (V_d:V_i) was calculated by dividing the V_d by the total infused volume (V_i) that was programmed in the syringe pump. For infusions using the single-port catheter, the volume was observed to be relatively spherical. Therefore, only the front view of the images was used to calculate V_d.

Using the statistical software R (R Foundation for Statistical Computing, Vienna, Austria), one-way ANOVA tests were performed to analyze differences in V_d and V_d:V_i for the three experimental groups assuming a significance level equal to 0.05. A Tukey-Kramer test was performed for pairwise comparisons among the three experimental groups.

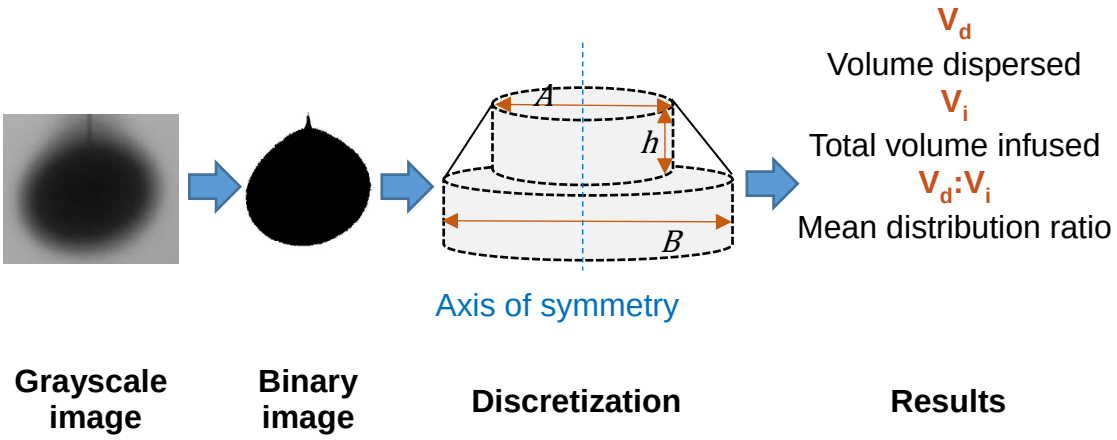

Figure 4.3: Illustration of image processing workflow. Binary images were imported into Matlab and were discretized into frustums of right circular cones to calculate V_d. Using the a priori V_i, the mean distribution ratio V_d:V_i.

RESULTS AND DISCUSSION

Advantage of Seven Ports versus Single-port

Results for volume dispersed and mean distribution ratio using a single-port catheter at 1 µL/min for 100 minutes were 2.36 cm^3 and 23.61, respectively (Figure 4.4). When the flow rate for the single-port catheter was increased seven-fold, the V_d increased by only approximate 117.7% to 5.14 cm3, and V_d:V_i decreased by approximately 69% to 7.34. However, comparisons of V_d and V_d:V_i using the arborizing catheter show that we can achieve a Vd of 10.47 cm3 and V_d:V_i of 14.95 with our current catheter prototype. Compared to the single-port catheter at 7 µL/min, the values for V_d and V_d:V_i achieved with the arborizing catheter were 2 times greater. It is important to note that the total V, across all microneedles in the arborizing catheter, was the same for the arborizing catheter and in the single-port catheter (7 µL/min flow rate) experimental groups. This suggests that the arborizing catheter can achieve significantly ($p < 0.001$) greater volumetric dispersal of the infusate, when it is distributed among 7 microneedles instead of coming out of a single-port. This would be beneficial in CED because it is desirable to

distribute the therapeutic agent throughout the entire tumor volume, including the surrounding tumor margins, to completely target any infiltrative malignant cells.

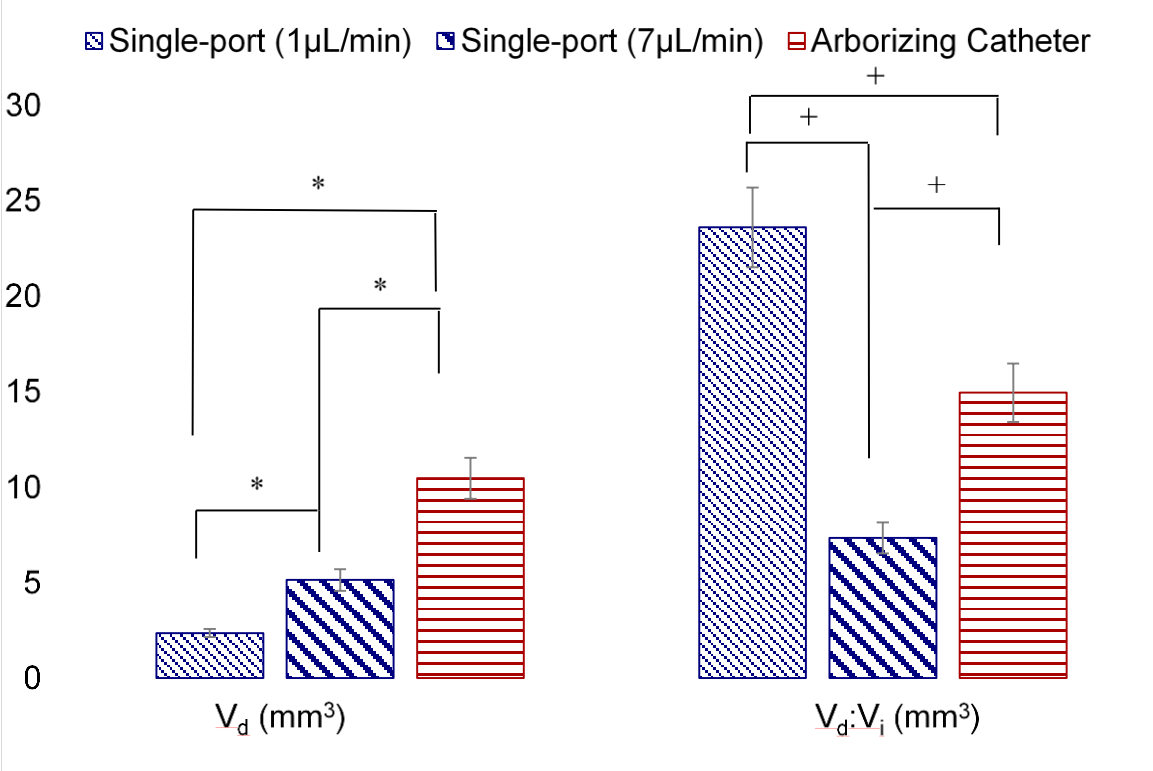

Figure 4.4: Statistical comparisons of average volume dispersed and mean distribution ratio results. A one-way ANOVA test was performed to analyze differences in average volume dispersed (V_d) and average mean distribution ratios (V_d:V_i) after 100 minutes of continuous infusion in agarose tissue phantoms for the three experimental groups: 1) single-port catheter at a flow rate of 1 μL/min; 2) single-port infusions at a flow rate of 7 μL /min; 3) arborizing catheter. A Tukey-Kramer test was performed for pairwise comparisons. Values for V_d were significantly different when each group was compared (*$p < 0.001$). Similarly, values for V_d:V_i were significantly different from each other among the three groups (+ $p < 0.0001$).

A visual representation of V_d for the three groups can be seen in Figure 4.5. In these binary images taken at the final time point of the infusion for each experimental group, the greater V_d achieved with the arborizing catheter can be appreciated. For this sample, the V_d of 12.13 cm^3 obtained after 100 minutes is equivalent to coverage of a

spherical volume with a 2.8-cm radius. The single-port catheter at the slower flow rate (1 μL/min) resulted in the lowest V_d value. This is expected because the overall V_i for that group was seven-times lower than for the single-port catheter at the higher flow rate (7 μL/min) and for the arborizing catheter groups. However, it can be appreciated that even though the total infused volume for the single-port group at the highest flow rate (7 μL/min) and the arborizing catheter were the same, the resultant volume dispersed was greater for the arborizing catheter.

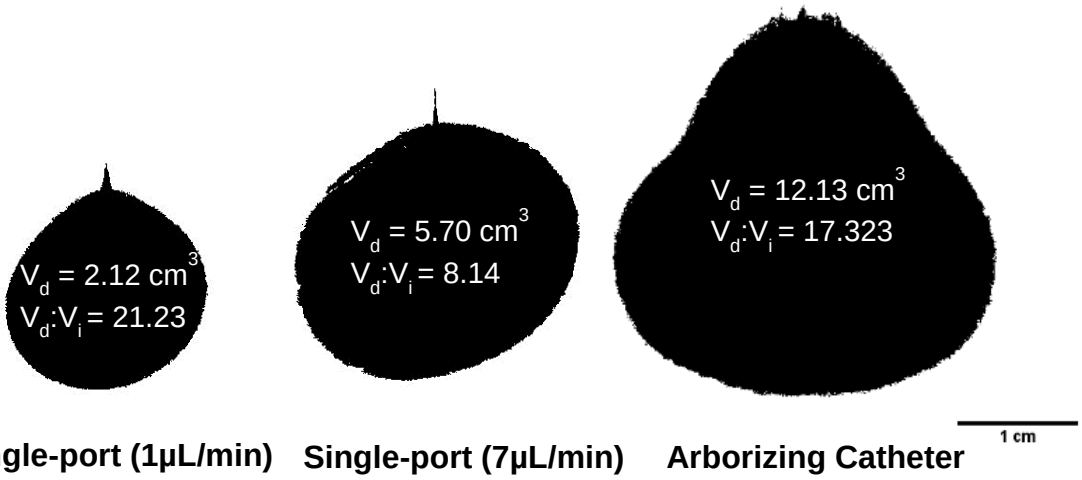

Figure 4.5: Representative volume dispersed for each experimental group after 100 minutes of continuous infusion. All images are of the front view captured directly by the DSLR camera. The volume dispersed (V_d) and mean distribution ratios (V_d:V_i) were calculated using an algorithm that discretizes the volume into elementary frustums of right circular cones [164]. The final volume is calculated by summing the volumes of all the frustums.

It's noteworthy to discuss that in these experiments, the agarose gel was casted around the microneedles and the single-port catheter in order to minimize reflux. Although this simplified model is not reflective of the real-life scenario in which the catheters would be inserted into tissue, this method allowed for the high flow rates used

in the study without loss of infusate due to reflux. Therefore, all the infused volume was distributed into the agarose gel and calculations of V_d and V_d:V_i were straightforward without having to account for reflux. However, more realistic experiments in which the microneedles of the arborizing catheter were deployed into tissue are described in Chapter 6.

V_d:V_i versus Time Indicates Overlap in the Infusion Distribution

Although the single-port catheter (1 µL/min) group showed the lowest V_d, it resulted in the highest V_d:V_i of the three groups. In comparison to the arborizing catheter group, the catheter is composed of 7 microneedles, with each individual microneedle representing a single-port (each at a flow rate of at 1 µL /min). However, at the end of the 100 min-long infusion, the overall V_d:V_i for all the microneedles of the arborizing catheter resulted in an approximately 37% lower mean distribution ratio compared to single-port catheter at the slower flow rate (1 µL/min). The V_d:V_i over time is shown in Figure 4.6 for the three experimental groups. The V_d:V_i for the arborizing catheter group is similar to that of the single-port at the slower infusion rate of 1 µL/min at the early time point, however it begins to decline and eventually becomes lower than the single-port (1 µL/min) group by 60 minutes of continuous infusion. This could be explained due to the likely overlap in the local infusions from individual microneedles as they become larger with time. It is likely that at the beginning of the infusion, the overlap of the individual volume provided by each needle is less pronounced, therefore the V_d:V_i is similar to that of the single-port catheter. However, as the volume dispersed from individual needles start to become bigger and merge with one another into one large volume, the benefit gained from the multiple ports in the arborizing catheter is reduced until eventually the V_d:V_i becomes less than that of a single-port catheter. The single-

port (7 μL/min) group, which has the lowest V_d:V_i, further supports the concept of overlap as it shows the dye, concentrated in a smaller volume, causes the mean distribution volume to plateau quickly during the infusion and stays relatively constant after approximately 20 minutes of continuous infusion.

The slower flow rate achieved the highest V_d:V_i, which can be thought as a measure of the "efficiency" of the infusion. It has been noted that macromolecular transport is sensitive to changes in tissue permeability due to perfusion-induced tissue deformations (e.g. reduced pore size)[165]. Therefore, it is likely that higher flow rates induce greater local deformation and strain at the infusion site, which would result in reduced hydraulic permeability and lower V_d:V_i compared to the slower flow rate. Clinically, infusion protocols implementing slower flow rates may be safer, not only to prevent reflux associated with higher flow rates, but to reduce damage to local tissue near the infusion site due to perfusion-induced deformations in the tissue.

We observed that, once deployed, the separation distance of the individual microneedles of the arborizing catheter affects the amount of overlap between the local infusions of each microneedle and influences the measured V_d. For this arborizing catheter prototype, the separation distance was approximately 0.5 cm. Based on the results from this study, such separation distance between adjacent needles was inefficient and contributed to the lower V_d:V_i values for the arborizing catheter group compared to the single-port catheter at slower flow rates. In the next chapter, a computational study was utilized to optimize the catheter design, by comparing the effects of separation distance of adjacent microneedles on infusion volume overlap in order to improve V_d:V_i.

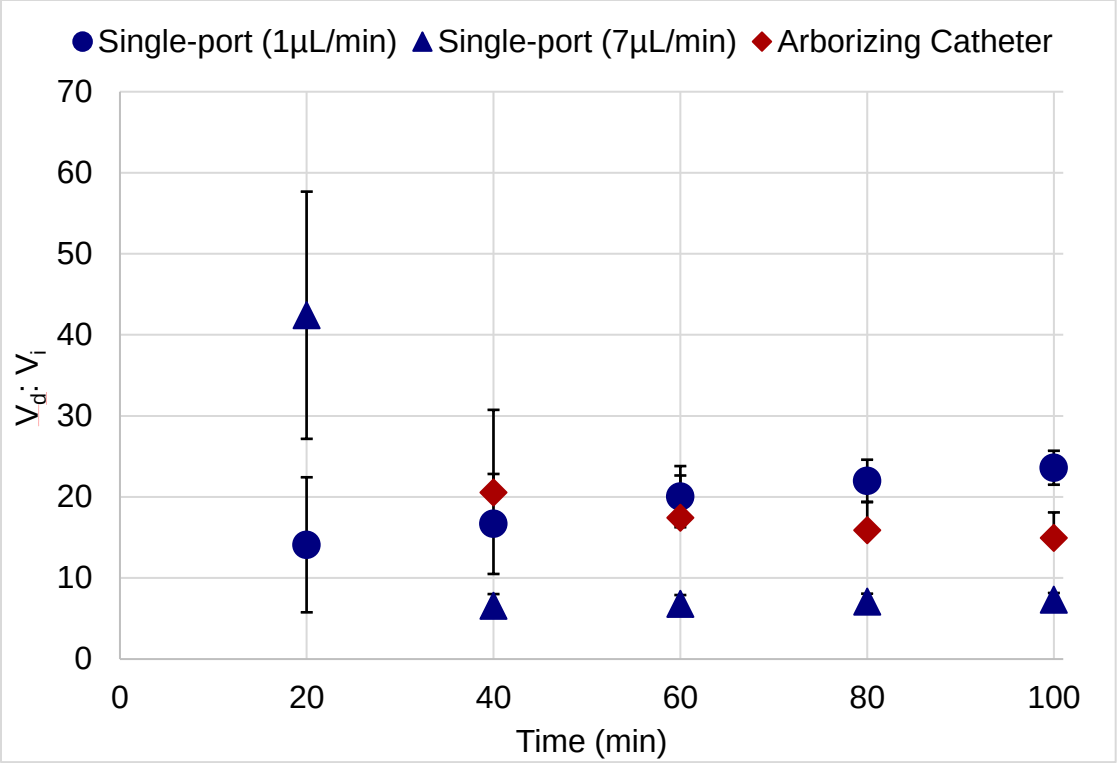

Figure 4.6: Mean distribution ratios (V_d:V_i,) versus time of infusions for the three experimental groups. The average V_d:V_i, for each group was calculated every 20 minutes. However, the image processing algorithm was limited to calculating volume of solid, axisymmetric shapes and could not reliably calculate the volume of infusions shapes with gaps or holes. Therefore, infusions in the arborizing catheter group were calculated at 40 minutes and beyond, after the infusion shapes of individual microneedles had overlapped sufficiently to form a solid shape.

It is important to note that our image processing algorithm was not able to reliably calculate V_d for the arborizing catheter at time points less than 40 minutes. This is because we assumed that the infusion volume was axisymmetric about the axis of the primary cannula of the arborizing catheter and thus, it was not able to account for any amorphous shapes or holes in the infusion volume. Figure 4.7 shows binary images of three representative time points in the infusion of an arborizing catheter. After 10 minutes of continuous infusion the dispersed volume from individual microneedles is clearly

discernable. At 20 minutes, there are still gaps present in the volume dispersed. However, after 40 minutes, most gaps in the volume dispersed had been filled and a reliable calculation for V_d could be obtained.

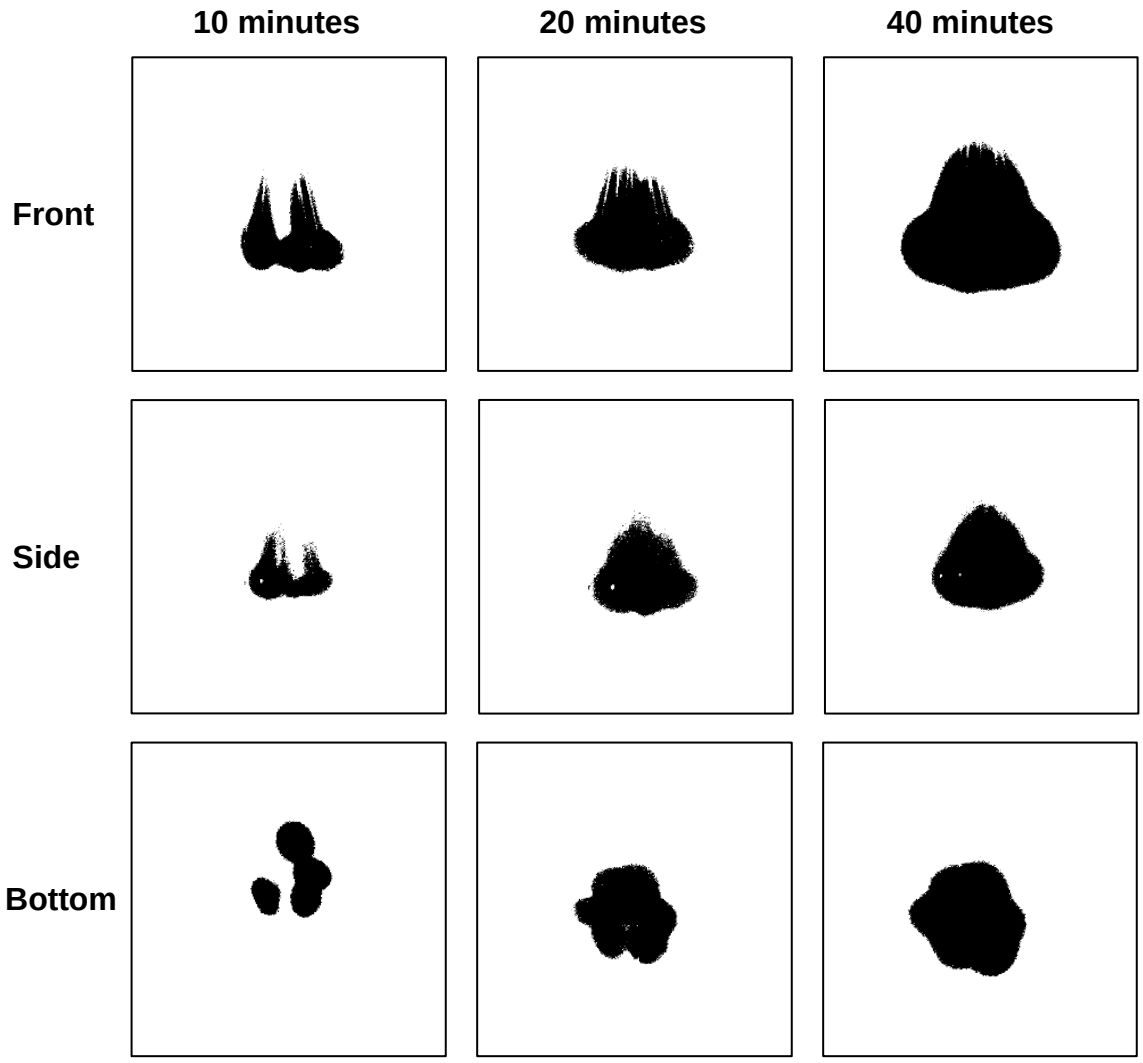

Figure 4.7: Representative binary images of volume dispersal for the arborizing catheter at three time points during the infusion for three view frames. The images show that at time points below 40 minutes, there were gaps in the dispersed volume due to branching out of the microneedles in the arborizing catheter. As the individual infusion volumes from each microneedle grew and began overlapping each other, the gaps were filled.

CONCLUSIONS

Results indicate that the multiport, arborizing catheter can significantly enhanced volumetric dispersal of the infusate over a single port. By separating the volume infused, the arborizing catheter achieved a two-fold, greater volumetric dispersal and mean distribution volume compared to a single-port catheter for the same total infused volume. When comparing infusions of the arborizing catheter to that of a single-port catheter at the same flow rate per microneedle, the mean distribution ratio for the arborizing catheter drops to approximately 30% less than the single needle perhaps due to overlap in the individual volume dispersed of the seven microneedles of the catheter. In the next design iteration, separation of individual microneedles within the arborizing catheter will be optimized to minimize overlap in the infusion volumes of individual microneedles (but, with no gaps in between them), while maximizing volumetric dispersal.

Chapter 5: Optimization of the Arborizing Catheter using a Biphasic Computational Model to Enhance Dispersed Infusion Volume

Introduction of Computational Models

Computational models to study the transport of the infused drug within the brain tissue are tools that can provide insights for informed-design of CED catheters and treatment protocols to achieve the necessary broad distribution of drugs in the affected brain tissue. Several mathematical models, varying in degree of complexity, have been used to study drug infusion into central nervous tissue. An analytical model of pressure-driven infusion in a cavity surrounded by infinite porous media was presented by Basser [166] and Barry and Aldis [167] to study the fluid transport and tissue deformation that occurred during the infusion. This model was able to predict interstitial (pore) pressure, radial fluid velocity and dilatation of the solid matrix following a step change in pressure within the infusion cavity, but did not incorporate solute transport. Chen and Sarntinoranont [168] later expanded on the existing model and derived the analytical solution for radial displacement of the solid matrix.

Morrison *et al.* [158] presented a simple model to describe transport of solutes in isotropic gray matter due to high-flow infusion; however, the brain was modeled as rigid porous media and the effect of solid deformation (i.e. tissue swelling and edema) induced by the infusion were neglected. Patient-specific models that incorporate diffusive tensor imaging data, but treat the brain tissue as a rigid solid, have also been used to predict the macromolecular distribution of the infusate within the brain parenchyma [169], however significant deformation has been observed during CED based on feedback from real-time MRI surveillance [170]. Other models couple fluid transport and solid deformation based on biphasic theory, poroelastic or poroviscoelastic theory [168, 171-175]. Using the finite element method, Chen and Sarntinoranont [168], and Garcia and Smith [171]

investigated pressure-driven solute transport in linear elastic and hyperelastic material properties, respectively. In these models, both research groups prescribed a constant pressure to the inner boundary of the infusion cavity inducing water and solute transport within a spherical mesh. They coupled the effects of tissue swelling including deformation-dependent hydraulic conductivity to study the solute distribution due the prescribed infusion pressure at the cavity. While, Chen and Sarntinoranont assumed linear elasticity for the solid phase of their model, Garcia and Smith used a custom-written finite element code to implement the nonlinear material properties of brain tissue.

In conventional CED studies, the drug is delivered at a constant flow rate using a programmable syringe pump. A constant prescribed infusion pressure may not indicate realistic conditions during CED simulations. Therefore, Netti *et al*. [172] presented an analytical solution for a flow-driven, biphasic model, using linear elasticity to represent the solid phase, and coupled the model to a macromolecular transport numerical model. Using Netti's model, Smith and Garcia [173, 174] validated their custom-written finite element model to study flow-driven fluid and mass transport in the brain considering nonlinear material properties under finite deformation, mechanically dependent hydraulic conductivity and convection-diffusion transport of the infused solution. Similar to previous models, a spherical geometry with an embedded infusion cavity was used to represent the brain. Traction on the infusion cavity is equal to the interstitial pressure, which contributes to solid deformation of the infusion cavity. However, unlike pressure-driven models, interstitial pressure at the boundary is unknown initially in flow-driven models. Therefore, to account for the nonlinear boundary condition, Smith and Garcia proposed a fixed, artificial boundary consisting of highly permeable and compliant elements, in which a constant radial fluid velocity was prescribed in order to guarantee a constant infusion flow rate.

Using computational models to test various design concepts is an economical and effective approach to optimize the design of the arborizing catheter. Thus, the goal of this study is to use computational models to simulate infusion conditions and parametrically explore how the separation distance of adjacent microneedles in the arborizing catheter and flow rates affect volume distribution. As the first iteration of this model, pressure-controlled infusions were compared to experimental data of infusion in agarose gel presented in Chapter 4.

METHODS

Biphasic with Solutes Theory

The biphasic-solute model, based on the theory of incompressible mixtures, consists of a permeable solid matrix, a solvent and a solute. The volume fraction of the solute was assumed negligible relative to the solid and solvent fractions. In addition, the friction within the fluid (i.e. solvent and solute viscosity) is assumed negligible relative to the friction between the solid and solvent (i.e. permeability). Additionally, quasi-static conditions were assumed. The complete derivation of the governing and constitutive equations is described elsewhere [176-179].

In this biphasic finite element (FE) model, the solid phase representing the porous tissue phantom made from 0.6% (w/w) agarose gel is denoted as $\alpha = s$, the solvent representing deionized water is denoted as $\alpha = w$, and the solute/infusate representing indigo carmine is $\alpha = a$ (MW ~ 446 Da). All constituents are assumed to be neutrally charged and intrinsically incompressible, thus the true density (ρ_T^α) is invariant for each constituent. Following the notation by Gu *et al.* [180], and using the generalizations for the balance of linear momentum equations, along with the constitutive equations for the mixture stress, and the solvent and solute electrochemical potentials presented in Mauck

et al. [176], the following momentum equations for the mixture, solvent and solute, respectively:

$$-\text{grad}p + \text{div}\boldsymbol{\sigma}^e = \mathbf{0} \tag{1}$$

$$-\varphi^w(\text{grad}p - R\theta\ \text{grad}c) + f_{ws}(\boldsymbol{v}^s - \boldsymbol{v}^w) + f_{wa}(\boldsymbol{v}^a - \boldsymbol{v}^w) = \mathbf{0} \tag{2}$$

$$-\varphi^w R\theta\ \text{grad}\ c + f_{sa}(\boldsymbol{v}^s - \boldsymbol{v}^a) + f_{wa}(\boldsymbol{v}^w - \boldsymbol{v}^a) = \mathbf{0} \tag{3}$$

where, p is the fluid pressure, $\boldsymbol{\sigma}^e$ is the elastic solid stress in the matrix, φ^w is the volume fraction for the solvent, R is the universal gas constant, θ is the absolute temperature and c is the concentration of the solute on a solution-volume basis. Additionally, $\boldsymbol{v}^\alpha$ is the velocity of the constituent α and $f_{\alpha\beta}$ is the diffusive drag force between the constituents α and β (with $f_{\alpha\beta} = f_{\beta\alpha}$). The non-zero diffusive drag coefficients are related to the hydraulic permeability (k) of the solvent through the solid matrix, the solute diffusivity in the mixture (D), and the solute diffusivity in the free solution (D_0) by:

$$f_{ws} = \frac{(\varphi^w)^2}{k}, f_{wa} = \frac{\varphi^w R\theta c^\alpha}{D_0}, f_{wa} + f_{sa} = \frac{\varphi^w R\theta c^a}{D} \tag{4}$$

The governing equations for mass balance of the mixture, solvent and solute phases, in the absence of chemical reactions, are:

$$\text{div}\ (\varphi^s \boldsymbol{v}^s + \varphi^w \boldsymbol{v}^w + \varphi^a \boldsymbol{v}^a) = 0 \tag{5}$$

$$\frac{\partial \rho^\alpha}{\partial t} + \text{div}(\rho^\alpha \boldsymbol{v}^\alpha) = 0, \alpha = w, a \tag{6}$$

where, $\rho^\alpha = \varphi^\alpha \rho_I^\alpha$ is the apparent density for the constituent α, and φ^α is the volume fraction for each constituent. Inverting the balance of linear momentum equations (Eq.2-3) yield expressions for the volumetric fluid flux, $\varphi^w(\boldsymbol{v}^w - \boldsymbol{v}^s)$, and solute molar flux, $\varphi^w c\ (\boldsymbol{v}^a - \boldsymbol{v}^s)$, as a function of their respective driving forces utilizing relations of the permeability and diffusivity to diffusive drag coefficients described in Ateshian *et al.* [178], and Maas *et al.* [181]. Such relationships represent generalized versions of Darcy's

law for fluid transport through porous media and Fick's law for solute diffusion in free solution and in porous media.

Model Validation

To validate the above model, V_d of indigo carmine dye in agarose from infusion experiments were compared to numerical predictions of solute dispersal in a biphasic medium from pressure-driven infusion simulations. The geometry for the model consists of a cube with an embedded spherical cavity of initial radius r_o = 0.18 mm, which corresponds to the inner diameter of a 28-gauge hypodermic needle. The solid matrix is modelled as a homogeneous, isotropic, neo-Hookean solid with a modulus of elasticity (E) of 6 kPa and a Poisson's ratio (v) of 0.4 [182]. The solid volume fraction (φ^s) is based on the volume fraction of fibers for the 0.6% agarose gel [183]. Consistent with literature reports, the hydraulic permeability tensor is modelled as a function of local porosity changes [184]. Specifically, the following relationship proposed by Holmes-Mow for the strain-dependent permeability tensor is used:

$$\boldsymbol{k} = k_0 \left(\frac{J-\varphi_0}{1-\varphi_0}\right)^{\beta} e^{M(J^2-1)/2}\,\mathbf{I} \tag{7}$$

where, k_0 is the isotropic hydraulic permeability in the reference state, M is the exponential strain-dependence coefficient, β is the power-law exponent and J is the Jacobian of the deformation gradient, i.e. J = det ($\boldsymbol{F}$). In the absence of literature data, k_0 = 4.5 mm^4/N·s, β = 0, and M = 1 were selected based sensitivity analyses. Free and effective diffusivity are assumed nearly equivalent and prescribed a value of 6.0x10^{-4} and 5.4x10^{-4} mm^2/s, respectively, based on the molecular size for indigo carmine and extrapolated for room temperature (298 K) using Einstein's relation for diffusivity [185].

For the model, all the outer tissue surfaces are exposed boundaries to ambient pressure (zero interstitial pressure and traction free boundary conditions). Taking

advantage of symmetry, only an eighth of the geometry was considered for the simulations. The boundary conditions at the symmetry faces include zero displacement, fluid flux and mass flux. Similar to Chen and Sarntinoranont [168], zero contact stress ($\sigma^e = 0$) was applied to the solid matrix at the porous-fluid interface. To guarantee continuity across element boundaries, the effective fluid pressure ($\tilde{p}$) rather than the interstitial fluid pressure (p) was prescribed, where $\tilde{p} = p - R\theta\phi c$, R is the universal gas constant, θ is absolute temperature, ϕ is the osmotic coefficient, and c is the solute concentration [179]. Infusion pressure (i.e. the effective fluid pressure) was prescribed to the spherical boundary of the cavity to induce an average flow rate of approximately 1 μL/min and 7 μL/min and compared to experimental data [150]. Infusion pressure was ramped rapidly with ramp time (t_0) of one second and held constant for the duration of each simulation. Solute concentration is only continuous across an interface in the case of ideal solubility, thus the effective solute concentration ($\tilde{c}$) is solved for instead [186]. This study assumed ideal solubility, therefore they are equivalent. The arising boundary value problem was solved with FEBio (version 2.6.4; www.febio.org).

PreView (version 1.20; www.febio.org) was used to create a mesh consisting of 8-node trilinear hexahedral elements with a mesh bias toward the infusion cavity. The effective solute concentration present in the solid was compared to the prescribed concentration at the infusion cavity in a mesh convergence study. Increasing the number of elements decreased the percent error between the prescribed concentration and the max concentration of elements at the boundary of the infusion cavity. A mesh with 1296 elements, biased toward the infusion cavities, resulted in less than 1% error for the simulations. Thus, meshes for the all simulations were at least 1296 elements.

The effective solute concentration values given by the FE solution were normalized and a threshold of 0.1% of the normalized effective solute concentration ($\tilde{c}_n$)

were used to calculate V_d. The chosen threshold was based on experimental calibration of grayscale intensity threshold values to known serial dilutions of 5% (w/w) stock concentration of indigo carmine with 0.6% agarose gel. This resulted in uniform gels of known concentrations of indigo carmine ranging from 0-1% of the stock solution. Images were taken of the gels in similar lighting as the experimental infusions. These were then converted into grayscale images normalized to an intensity values ranging from 0.0 (black) to 1.0 (full intensity or white). Global intensity threshold values were calculated (using a Matlab algorithm based on Otsu's method) for each image. The calculated V_d from the simulations for time 20-100 min were compared with derived V_d from experiments for the same infusion times.

Optimization Simulations

After the validation of the FE model, simulations were performed to optimize the placement of two individual ports in a multiport catheter. The model geometry was adjusted to include two infusion cavities, representing catheter source ports (Figure 5.1). The sources are spaced along the x-axis at a separation distance (d) ranging from 0.5-2.0 cm, measured from the center of each cavity. The y, z length dimensions for the cube are equal to the separation distance, which was approximately 275-times greater than r_o. This ensures that changes in interstitial pressure, displacement and fluid velocity are negligible beyond such a distance from the infusion site [159, 172].

Magnitude for the infusion pressure was varied between 1-4 kPa depending on the experimental protocol. At the higher infusion pressures, lowering v helped achieve convergence of the model. Thus, v ranged from 0.35 to 0.4. Additionally, a constant effective solute concentration was prescribed at the spherical boundary of the cavities. Table 5.1 presents a summary model parameters used for this study.

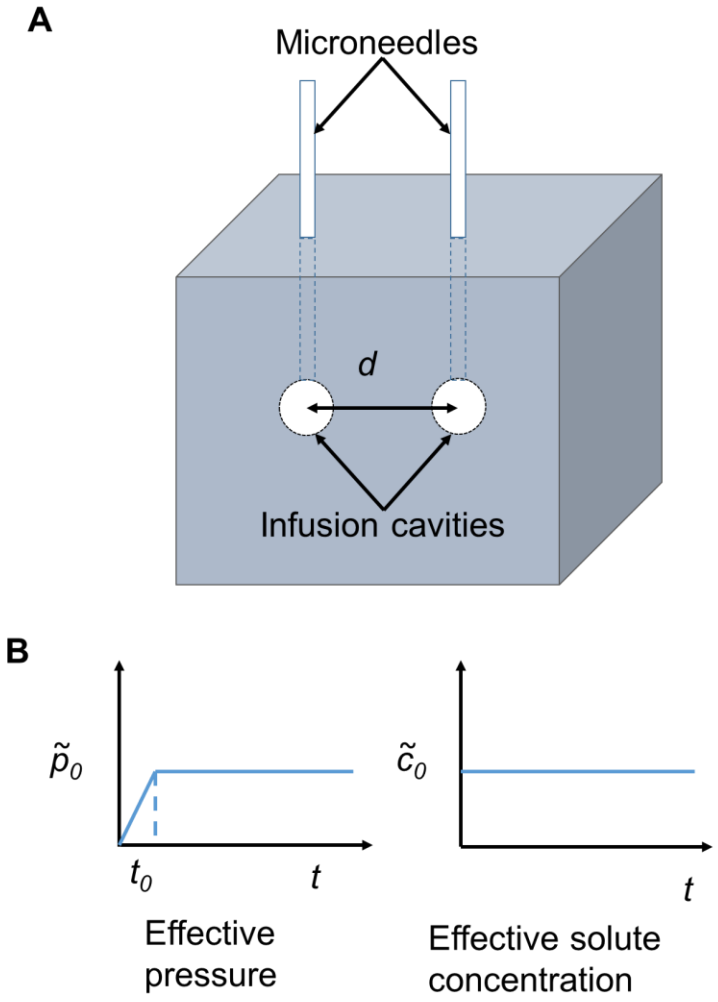

Figure 5.1: A) FE model geometry of biphasic solid with two embedded infusion cavities (i.e. source ports). B) Constant infusion pressure applied at a rapid ramp time of t 0 and constant effective solute concentration were applied at inner surface boundary of the infusion cavities. Zero interstitial pressure and traction free surface boundary conditions were applied at the outer boundaries of the solid.

Parameter	Value
Young's modulus, E	6000 Pa
Poisson ratio, *v*	0.35-0.4
Initial hydraulic permeability, k_0	5.0 $mm^4 N^{-1} s^{-1}$
Nonlinear hydraulic permeability parameter, M	1
solid volume fraction, φ_s	0.006
Free Diffusivity, D_o	6.0 x 10^{-4} $mm^2 s^{-1}$
Effective Diffusivity, D	5.5 x 10^{-4} $mm^2 s^{-1}$
Temperature, T	298 K
t_0	1 s
$\tilde{p}_0$	1 – 4 kPa
d	0.5 – 2 cm
MW, indigo carmine	466 Da

Table 5.1: Summary of baseline parameters used for model.

The volumetric flow rate were calculated utilizing the resultant deformation of the infusion cavity per time step and the flux with the current surface area of the cavity. Because the volumetric flow rate is a function of time, the values were averaged from t_0 to 100 minutes for each simulation. Additionally, T_{c50} was defined and computed as the infusion time to reach 50% of the max-prescribed concentration at the mid-point between the two infusion cavities.

RESULTS

Figure 5.2A shows the intensity threshold values corresponding to the known diluted concentrations of the dye stock solution. The intensity threshold used to calculate V_d in in infusion experiments was 0.22 ± 0.03, which corresponds to a concentration of 0.09% of the stock solution. Therefore, 0.1% of the normalized effective concentration was used as a threshold to calculate V_d in the FE simulations. V_d values were calculated

from simulations for continuous infusion ranging from 20-100 min and compared with single-port experimental infusions as shown in Figure 5.2B. The simulation with the average flow rate of 0.99 μL/min and single-port experiments (conducted at a flow rate of 1 μL/min) indicate good agreement at all time points. The percent difference between the average V_d for experiments and the FE model is less than 4%, for times 60-100 minutes, but is higher at earlier time points. For the 20-min and 40-min time-points the percent difference is 11.0% and 6.0%, respectively. However, this difference falls below one standard deviation of the measured experimental values. Similarly, V_d derived from the FE simulation with an average flow rate of 6.92 μL/min were compared to the V_d measured for single-port infusion experiments at 7 μL/min. They also show good agreement with a percent difference of less than 5.5% for all time points.

Figure 5.3 shows the prescribed infusion pressures ranging from 1-4 kPa versus the resultant average flow rates calculated after the rapid ramp time of 1 sec and up to 100 min. Consistent with Chen and Sarntinoranont, the predicted relation between infusion pressure and the average flow rate was nonlinear. Small changes in infusion pressure resulted in greater changes in the average flow rate. The minimum flow rate achieved by 1 kPa was 0.72 μL/min and the maximum flow rate, 8.48 μL/min, was achieved at the infusion pressure of 4 kPa. By comparison, clinically relevant flow rates for CED range from 0.5 – 10 μL/min [85, 103, 117-119, 159]. Infusion pressure of 1300 Pa and 3500 Pa resulted in an average flow rate of 0.99 μL/min and 6.92 μL/min, respectively. These results were the infusion pressures used for validating the model by comparing with infusion studies performed at a constant flow rate of 1 μL/min and 7 μL/min. The percent error between the average flow rates from the FE simulation and the experimental flow rates is 1.14% and 1.04% for the 1 μL/min and 7 μL/min, respectively.

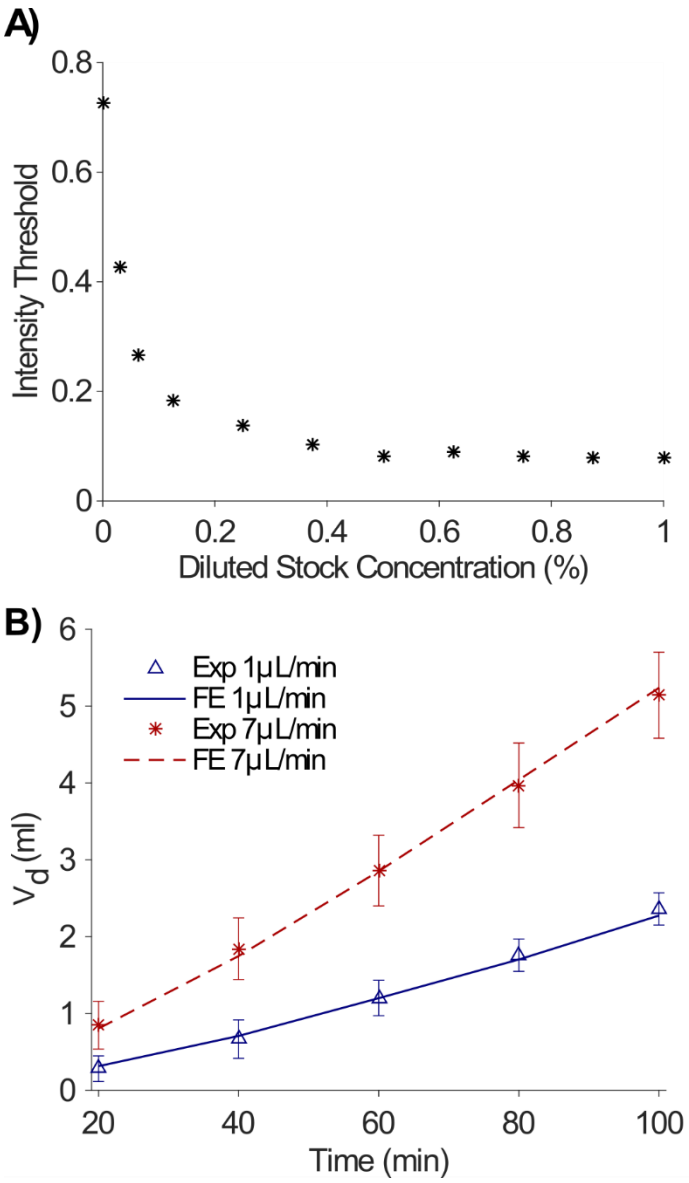

Figure 5.2: A) Indigo carmine stock solution (5% w/w) was serially diluted from 1:100 in agarose gel solution and plotted as percentages versus their corresponding grayscale intensity threshold values from post processed images. B) Volume dispersed (V d) in ml versus time in minutes for finite element (FE) simulations compared to infusion experiments (Exp). Average flow rate for FE model slow was 0.99 µL/min versus flow-controlled infusion with constant flow rate of 1 µL/min. Conversely, the average flow rate of the FE model fast was 6.92 µL/min versus flow-controlled infusion with constant flow rate of 7 µL/min.

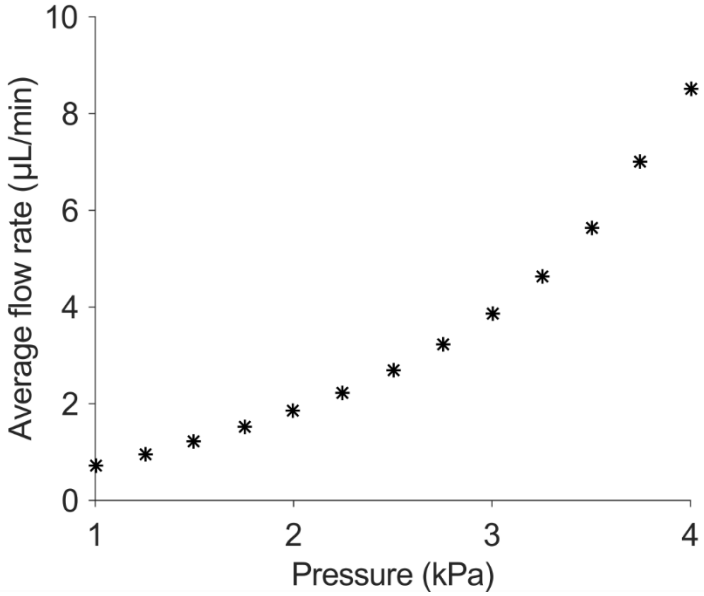

Figure 5.3: Prescribed infusion pressure versus resultant average infusion flow rates. Flow rates were calculated after the infusion pressure was applied to the boundary of the infusion cavity.

Given the pressure to flow rate relationship, four different flow rates were selected to calculate the mean distribution ratio (V_d:Vi) as a function of infusion time. Results show that slower flow rates resulted in greater V_d:Vi, or are more efficient infusions. This is consistent with results previously reported in the literature and are consistent with the experimental results shown in Chapter 4 [174]. One potential mechanism for this phenomenon is the mechanically-dependent hydraulic permeability prescribed in the model. Slower flow rates may be associated with reduced deformation of the infusion cavity and smaller porosity (volume fraction of fluid) allowing for greater distribution of the solute. From a clinical perspective, slower flow rates are potentially safer as they are associated with less tissue deformation that may result in damage and are less prone to induce reflux of the therapeutic [96, 139, 159].

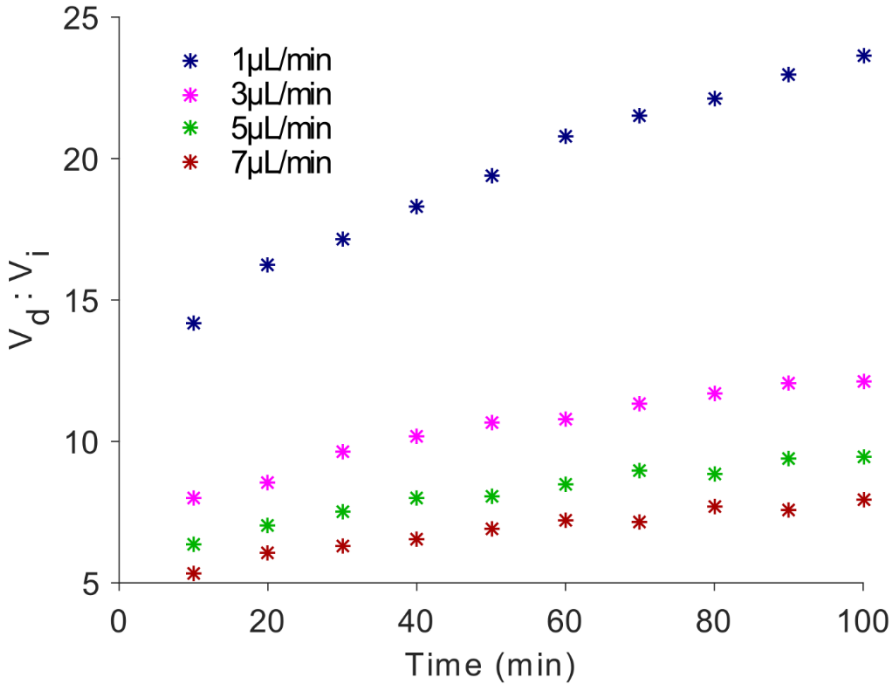

Figure 5.4: Mean distribution ratios (V_d:Vi) plotted versus time (min) calculated for infusion simulations at infusion flow rates ranging from 1 to 7 μL/min . The results indicate that slower infusions result in greater V_d:Vi.

Figure 5.5 demonstrates simulation results for infusion pressures ranging from 1-4 kPa for infusion cavities spaced 1.5 cm apart (center to center). Due to symmetry, only an eight of the geometry is represented in the model. The two infusion cavities are shown in the bottom corners. Contour plots show the spatial distribution of $\tilde{c}_n$ at 300 minutes of continuous infusion. At this time, the simulations prescribed 1 kPa and 2 kPa show an area between the two source ports in which the $\tilde{c}_n$ is below 0.1. For these infusions, 300 minutes of continuous infusion would not be sufficient for complete coverage of the volume target if a concentration greater than 0.1 or 10% of the infused therapeutic were required for efficacy. At 300 minutes, some overlap in the spatial distribution of the solute concentration between the two sources is demonstrated for the 3 kPa case. Finally,

the 4 kPa case achieves significant overlap between the two sources with concentrations greater than 0.5 $\tilde{c}_n$.

For each simulation, the calculated T_{c50} indicate the time at which the concentration overlap between the sources reached 0.5 or 50% of the prescribed concentration at the infusion cavities. Figure 5.6 shows a summary of the parametric results indicating T_{c50} values (in hours) as a function of microneedle/port spacing for various flow rates. As the separation distance increases from 0.5-2.0 cm, V_d increases. However, T_{c50} drastically increases as shown by the two orders of magnitude change in the logarithmic scale of the y-axis (approximately by 100 hours). Lowering T_{c50} to a more manageable total procedure time would require infusion flow rates to be increased. For example, increasing infusion pressure from 1 to 4 kPa will result in 8-times higher flow rate, which would decrease the T_{c50} by approximately 32 hours. This is at the cost of lowering V_d:V_i as we found in infusion experiments and simulations.

In this study, T_{c50} was defined as 0.5 of the normalized solute concentration at a point midway between the two sources. However, this concentration is somewhat arbitrary as the minimum effective dose required is therapeutic-specific. Therefore, a separate analysis was performed to understand the time required to reach a distribution overlap at various solute concentrations between the source ports. Figure 5.7 shows the time, in hours, required for the solute concentration overlap ranging from 0.1-0.5 for ports spaced 0.5-2.0 cm apart and infusion pressures ranging from 1-4 kPa. Prescribed infusion pressures, and subsequently, the average flow rate of the infusion, have a greater influence at higher concentration thresholds and at greater separation distances between the source ports. Additionally, doubling the separation distance between the ports achieves approximately a ten-fold increase in time required to reach the specified concentration.

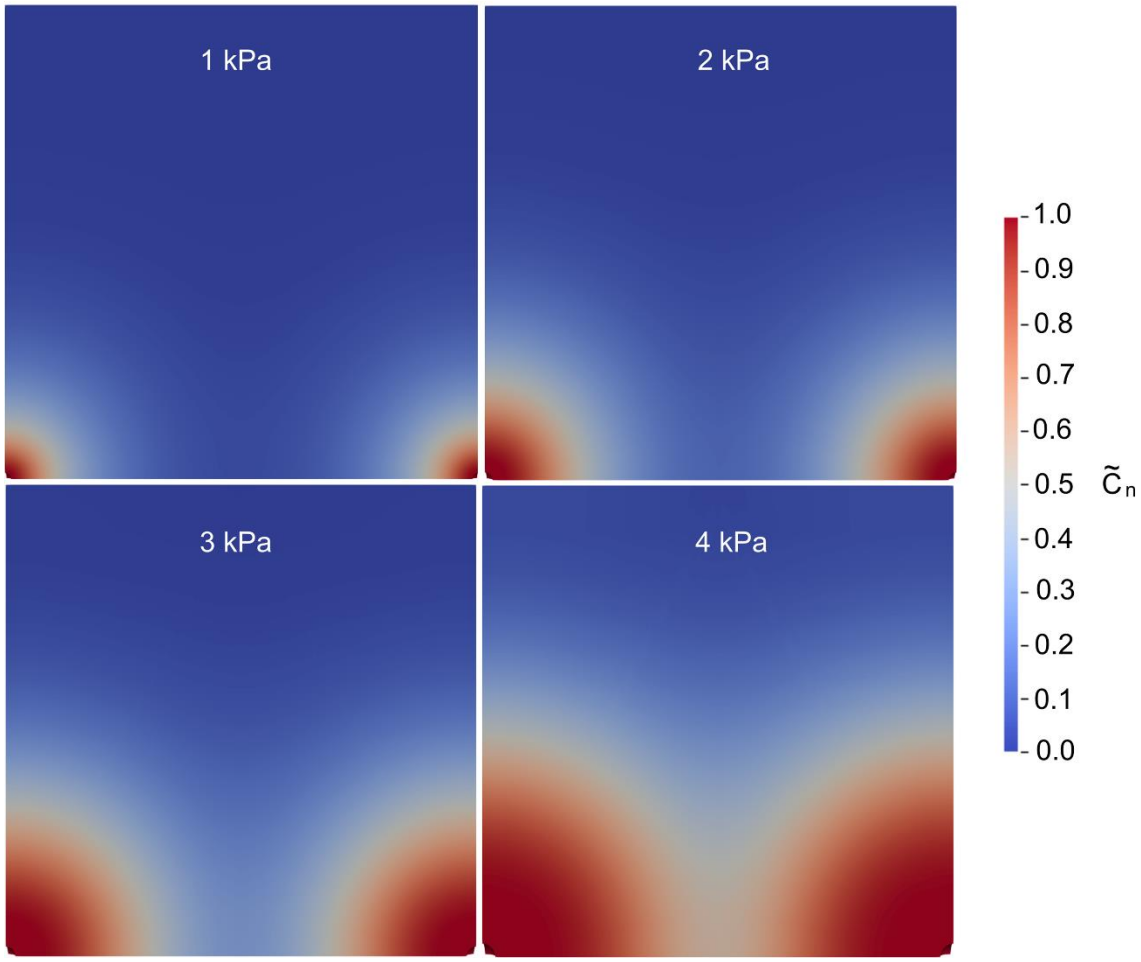

Figure 5.5: Representative color map for simulation with source ports (infusion cavities) spaced 1.5 cm apart. The color map shows the normalized effective solute concentration at time = 300 min.

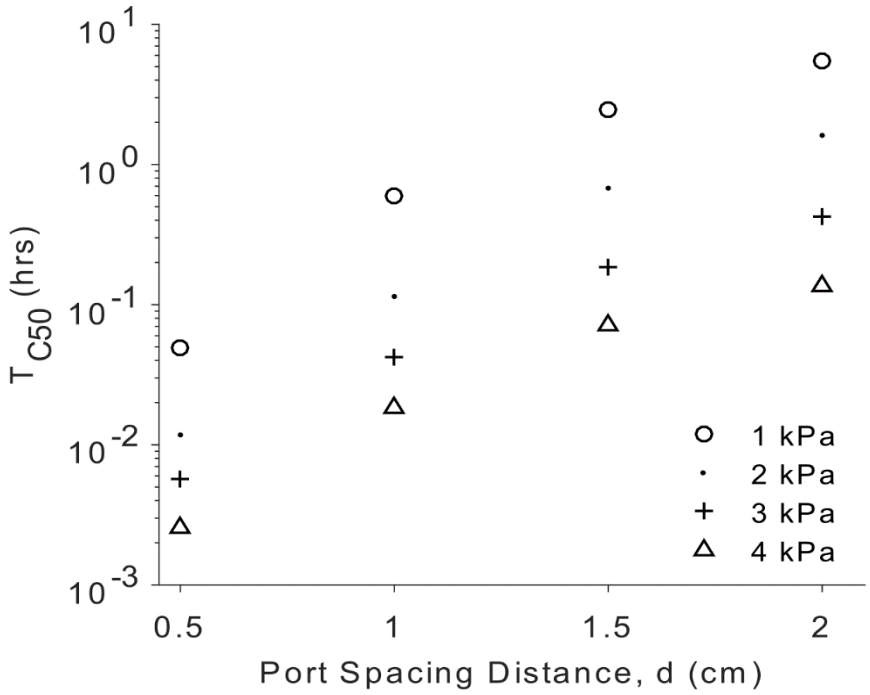

Figure 5.6: Time (in hours) required for normalized effective concentration between sources to reach 0.5, Tc50, vs the source separation distance in cm.

DISCUSSION

Maintaining the treatment duration within a manageable period is important for a number of reasons. Chronic CED may be beneficial to achieve large V_d, even with lower infusion rates; however, it has not gained wide acceptance and has only been performed in humans outside of the United States. Due to the highly invasive and permanent nature of the procedure, it requires highly specialized infusion equipment for long-term use. Short-term infusions seems to be the more common approach to CED. In the PRECISE trial, IL13-PE38QQR was administered over 96 hours using 2 to 4 catheters at a total flow rate of 12.5 μL/min, which would result in a flow rate ranging from 3.13 to 6.25 μL/min per catheter [85]. Even if the infusion is continuous over a period of days, it does not guarantee that the therapeutic reaches all the affected tissue as revealed in the study

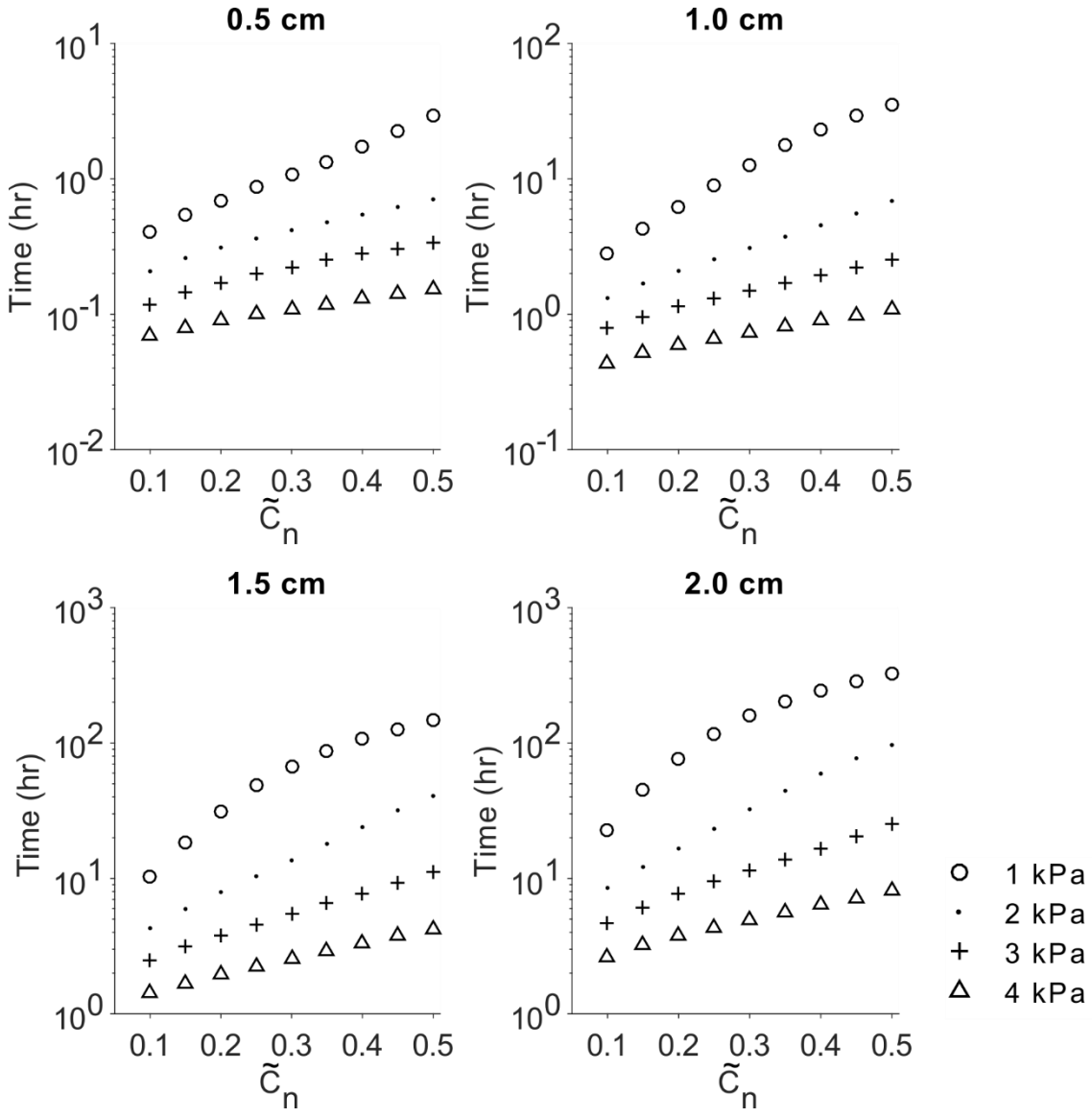

Figure 5.7. Time to reach a concentration overlap (ranging from 0.1 to 0.5 of the normalized effective solute concentration) midway between two sources for port separation distance ranging from 0.5 to 2.0 cm.

conducted by Sampson *et al.* [130]. Therefore, a more effective approach could be to co-infuse the therapeutic with an imaging marker and perform CED under continuous imaging surveillance such as with MRI. Feedback of the spatial distribution of the therapeutic can help guide the therapy to ensure proper coverage of the intended volume

target [106, 136, 187]. Although this method would be an improvement over "blind" CED, the cost associated with continuous time in the MRI scanner room would undoubtedly increase the overall cost of treatment. Therefore, optimizing the treatment duration would help reduce the cost of the treatment. Additionally, shorter treatments could reduce risk of infection exposure and discomfort to patients.

A second option to decrease time of treatment is to decrease the distance between the two ports, however that would also reduce V_d. Thus, in order to maintain good coverage of a given tissue volume, more ports would be required, which supports the advantage of using a multiport catheter. Finally, infusing at higher flow rates may help decrease infusion time, but it comes at the expense of reducing V_d:V_i [174] . However, given the high recurrence rates of GBM, maximizing V_d to ensure treatment of infiltrated disease may be more important than maximizing V_d:V_i. With development of targeted drugs and drugs with a wide therapeutic index, peripheral damage of healthy brain tissue is less of a concern when attempting large V_d [188-190]. Nevertheless, higher flowrates are associated with adverse effects such as reflux of the infusate along the catheter insertion tract [159].

The prescribed material properties in the model are based on agarose gels given that the model was validated using experimental data from infusions in agarose tissue phantoms. Although agarose has been commonly used as a substitute for brain tissue in infusion studies [191, 192], the isotropic, homogenous and simple geometry of the phantom is very different from the brain. Additionally, this model neglects perfusion and low pressure sinks, such as the ventricles and subarachnoid space present in the brain. Additionally, to induce flow, a constant interstitial pressure was prescribed at the infusion cavity boundary. However, during CED, a programmable syringe pump is used to control the flow rate of the infusion. For the flow-controlled case, the interstitial pressure of the

cavity is unknown initially; thus, a constant flow rate cannot be prescribed directly with current FE analysis software. Instead, custom-written FE code or additional steps are required to circumvent the nonlinear boundary condition [173]. Future iterations of this model will include flow-controlled infusions. Given the highlighted limitations, this model was useful for elucidating how factors of CED therapy, such as infusion flow rate and separation distance of individual ports, influence the distribution of an infused solute in a biphasic material. Additionally, it provided a sense of the design constraints when considering the time that would be required for each infusion given a desired spatial distribution of the infusate.

CONCLUSIONS

The infiltrative nature of GBM requires maximizing the dispersion volume of the infused therapeutic to increase the efficacy of CED. Therefore, the drug delivery technology for CED must be optimized in order to make it a viable therapy for GBM. In this study, using multiple ports proved that to be advantageous in increasing the dispersion volume of infused solutes in biphasic material, such as the brain. Increasing the separation distance of individual ports can help increase V_d. However, doubling the separation distance of source ports will require about ten-times longer infusion time for the solute spatial distribution between sources to reach a desired concentration. Increasing the flow rate of the infusion mitigates this effect, although caution is required as higher flow rates result in more reflux. Finally, a compromise of port spacing and flow rate could optimize both infusion duration with max V_d. Such optimization would require clinical guidance and/or adjustment of the treatment parameters based on imaging feedback.

FUTURE WORK

In conventional CED studies, the drug is delivered at a constant flow rate using a programmable syringe pump. Therefore, a constant prescribed infusion pressure may not indicate realistic conditions during CED simulations. However, unlike pressure-driven models, interstitial pressure at the boundary is unknown initially in flow-driven models. Therefore, to account for the nonlinear boundary condition, Smith and Garcia [173, 174] proposed a fixed, artificial boundary consisting of highly permeable and compliant elements, in which a constant radial fluid velocity was prescribed in order to guarantee a constant infusion flow rate.

Another approach to overcome the nonlinear boundary condition is to iteratively solve for the infusion pressure profiles using an optimization algorithm in Matlab along with a FE solver such as FEBio. A target infusion flow rate is prescribed in the optimization algorithm, which then initiates a first guess for the interstitial pressure at the infusion cavity boundary and runs FEBio for the first time step. During each step, part of the fluid volume prescribed will contribute to volume change of the infusion cavity and some would permeate into the tissue across the infusion boundary. This iterative approach is used to find the infusion pressure that will minimize the error between the actual flow rate and the prescribed flow rate at each time step. Therefore, a nonlinear infusion pressure profile can be obtained that guarantees the prescribed constant flow rate.

Creating infusion models with more realistic boundary conditions for CED can elucidate the mechanisms of fluid transport and tissue deformation in the brain during the infusions. Such models could be extremely beneficial in treatment planning for accurate prediction of the fluid distribution with the goal of achieving maximum therapeutic

coverage of the diseased tissue. Additionally, they can predict any potential mechanical damage of the tissue due to the infusion.

Chapter 6: Evaluation of Arborizing Catheter in Excised Porcine Tissue

INTRODUCTION

Chapter 4 demonstrated the greater volume dispersed and mean distribution ratios achieved with the arborizing catheter compared to single-port catheters in brain tissue phantoms [150]. This chapter compares the performance of the refined arborizing catheter versus a single-port catheter in excised porcine brains.

METHODS

Fabrication of Catheters

Two arborizing catheters and two single-port catheters were used for the infusion experiments. A set of each is shown in Figure 6.1A. The refined arborizing catheter prototype used for these experiments consisted of a primary cannula and six total microneedles. The full description of its design and fabrication process is described in Chapter 3. When the microneedles are fully deployed, the step change at the interface of the cannula and microneedles helps stop back flow during the infusion (Figure 6.1B). Similarly, the step change in the single-port catheter is demonstrated in the magnified image.

The single-port catheters were modeled after commercially-available, reflux-preventing step catheters (e.g., SmartFlow cannula, MRI Interventions). The single-port catheter consisted of a single fused-silica capillary tube (i.e. microneedle) fixed inside PEEK tubing (OD 794 μm x ID 381 μm). To create the reflux-preventing step-change, the PEEK-reinforced microneedle was inserted into a PEEK tube (1.5 mm OD). The proximal end of each microneedle was attached to a 22 G plastic dispensing needle with a Luer lock adapter. The distal end of each microneedle was cleaved flat.

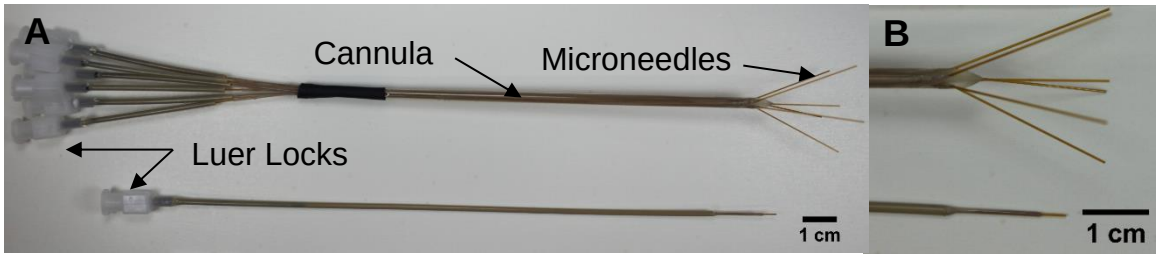

Figure 6.1: A) Image of arborizing catheter and single-port catheter. B) Magnified image of distal ends of the catheters showing microneedle deflection in the arborizing catheter and the reflux-arresting step change for the respective catheters.

Specimen Preparation

Fresh commercial pig heads (n =7) were procured from a local abattoir within hours of harvesting and processed at room temperature. The bulk of the head was removed leaving only a block of tissue encapsulating the cranium and brain (~ 6 cm x 10 cm x 11 cm) to prevent X-ray attenuation during imaging due to excess tissue. A Mopec autopsy saw was used to create a window in the sinus frontalis of the pigs and reveal the underlying frontal bone. Two burr holes were drilled into the cranium, 1.5 cm apart, one on each hemisphere.

Infusion Experiments

A custom-built fixture was used to hold the main cannula of the arborizing catheter and provide support to the microneedles and prevent them from buckling during deployment (Figure 6.3A). The device consists of two plastic plates secured to a linear stage. The back-plate contains vertical channels to help guide the microneedles and the front-plate is used to “sandwich" the catheter and microneedles, securing them to the linear stage. The microneedles were secured to the translating portion of the linear stage with a second fixture used to grip on to their Luer locks (Figure 6.3B). Mountable gage pressure sensors (PX26 series, Omega Engineering, Norwalk CT) were connected to the fluid line for each microneedle and the single-port catheter. Pressure sensors numbered

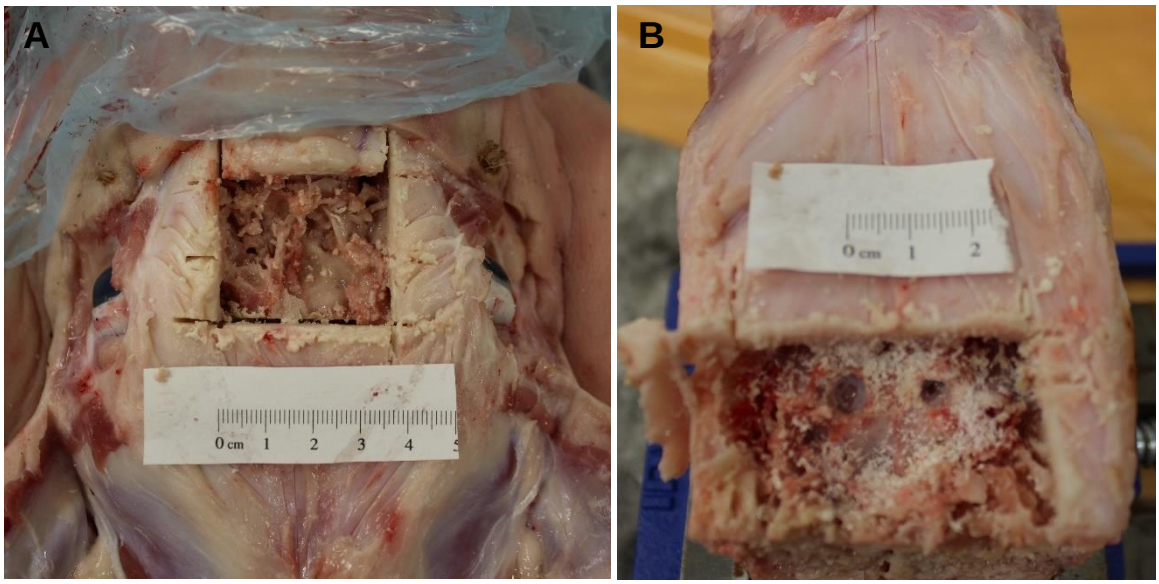

Figure 6.2: A) Window into sinus cavity revealing the underlying frontal bone. B) Block of tissue with excess head tissue removed showing two burr holes created in the porcine cranium. The dura was pierced for access into the brain tissue.

P1-P6 were assigned to each microneedle of the arborizing catheter and a seventh pressure sensor was assigned to the single-port catheter (Figure 6.4). Before the catheters were inserted, the microneedles and fluid lines were primed with the imaging tracer iohexol, at a concentration of 241.2 mg iodine/mL, and fully retracted inside the cannula. The cannula of arborizing catheter and the single port catheter were inserted manually, with the linear stage's micrometer, on the right and left hemispheres of the brain, respectively. The arborizing catheter was inserted approximately 1-cm deep from brain surface. The single port catheter was inserted approximately 2-cm deep from brain surface. Both catheters were inserted at 40° using the flat surface of the tissue specimen as a reference.

A virtual graphical interface program written in LabVIEW (National Instruments, Austin, TX) was used to control a linear actuator (Zaber Technologies, Inc. Vancouver, BC) to simultaneously deploy the microneedles 1-cm deep into brain tissue at an

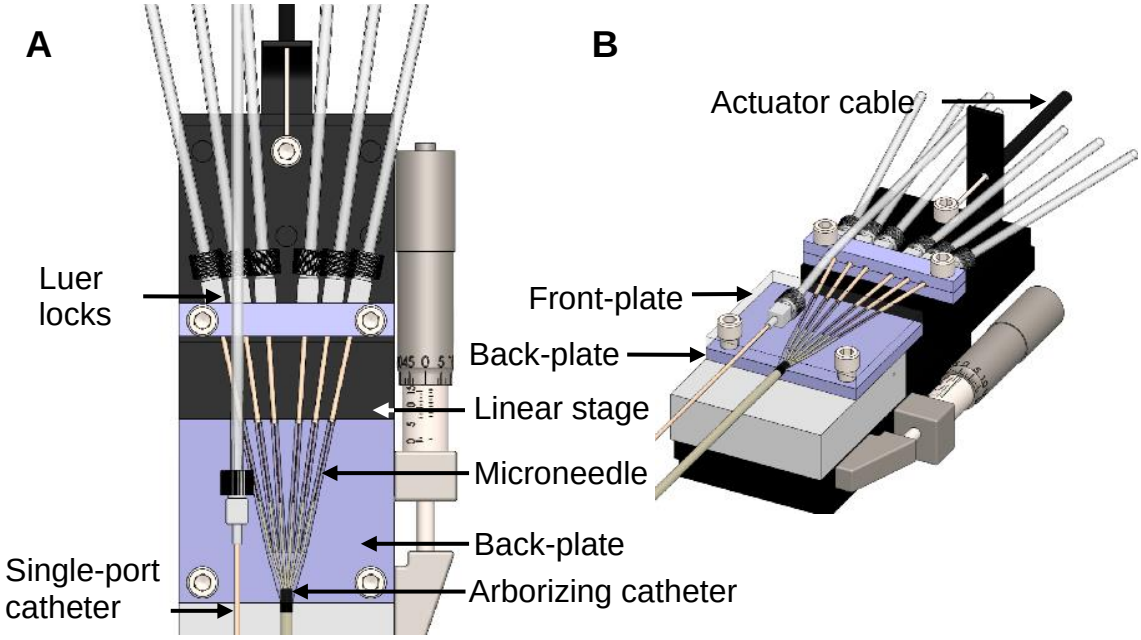

Figure 6.3: A) Diagram of fixture used to secure arborizing catheter and single-port catheter. B) Trimetric view of catheter fixture. The back-plate and frontplate support and guides microneedles.

insertion rate of 0.33 mm/sec. When the microneedles were deployed, the separation distance between adjacent microneedles was approximately 1 cm. The infusion flow rate was set to ramp from 0.5 to 1 µL/min/microneedle for the first 2 minutes, then to a constant flow rate of 1 µL/min/microneedle for the duration of the infusion using a programmable syringe pump (Harvard Apparatus, Holliston, Massachusetts). The total infusion time was 4hrs and 2 min.

Computer Tomography Imaging

Immediately following the infusion, the specimens were transported to the University of Texas at Austin High Resolution X-Ray CT Facility (UTCT) for CT scanning. Each specimen was imaged with the catheters in situ along with iohexol solution standards ranging from 100% to 1% of the stock solution. All specimens were imaged with a North

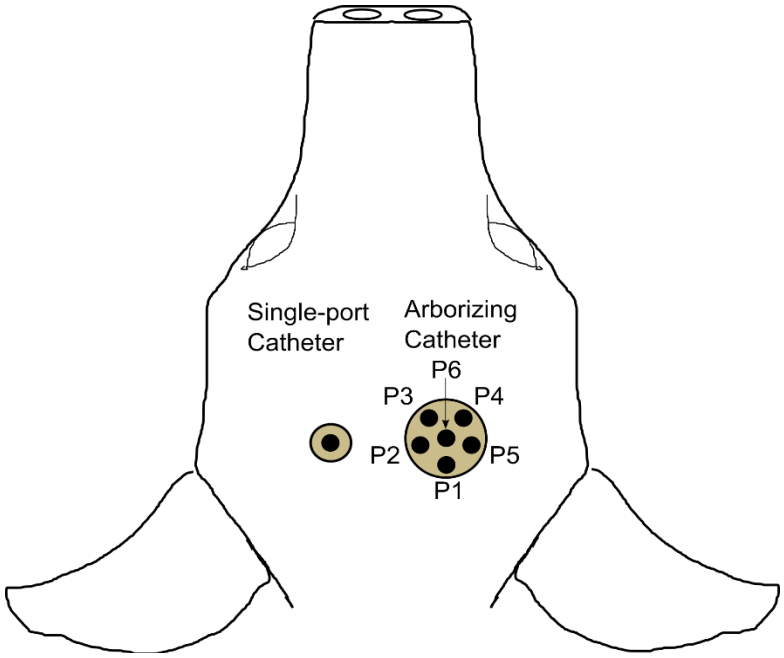

Figure 6.4: Axial view of specimen demonstrating the arrangement of pressure sensors within each catheter. For the arborizing catheter, each dot represents the distal end of the microneedles fully deployed. Illustration not to scale.

Star Imaging CT scanner and Perkin Elmer detector. The specimens were scanned at 130 kV with a current of 0.13 mA. Voxel size was 133.3 μm for all three dimensions. The final data set ranged from 843 to 975 slices.

Image Analysis

For each specimen, stacks of 16-bit TIFF images were imported into Image J (NIH, Bethesda, MD) to extract the corresponding grayscale values from the iohexol solution calibration standards. The intensity value of each standard was averaged from 40-50 images. A concentration of 10% of the iohexol stock solution was selected as the threshold for calculating the volume dispersed (V_d) of the infusion. At this concentration, the mean grayscale intensity for the contrast agent was greater than that of the surrounding brain tissue.

After determining the average grayscale values for the solution standards and brain tissue, the image data was loaded into Avizo (version 9.5 FEI Visualization Sciences Group) for volumetric segmentation. Each voxel size was defined as 133.3 μm based on the CT images. The brain was isolated from the surrounding skull and superfluous tissue. A threshold range using the 10% stock concentration for the lower bound was applied to select the infused contrast agent. This was done in three orthogonal views, leading to a three-dimensional preliminary "mask" containing the selected voxels. This original mask was compartmentalized into separate masks based on each catheter. The infused volume on the right and left hemispheres corresponded to the arborizing catheter and the single-port catheter, respectively. Ventricular leakage was separated from the infusion volumes manually based on the structure of the lateral ventricles visualized in the images. Each catheter's individual contribution to ventricular leakage could not be clearly distinguished, thus leakage was not subdivided, but rather aggregated in a single mask.

The material analysis function available in Avizo was used to count each voxel and calculate the volume of each mask that represented V_d. Given the prescribed flow rate and duration of the infusion, the infused volume (V_i) per microneedle is known a priori, and was used to calculate the mean distribution ratio (V_d:V_i). Using the statistical software R (R Foundation for Statistical Computing, Vienna, Austria), a Student's t-test for two samples was performed to analyze differences in V_d and V_d:V_i for the two catheter groups assuming a significance level equal to 0.05.

RESULTS AND DISCUSSION

Following the infusion of iohexol into excised pig brains, specimens (n=7) and vials of calibration standard solutions were imaged with CT. From CT imaging, it was

observed that in two specimens, one (Specimen A) or two (Specimen B) of the microneedles from the arborizing catheter were not inserted into the brain parenchyma, but rather were placed in epidural space, potentially caused by loss of CSF (Figure 6.5). This was taken into account when calculating V_d:V_i given the smaller total infused volume into the brain parenchyma due to needles not infusing into the tissue.

Before segmentation of the infusion volumes, intensity thresholds were determined. Image stacks of the CT scan were imported into Image J to quantify the grayscale intensity values for the solution dilutions that ranged from 0 to 100% concentration of the iohexol image contrast solution. The grayscale intensity values, averaged from 40-50 images, are plotted versus concentration of iohexol (Figure 6.6). A concentration value of 10% of the stock iohexol solution with a mean intensity value of 20653.7 ± 919.6 was consistently distinct from the surrounding tissue (15880.0 ± 229.0).

The grayscale values derived from the calibration standards were used to set the grayscale threshold in Avizo and select voxels corresponding to 10-100% concentration of infused iohexol (Figure 6.7A). The infusion volume from each hemisphere was further segmented into the single-port and arborizing catheter groups (blue and red, respectively) (Figure 6.7B). The ventricles of the brain acted as “low-pressure-sinks” and flow from the infusion solution leaked into them and was labeled as “leakage” (displayed in green). For the majority of the specimens, the ventricles of the brain were filled with CSF and were indistinguishable from the surrounding tissue with grayscale thresholding. Therefore, the volume infusion from each catheter was separated from the ventricular leakage manually and cutoff where flow tapered into the lateral ventricle (Figure 6.7C). However, because the lateral ventricles are in communication with the third ventricle, it was not feasible to separate the contribution of ventricular leakage from each catheter. All the segmented volumes for all the specimens are shown in Figure 6.8. Arrows

indicate the tips of the microneedles with iohexol drops at end for Specimen A with one microneedles in the epidural space, and Specimen B with two microneedles in the epidural space.

A box plot demonstrating V_d for the three groups: the arborizing catheter, single-port catheter and ventricular leakage, is shown in (Figure 6.9A). The outlier (defined outside the 1.5 times the interquartile range below the lower quartile) in the arborizing catheter group corresponds to Specimen B, with two microneedles inadvertently not inserted into the brain tissue. Mean V_d for the arborizing catheter (2227.4 ± 562.7 mm^3) was significantly higher ($p<0.001$) than the V_d for the single-port catheter (382.2 ± 243.0 mm^3). The flow rate of 1μL/min was prescribed for each microneedle of the arborizing catheter and for the single-port catheter. The selected flow rate is on the low range of flowrates utilized in CED and infusion studies. The arborizing catheter demonstrated that it can achieve high V_d, even at a low flow rate, which may be beneficial given that higher flow rates are associated with reflux [158, 159]. In this study, minimal reflux was observed for both catheters, which was probably due to the step-change incorporated in the catheters and the low flow rate selected.

The design of the arborizing catheter and the goal of this study were to maximize V_d. It was expected that the V_d from the arborizing catheter would be at least 6 times larger than for the single-port catheter given that V_i delivered for the catheter was 6-times greater. The actual difference in the V_d mean for the arborizing catheter was only 5.8-times greater. The two specimens that did not have all six microneedles deployed in the brain parenchyma could explain this slightly lower value. Although consistent methods were employed to position the distal tip of the cannula within the tissue, variability was observed among the surface of the brains after imaging. In some instances there were air pockets between the surface of the brain and skull (i.e. subarachnoid space).

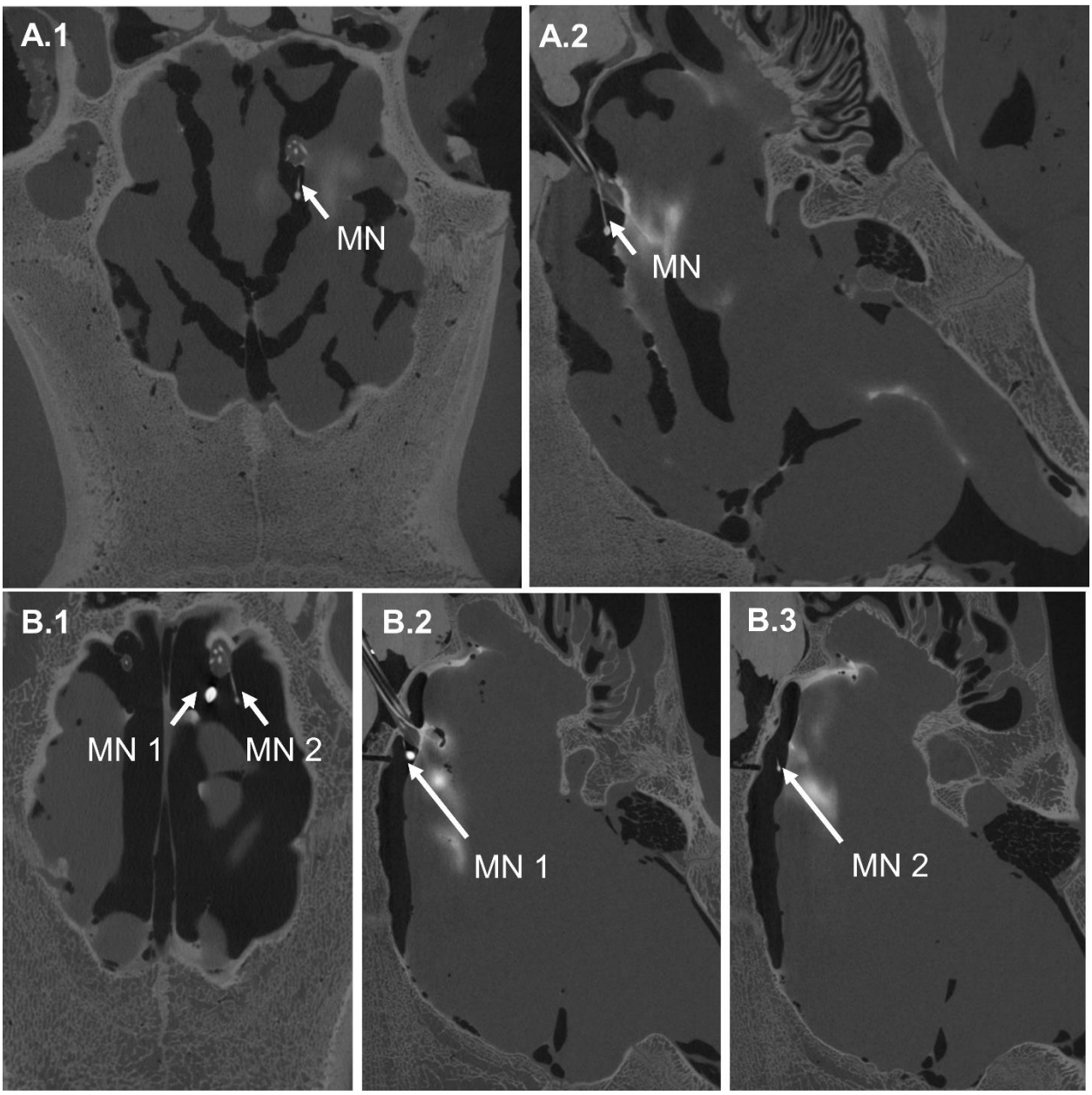

Figure 6.5: A.1) Axial view A.2) and sagittal view of Specimen A with one microneedle (MN) in the epidural space. B.1) Axial view showing Specimen B with two microneedles in the brain. B.2) Sagittal view showing the first microneedle in epidural space. B.3) Sagittal view showing the second microneedle in the epidural space of the brain.

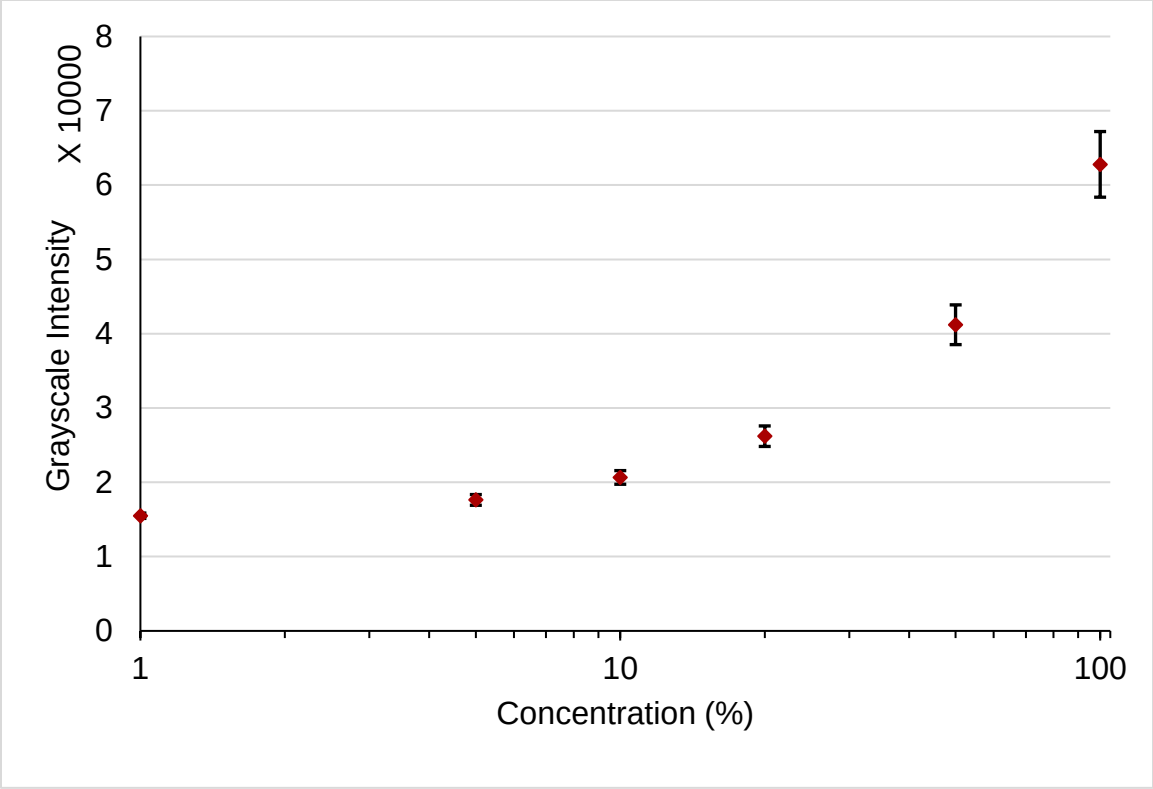

Figure 6.6. Grayscale intensity values versus concentration. A concentration of 10% was selected for the lower bound of grayscale threshold values for selecting voxels of interest.

Loss of perfusion, along with blood and CSF drainage due to the harvesting process, may be responsible for the air pockets. Flow of contrast agent through the subarachnoid space was observed, especially for the specimens with microneedles near the surface of the brain. In specimens with microneedles in the epidural space of brain, the contrast agent was pooled on the surface of the brain. This solution volume was not included as part of the V_d or ventricular leakage.

Given the high recurrence rates of GBM due to frequently infiltrated by GBM cells [32, 148], maximizing V_d is an approach to ensure that the peritumoral regions are treated. This means that local-regional "healthy" tissue would also be treated. This requires the use of targeted therapeutic agents with a wide therapeutic index to obviate

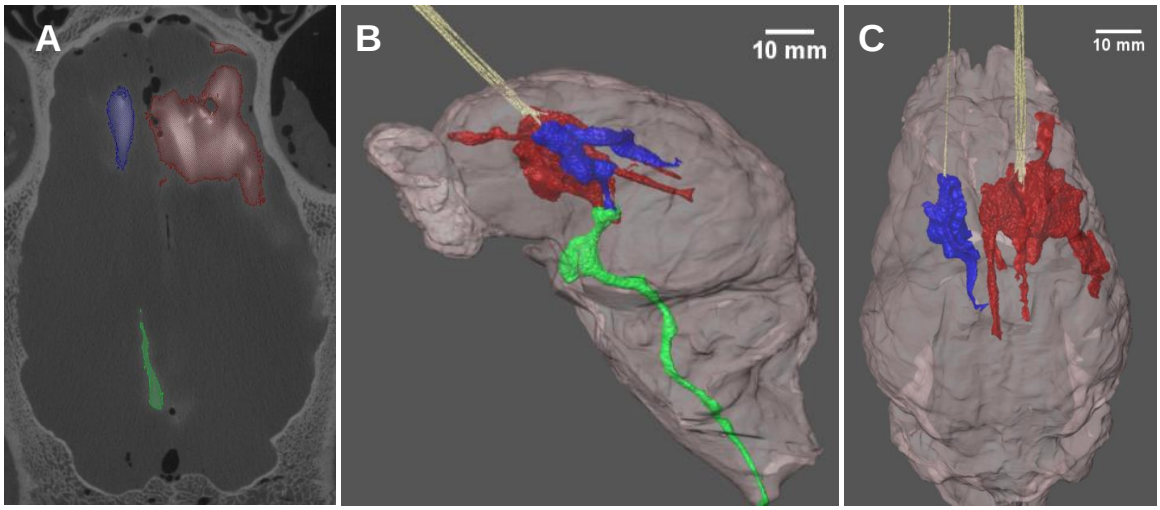

Figure 6.7: Volumetric segmentation with Avizo. A) Voxels with grayscale value corresponding to 10% and greater of iohexol concentration were selected to derive Vd for the single-port catheter (blue) and arborizing catheter (red). The volume of solution that leaked into the ventricles was segmented into a separate mask (green). B) Volumetric rendering of brain and Vd for each group. C) Volumetric rendering showing dispersed volumes for the single port catheter and the arborizing catheter after removing ventricular leakage from image.

peripheral damage of healthy brain tissue when designing for large V_d. The development of such suitable drugs has progressed significantly [188-190, 193].

It is important to note that the V_d for the catheters is a mixture of the iohexol solution and interstitial fluid. Furthermore, ventricular leakage are estimates from the iohexol mixing with the residual CSF after four hours of continuous infusion. Therefore, volumes for all three groups are notably larger than the total infused volume at 100% concentration. Lower leakage values were associated with larger V_d for the arborizing catheter and single-port catheter. A limitation of this study is that the excised brains were an open system and some of the CSF within the ventricles could have flowed out of the brain during the specimen preparation and/or experiments, influencing the end results for leakage. The ventricles were filled with CSF for the majority of the specimens, but the

contrast agent reached the base of the brain, and could have leaked out. However, we only were able to quantify the contrast agent within the ventricles in images.

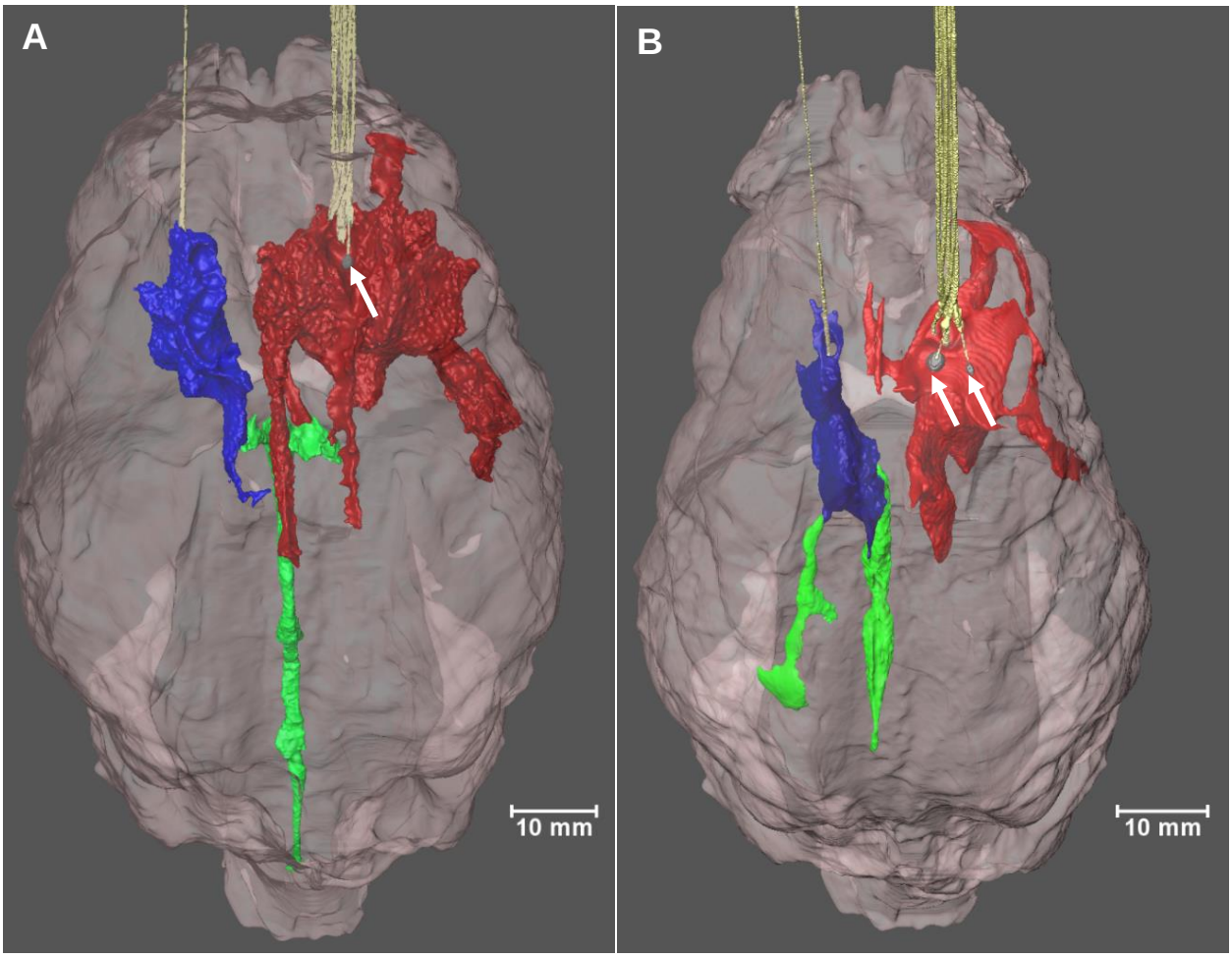

Figure 6.8: Volumetric reconstruction of brain and segmented infusion volumes for the single port catheter (blue) and arborizing catheter (red). Contrast agent that leaked into the ventricles was labeled in green. For Specimen A and Specimen B, one or two microneedles, respectively, were inadvertently placed in the epidural space of the brain and a drop of contrast agent was imaged at the tip of the microneedles. Arrows point to the gray volume that represents the drop of contrast agent at the tip of the microneedles.

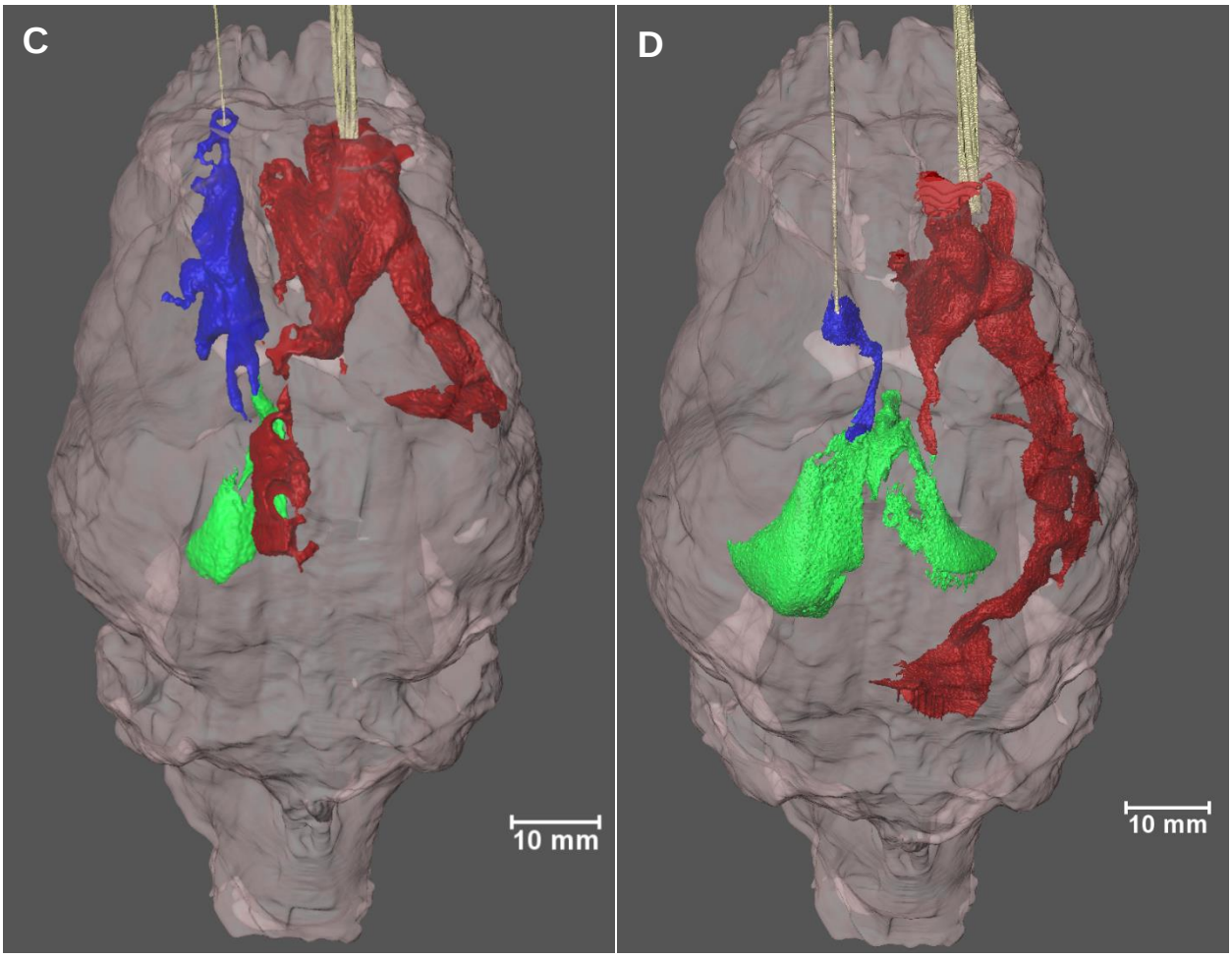

Figure 6.8: cont. Volumetric reconstruction of brain and segmented infusion volumes for the single port catheter (blue) and arborizing catheter (red). Contrast agent that leaked into the ventricles was labeled in green.

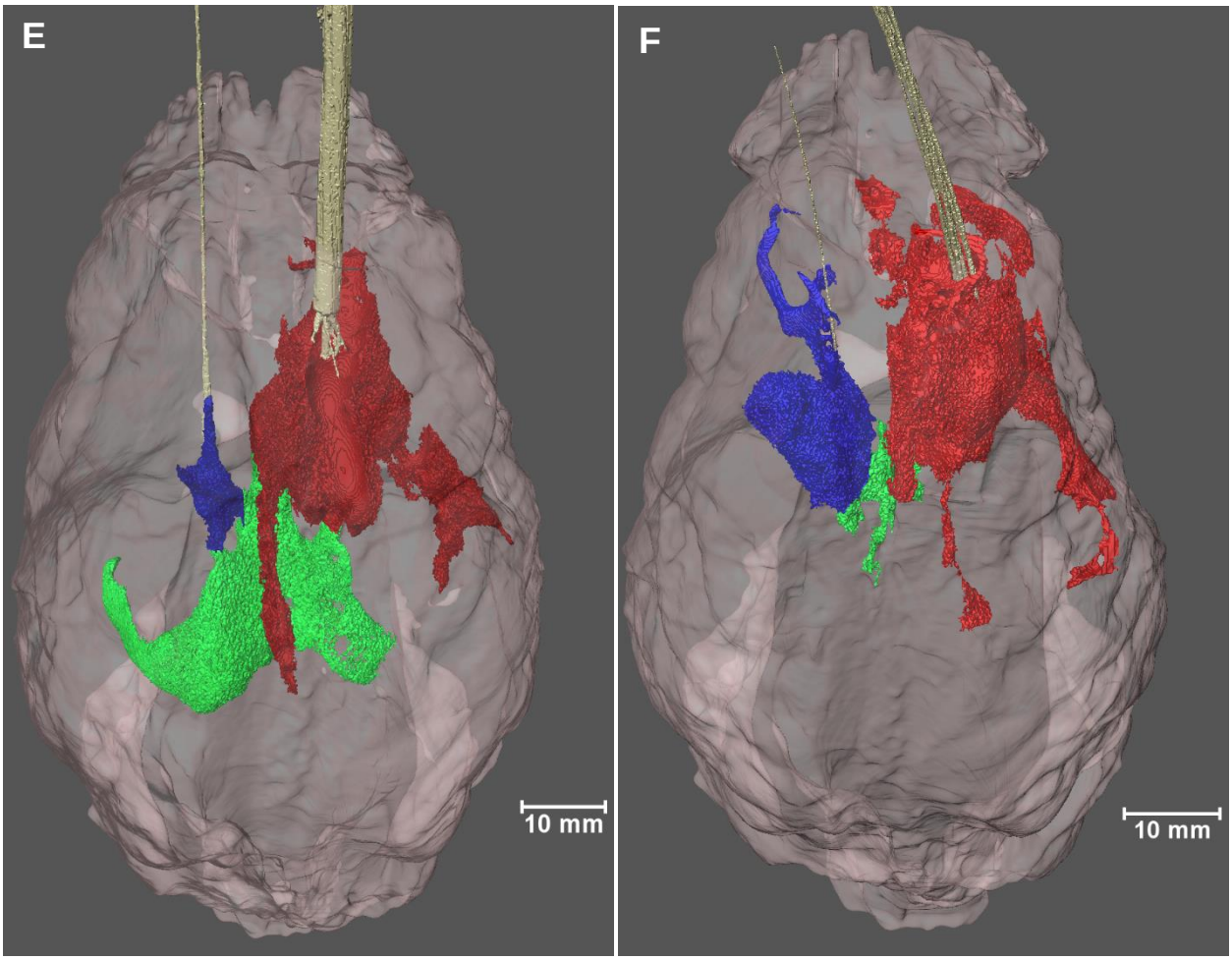

Figure 6.8: cont. Volumetric reconstruction of brain and segmented infusion volumes for the single port catheter (blue) and arborizing catheter (red). Contrast agent that leaked into the ventricles was labeled in green.

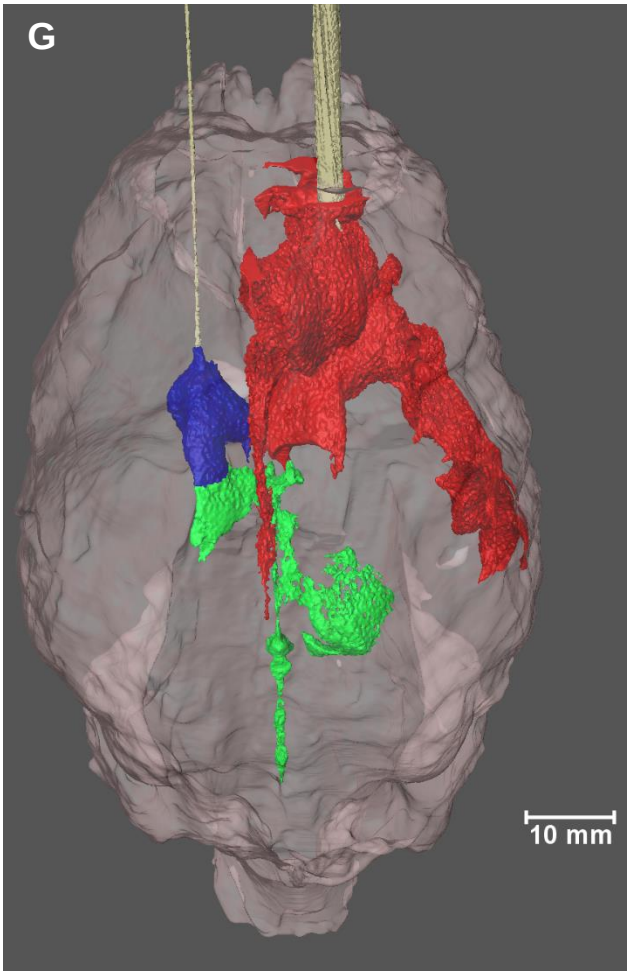

Figure 6.8: cont. Volumetric reconstruction of brain and segmented infusion volumes for the single port catheter (blue) and arborizing catheter (red). Contrast agent that leaked into the ventricles was labeled in green.

Figure 6.9B shows box plot comparing mean distribution ratio for the arborizing catheter and the single-port catheter. Average values of V_d:V_i for the arborizing and the single-port catheters were 1.6 ± 0.3 and 1.6 ± 1.0, respectively. The outliers (defined outside 1.5 times the interquartile range above the upper quartile and below the lower quartile) correspond to the Specimen A (upper outlier) and Specimen B (lower outlier) with microneedles outside of the brain tissue. The loss of infusion volume was accounted for by dividing V_d by lower V_i values when calculating V_d:V_i for these specimens.

Specimen A with only five microneedles actively infusing in the brain resulted in V_d values comparable with V_d values for specimens with all six active microneedles. When dividing by the V_i expected for only five microneedles, its V_d:V_i was higher than the mean V_d:V_i (2.2 vs 1.6). However, this was not the case for the Specimen B with only four active microneedles in brain tissue. A notably smaller V_d (1070 mm^3) was associated with this Specimen B, which in turn, resulted in a small V_d:V_i. The small V_d for this specimen could be due to a compound effect of iohexol not infused in the brain tissue and loss due to leakage into the ventricle. However, that could not be confirmed because of limitations with identifying leakage originating from the arborizing catheter. Another possibility is that in addition to two microneedles not being inserted in the brain, a third microneedle may have been clogged. Pressure data for microneedle labeled P2 in Specimen B saturated and stayed above the sensor's pressure range throughout the infusion. When studying the CT images from for Specimen B, it was observed that minimal, if any, contrast enhancement was shown in the region where the P2 microneedle was inserted in the tissue (Figure 6.10). Thus, a total of 3/6 microneedles may have been inactive. Thus, if only half of the microneedles were active, the resultant V_d of 1070 mm^3 for this Specimen B is expected because it is approximately half of the average V_d quantified for the arborizing group.

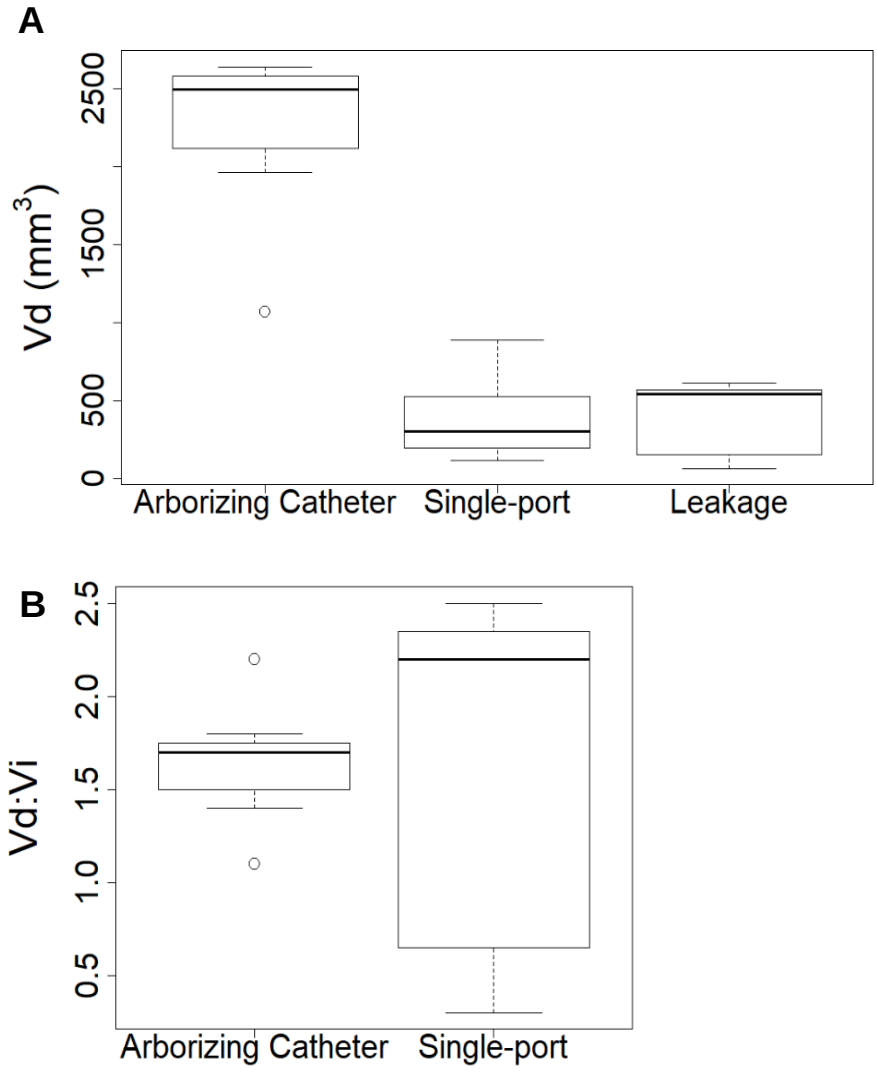

Figure 6.9: A) Box plot demonstrating dispersed volume (V_d) for the arborizing catheter, single-port catheter and any leakage of the contrast agent into the ventricles of the brain. B) Box plot of mean distribution ratio (V_d:V) comparison of the arborizing catheter and the single-port catheter. The outliers correspond to the specimens, which had one or two microneedles or the arborizing catheter outside of the brain tissue.

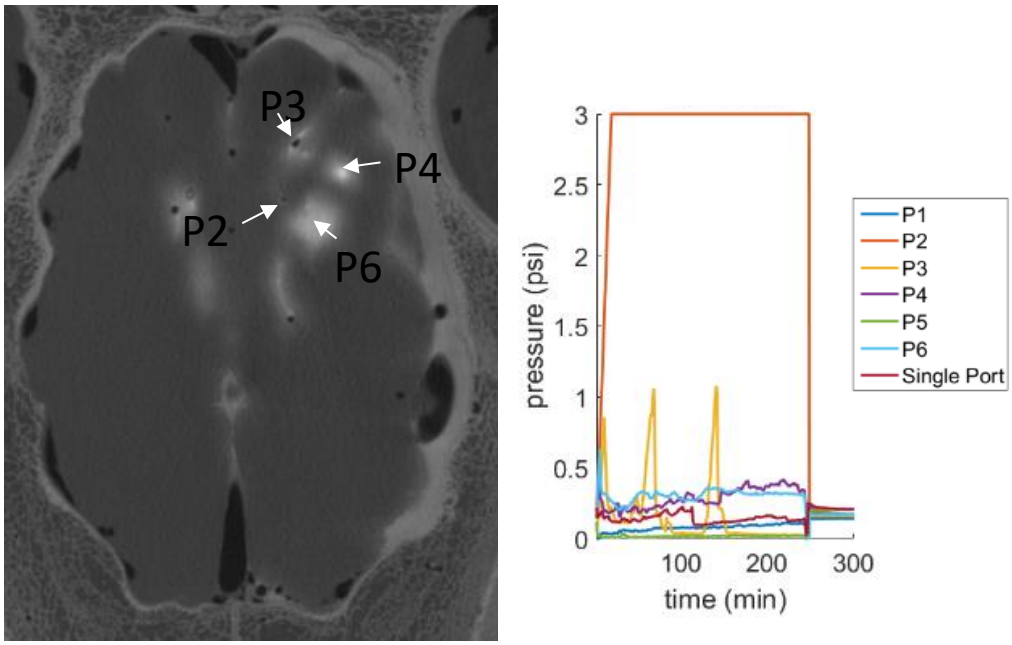

Figure 6.10: Pressure data for P2 (orange) suggest clogging for that microneedle. The lack of contrast in the local region where P2 microneedle was inserted in tissue seem to support this observation.

Overall, the arborizing catheter V_d:V_i were similar compared to the single-port catheter. It is likely that the separation distance of 1 cm between adjacent microneedles, resulted in minimal overlap in the infusion volumes from individual microneedles. Therefore, the arborizing catheter acted like six single-port catheters. Yet, one advantage of the arborizing catheter is that it permits six infusion ports through a single burr hole and trajectory path, which could mitigate the risk of mechanical damage compared to inserting multiple single-port catheters requiring multiple burr holes and trajectory paths. Although the arborizing catheter did not improve V_d:V_i when compared to the single-port catheter, maximizing V_d:V_i may be secondary to maximizing V_d to ensure treatment of infiltrated GBM cells.

Mean distribution ratios in this study were much lower than previous results in infusion experiments using agarose gel and similar flow rates [150, 194]. Mean distribution ratios for the single-port catheter in agarose (at room temperature ~24ºC) were 23.6 ±2.1 and 15.0 ± 1.5 for the arborizing catheter, an order of magnitude larger than for the results in this study (Chapter 4). Several factors could contribute to the discrepancy. First, the complex geometry and heterogeneous structure of the brain led to losses in solution due to ventricular leakage and leakage along the subarachnoid spaces, which stresses the challenge of CED for maximizing drug distribution in the brain. Due to the optically transparent nature of agarose gel, the minimum concentration for infused dyes could be orders of magnitude lower than the 10% minimum iohexol concentration that was needed for grayscale thresholding in CT images. These inherent differences between agarose and brain tissue also highlight the importance of performing infusion studies in brain tissue for the evaluation of the arborizing catheter. Although the specimens were excised tissue, V_d:V_i measured in this study were comparable to values measured in live canines and primate brains [148] and in rat brains [157].

Line pressure data was measured continuously throughout the infusions. For the majority of the microneedles, pressure fluctuated throughout the infusion but remained below 1.5 psi. However, in four instances the pressure increased above 1.5 psi, but never exceeded 12 psi, which could be an indication of rise in pressure due to possible clogging in the microneedles upon insertion into tissue. However, upon removal of the microneedles and inspection, none of the microneedle were permanently clogged, suggesting that clogs, if any, were dislodged upon removal. Because the study was limited to images acquired only at the end of the infusion, it was not possible to definitively correlate the pressure spikes to possible clogging. Therefore, exploration into this issue is required to find a concrete explanation for the higher pressures. One

approach is to intermittently image the infusion in order to investigate the temporal distribution of the contrast agent, especially in the event of pressure spikes. This also illustrates the advantage of having multiple microneedles in which the fluid line can be shut off for individual microneedles in the event of an adverse effect. Alternatively, the microneedle may be individually retracted in an attempt to dislodge clogged tissue.

CONCLUSIONS

The performance of the arborizing catheter versus a step single-port catheter were assessed with infusions of iohexol in excised pig brains. Following the infusions, CT scans of the brains were taken and Avizo was used to analyze the images and quantify V_d of the infused contrast agent. Volume dispersed for the arborizing catheter was significantly higher (5.8 times higher) than the V_d achieved with the single-port catheter. The high V_d values were achieved at a slow flow rate that resulted in minimal reflux for either catheter. Mean distribution ratios for both catheters were not significantly different. The greater V_d achieved with the arborizing catheter is beneficial for maximizing drug coverage of the intended tumor and tumor margin target volume and potentially improving the efficacy of CED.

FUTURE WORK

The arborizing catheter's performance was demonstrated in excised pig brains, however additional evaluation in a live animal model is necessary to access the performance of the catheter in a more challenging environment. Conditions in the live brain including perfusion, interstitial pressure and the challenge of maintaining homeostasis in the animal will add to the difficulty of infusing the brain. To evaluate the capability of the arborizing catheter to deliver therapeutics to GBM, spontaneous canine gliomas can be utilized as translational models of human GBM. Dogs and humans are the

only species in which primary brain tumors are common. Intracranial spontaneous primary tumors in dogs are three times more common than in humans [195, 196] and account for 1-3% of all deaths in aged dogs where necropsy is performed [197]. Dogs with gliomas present significant clinical signs, including seizures, depression or disoriented mental status, and motor dysfunction [198]. Patterns of survival for dogs with GBM (if not euthanized at time of diagnosis) are similar to those seen in humans, with death relatively soon (weeks to months) after diagnosis. Additionally, and unlike implanted tumors in rodents, tumors of the CNS in dogs are large enough to facilitate the testing, optimization, and use of both experimental diagnostic and therapeutic clinical procedures developed for human patients, including CED. Dogs offer a unique pre-clinical model of brain tumors while concurrently serving as patients. The goal of such study, would be to show that the arborizing catheter can broadly saturate tumor and margins with a therapeutic agent co-infused with a imaging contrast agent to quantify volume coverage of the tumor target.

Chapter 7: Conclusions and Future Work

This dissertation provides the most recent and comprehensive review of the arborizing catheter technology. The objective of the arborizing catheter is to address the limited ability of commercial single-port catheters to broadly distribute therapeutics in the brain. The arborizing catheter's design was refined based on user and collaborators' feedback. Then it was evaluated in both agarose and excised pig brains. Additionally, a validated computational model of CED was used to gain insights how interactions between adjacent ports of the arborizing catheter influence solute transport in a biphasic material.

Initial infusion experiments in agarose gels showed that the arborizing catheter could significantly enhance volumetric dispersal of the infusate compare to a single-port catheter. V_d achieved with the arborizing catheter was double the V_d achieved with a single-port for the same total V_i. When comparing infusions at 1µL/min/port, mean distribution ratios for the arborizing catheter were lower than the single-port catheter, suggesting that the distance of adjacent microneedles (< 1 cm) may play a role in the efficiency of the infusion and spread of individual microneedle infusion volumes.

Using a multiphasic finite element framework, the interaction of dispersal volume and separation distance of adjacent microneedles was investigated. Doubling the separation distance of adjacent microneedle could increase dispersal volumes, but drastically increase the time required for distribution at a given concentration threshold. Increasing the flow rate could help mitigate the increase in infusion time, but care should be exercised given the potential for reflux at the higher flow rates. Furthermore, higher flow rates may be less efficient given the reduced hydraulic permeability as a result of local deformation and strain at the infusion site. Thus, the interplay between treatment

time, infusion flow rate and separation of microneedles would need to be considered when treatment planning for desired coverage of the volume target.

Finally, the arborizing catheter was evaluated and compared to a single-port catheter in excised pig brain infusions. Volume dispersed, quantified from contrast-enhanced CT images, for the arborizing catheter was significantly higher (5.8-times higher) than the V_d achieved with the single-port catheter. The flow rate for the infusion was maintained at 1µL/min/port, thus the V_i for the arborizing catheter was 6 times higher. Thus, higher V_d can be achieved at slow flow rates, via one access point to the brain with the arborizing catheter compared to the single-port catheter. Given that slower flow rates are clinically safer and may be associated with less mechanical damage, utilizing slow flow rates, but higher number of ports, may be an advantage in CED.

CONVECTION ENHANCED THERMOTHERAPY CATHETER SYSTEM (CETCS)

The fiberoptic microneedle technology allows for soluble therapeutic agents and laser energy to be simultaneously delivered to tissue. Combining the co-delivery features of light guiding, fiberoptic microneedles and the arborizing catheter yields the concept of Convection-Enhanced Thermo-therapy Catheter System (CETCS). It was previously established, that during CED thermo-therapy, the laser energy heats the target tissue and permits greater volumetric dispersion of the infused agent (up to 80% greater than without co-delivered laser energy) with limited tissue damage [157]. Therefore, the goal of CETCS would be to significantly enhance CED therapy by delivering therapeutics to an extensive volume of the tumor and tumor margins, previously unrealized with standard CED. With broader dispersion of the therapeutic, complete coverage of the tumor and infiltrating cells is more achievable, and can potentially reduce tumor recurrence. Additionally, with enhanced delivery due to the co-delivery arborizing

catheter, coverage of the target tissue may be faster. This is beneficial because it could reduce the duration of the treatment, thus potentially minimizing patient discomfort and time in the operating room resulting in cost-reduction of the procedure.

REAL-TIME MRI FEEDBACK

The PRECISE trial highlighted the limitations associated with "blind" CED. The advantages of monitoring the infusion using a co-infused contrast agent with real-time or quasi-real-time MRI are numerous. First, the neurosurgeon can confirm visually that the therapeutic is covering the intended volume target to treat the diseased tissue. Additionally, in the event of any adverse effects, such as leakage into the ventricles, the neurosurgeon can take action, such as stop the fluid line for that port. Conversely, if the infusion is "well-behaved", the physician can even increase the flow rate, while monitoring the infusion to ensure continuous forward flow.

CETCS combined with real-time imaging feedback would be a fully integrated approach to address the limitations of current CED technology. These developments would enable the first opportunity to treat malignant brain tumors by broadly and accurately delivering drug to the tumor and infiltrative cells through unique features of arborization, photothermal activation, and MRI guidance. Paired with the appropriate targeting cytotoxic therapy, an innovative and versatile treatment system is possible with the goal of achieving better outcomes in patients with MGs.

References

1. *Cancer Facts & Figures 2018*. 2018, American Cancer Society: Atlanta.
2. Johnson, N.B., et al., CDC National Health Report: Leading Causes of Morbidity and Mortality and Associated Behavioral Risk and Protective Factors—United States, 2005–2013. *CDC MMWR*. 2014; **63**(4): 1-27.
3. *SEER Cancer Statistics Review*, N. AM, et al., Editors. 1975-2015, National Cancer Institute: Bethesda, MD.
4. Wen, P.Y. and S. Kesary, Malignant Gliomas in Adults. *The New England Journal of Medicine*. 2008; **359**(5): 492-507.
5. Ostrom, Q.T., et al., CBTRUS Statistical Report: Primary Brain and Other Central Nervous System Tumors Diagnosed in the United States in 2009-2013. *Neuro Oncol*. 2016; **18**(suppl_5): v1-v75.
6. Berger, M.S., Malignant astrocytomas: surgical aspects. *Semin Oncol*. 1994; **21**(2): 172-185.
7. Lesser, G.J. and S. Grossman, The chemotherapy of high-grade astrocytomas. *Semin Oncol*. 1994; **21**(2): 220-235.
8. Shaw, E.J., Central Nervous System Overview, in L.L. Gunderson and J.E. Tepper, Editors. *Clinical Radiation Oncology*. Churchill-Livingstone: Philadelphia, PA; 2000: 314-354.
9. DeAngelis, L.M., Brain Tumors. *N Engl J Med*. 2001; **344**(2): 114-123.
10. Ahmed, R., et al., Malignant gliomas: current perspectives in diagnosis, treatment, and early response assessment using advanced quantitative imaging methods. *Cancer Manag Res*. 2014; **6**: 149-170.
11. Rao, J.S., Molecular mechanisms of glioma invasiveness: the role of proteases. *Nat Rev Cancer*. 2003; **3**(7): 489-501.
12. Pollak, L., et al., Meningiomas after radiotherapy for tinea capitis--still no history. *Tumori*. 1998; **84**(1): 65-68
13. Fisher, J.L., et al., Epidemiology of brain tumors. *Neurol Clin*. 2007; **25**(4): 867-890, vii.
14. Walter, A.W., et al., Secondary Brain Tumors in Children Treated for Acute Lymphoblastic Leukemia at St Jude Children's Research Hospital. *J Clin Oncol*. 1998; **16**(12): 3761-3767.
15. C, F., et al., Current Standards of Care in Glioblastoma Therapy, in D.V. S, Editor. *Glioblastoma*. Codon Publications: Brisbane (AU); 2017: 197-241.
16. Walbert, T. and A. Pace, End-of-life care in patients with primary malignant brain tumors: early is better. *Neuro Oncol*. 2016; **18**(1): 7-8.

17. Arber, A., et al., A study of patients with a primary malignant brain tumour and their carers: symptoms and access to services. *Int J Palliat Nurs*. 2010; **16**(1): 24-30.

18. Lefranc, F., J. Brotchi, and R. Kiss, Possible future issues in the treatment of glioblastomas: special emphasis on cell migration and the resistance of migrating glioblastoma cells to apoptosis. *J Clin Oncol*. 2005; **23**(10): 2411-2422.

19. Demuth, T. and M.E. Berens, Molecular mechanisms of glioma cell migration and invasion. *J Neurooncol*. 2004; **70**(2): 217-228.

20. Nishikawa, R., Standard Therapy for Glioblastoma - A Review of Where We Are. *Neurol Med Chir (Tokyo)*. 2010; **50**: 713-719.

21. Lacroix, M., et al., A multivariate analysis of 416 patients with glioblastoma multiforme: prognosis, extent of resection, and survival. *J Neurosurg*. 2001; **95**: 190-198.

22. Jeremic, B., et al., Multivariate analysis of clinical prognostic factors in patients with glioblastoma multiforme treated with a combined modality approach. *J Cancer Res Clin Oncol*. 2003; **129**(8): 477-484.

23. Lutterbach, J., W. Sauerbrei, and R. Guttenberger, Multivariate analysis of prognostic factors in patients with glioblastoma. *Strahlenther Onkol*. 2003; **179**(1): 8-15.

24. Simpson, J.R., et al., Influence of location and extent of surgical resection on survival of patients with glioblastoma multiforme: results of three consecutive radiation therapy oncology group (RTOG) Clinical Trials. *Int J Radiat Oncol Biol Phys*. 1993; **26**: 239-244.

25. Sawaya, R., Extend of resection in malignant gliomas: a critical summary. *J Neurooncol*. 1999; **42**: 303-305.

26. Keles, G.E., B. Anderson, and M.S. Berger, The Effect of Extent of Resection on Time to Tumor Progression and Survival in Patients with Glioblastoma Multiforme of the Cerebral Hemisphere. *Surg Neurol*. 1999; **52**: 371-379.

27. Keles, G.E., et al., Volumetric extent of resection and residual contrast enhancement on initial surgery as predictors of outcome in adult patients with hemispheric anaplastic astrocytoma. *J Neurosurg*. 2006; **105**: 34-40.

28. Ammirati, M., et al., Effect of the Extend of Surgical Resection on Survival and Quality of Life in Patients with Supratentorial Glioblastomas and Anaplastic Astrocytomas. *Neurosurgery*. 1987; **21**(2): 201-206.

29. Hervey-Jumper, S.L., et al., Awake craniotomy to maximize glioma resection: methods and technical nuances over a 27-year period. *J Neurosurg*. 2015; **123**(2): 325-339.

30. Walker, M.D., et al., Evaluation of BCNU and/or radiotherapy in the treatment of anaplastic gliomas. *J Neurosug*. 1978; **49**: 333-343.

31. Caldwell, W.L. and S.A. Aristizabal, Treatment of Glioblastoma Multiforme A Review. *Acta Radiologica: Therapy, Physics, Biology*. 2009; **14**(6): 505-512.

32. Hochberg, F.H. and A. Pruitt, Assumptions in the radiotherapy of glioblastoma. *Neurology*. 1980; **30**(9): 907-911.

33. Wallner, K.E., et al., Patterns of failure following treatment of glioblastoma mulitform and anaplastic astrocytoma. *Int J Radiat Oncol Biol Phys*. 1989; **16**: 1405-1409.

34. Stupp, R., et al., Radiotherapy plus concomitant and adjuvant temozolomide for glioblastoma. *N Engl J Med*. 2005; **352**(10): 987-996.

35. Stewart, L., Chemotherapy in adult high-grade glioma: a systematic review and meta-analysis of individual patient data from 12 randomised trials. *The Lancet*. 2002; **359**(9311): 1011-1018.

36. Fine, H.A., et al., Meta-Analysis of Radiation Therapy with and without Adjuvant Chemotherapy for Malignant Gliomas in Adults. *Cancer*. **71**(8): 2585-2595.

37. Agarwala, S.S. and J.M. Kirkwood, Temozolomide, a Novel Alkylating Agent with Activity in the Central Nervous System, May Improve the Treatment of Advanced Metastatic Melanoma. *The Oncologist*. 2000; **5**: 144-151.

38. Hegi, M.E., et al., MGMT Gene Silencing and Benefit from Temozolomide in Glioblastoma. *N Engl J Med*. 2005; **352**: 997-1003.

39. Esteller, M., et al., Inactivation Of The DNA-Repair Gene Mgmt And The Clinical Response Of Gliomas To Alkylating Agents. *N Engl J Med*. 2000; **343**(19): 1350-1354.

40. Westphal, M., et al., A phase 3 trial of local chemotherapy with biodegradable carmustine (BCNU) wafers (Gliadel wafers) in patients with primary malignant glioma. *Neuro Oncol*. 2003; **April**: 79-88.

41. Westphal, M., et al., Gliadel wafer in initial surgery for malignant glioma: long-term follow-up of a multicenter controlled trial. *Acta Neurochir (Wien)*. 2006; **148**(3): 269-275; discussion 275.

42. Stupp, R., et al., NovoTTF-100A versus physician's choice chemotherapy in recurrent glioblastoma: a randomised phase III trial of a novel treatment modality. *Eur J Cancer*. 2012; **48**(14): 2192-2202.

43. Stupp, R., et al., Maintenance Therapy With Tumor-Treating Fields Plus Temozolomide vs Temozolomide Alone for Glioblastoma: A Randomized Clinical Trial. *JAMA*. 2015; **314**(23): 2535-2543.

44. Rick, J., A. Chandra, and M.K. Aghi, Tumor treating fields: a new approach to glioblastoma therapy. *J Neurooncol*. 2018; **137**(3): 447-453.

45. Chen, L., et al., Glioblastoma recurrence patterns near neural stem cell regions. *Radiother Oncol*. 2015; **116**(2): 294-300.

46. Mallick, S., et al., Management of glioblastoma after recurrence: A changing paradigm. *J Egypt Natl Canc Inst*. 2016; **28**(4): 199-210.

47. Wong, E.T., et al., Outcomes and Prognostic Factors in Recurrent Glioma Patients Enrolled Onto Phase II Clinical Trials. *Journal of Clinical Oncology*. 1999; **17**(8): 2572-2578.

48. Yung, W.K.A., et al., Multicenter Phase II Trial of Temozolomide in Patients With Anaplastic Astrocytoma or Anaplastic Oligoastrocytoma at First Relapse. *J Clin Oncol*. 1999; **17**: 2762-2771.

49. Yung, W.K.A., et al., A phase II study of temozolomide vs. procarbazine in patients with glioblastoma multiforme at first relapse. *British Journal of Cancer*. 2000; **83**(5): 588-593.

50. Scott, J.N., et al., Which Glioblastoma Mutlfiforme Patient will Become a Long-term Survivor? A Population-based Study. *Ann Neurol*. 1999; **46**: 183-188.

51. Gavrilovic, I.T. and J.B. Posner, Brain metastases: epidemiology and pathophysiology. *J Neurooncol*. 2005; **75**(1): 5-14.

52. Nayak, L., E.Q. Lee, and P.Y. Wen, Epidemiology of brain metastases. *Curr Oncol Rep*. 2012; **14**(1): 48-54.

53. Nussbaum, E.S., et al., Brain Metastases: Histology, Multiplicity, Surgery, and Survival. *Cancer*. 1996; **78**(8): 1781-1787.

54. Hung, J.J., et al., Prognostic factors of postrecurrence survival in completely resected stage I non-small cell lung cancer with distant metastasis. *Thorax*. 2010; **65**(3): 241-245.

55. Chen, A.M., et al., Risk of cerebral metastases and neurological death after pathological complete response to neoadjuvant therapy for locally advanced nonsmall-cell lung cancer: clinical implications for the subsequent management of the brain. *Cancer*. 2007; **109**(8): 1668-1675.

56. Stemmler, H.J., et al., Characteristics of patients with brain metastases receiving trastuzumab for HER2 overexpressing metastatic breast cancer. *Breast*. 2006; **15**(2): 219-225.

57. Clayton, A.J., et al., Incidence of cerebral metastases in patients treated with trastuzumab for metastatic breast cancer. *Br J Cancer*. 2004; **91**(4): 639-643.

58. Shonka, N.A., et al. *Primary and Metastatic Brain Tumors*. Cancer Management 2015; Available from: http://www.cancernetwork.com/cancer-management/primary-and-metastatic-brain-tumors.

59. Delattre, J., et al., Distribution of brain metastases. *Archives of Neurology*. 1988; **45**(7): 741-744.

60. Shonka, N.A., et al., *Primary and Metastatic Brain Tumors*. 2015, Cancer Management.

61. Noordijk, E.M., et al., The choice of treatment of single brain metastasis should be based on extracranial tumor activity and age. *Int J Radiat Oncol Biol Phys*. 1994; **29**(4): 711-717.

62. Bindal, R.K., et al., Surgical treatment of multiple brain metastases. *J Neurosurg*. 1993; **79**: 210-216.

63. van den Bent, M.J., The role of chemotherapy in brain metastases. *European Journal of Cancer*. 2003; **39**(15): 2114-2120.

64. Chen, G., et al., Chemotherapy for brain metastases in small-cell lung cancer. *Clin Lung Cancer*. 2008; **9**(1): 35-38.

65. Peereboom, D.M., Chemotherapy in Brain Metastases. *Neurosurgery*. 2005; **57**(Supplement): S4-54-S4-65.

66. Patel, M.M., et al., Getting into the brain: approaches to enhance brain drug delivery. *CNS Drugs*. 2009 **23**(1): 35-58.

67. Pardridge, W.M., The Blood-Brain Barrier: Bottleneck in Brain Drug Development. *J American Society for Experimental NeuroTherapeutics*. 2005; **2**: 3-14.

68. Liebner, S., C.J. Czupalla, and H. Wolburg, Current concepts of blood-brain barrier development. *Int J Dev Biol*. 2011; **55**(4-5): 467-476.

69. Figley, C.R. and P.W. Stroman, The role(s) of astrocytes and astrocyte activity in neurometabolism, neurovascular coupling, and the production of functional neuroimaging signals. *Eur J Neurosci*. 2011; **33**(4): 577-588.

70. Chose, A.K., V.N. Viswanadhan, and J.J. Wendoloski, A Knowledge-Based Approach in Designing Combinatorial or Medicinal Chemistry Libraries for Drug Discovery. 1. A Qualitative and Quantitative Characterization of Known Drug Databases. *J Comb Chem*. 1999; **1**: 55-68.

71. Regina, A., et al., Multidrug resistance in brain tumors: Roles of the blood-brain barrier. *Cancer and Metastasis Reviews*. 2001; **20**: 13-25.

72. van Tellingen, O., et al., Overcoming the blood-brain tumor barrier for effective glioblastoma treatment. *Drug Resist Updat*. 2015; **19**: 1-12.

73. Liu, Y. and W. Lu, Recent advances in brain tumor-targeted nano-drug delivery systems. *Expert Opinion on Drug Delivery*. 2012; **9**(6): 671-686.

74. Groothuis, D.R., The blood-brain and blood-tumor barriers: A review of strategies for increasing drug delivery. *Neuro Oncol*. 2000: 45-59.

75. Liebner, S., et al., Claudin-1 and claudin-5 expression and tight junction morphology are altered in blood vessels of human glioblastoma multiforme. *Acta Neuropathol*. 2000; **100**: 323-331.

76. Lu, V.M., K.L. McDonald, and H.E. Townley, Realizing the therapeutic potential of earth element in designing nanoparticles to target and treat glioblastoma. *Nanomed*. 2017; **12**(19): 2389-2401.

77. Hobbs, S.K., et al., Regulation of transport pathways in tumor vessels: Role of tumor type and microenvironment. *Proc Natl Acad Sci USA*. 1998; **95**: 4607-4612.

78. Zhan, C. and W. Lu, The Blood-Brain/Tumor Barriers: Challenges and Chances for Malignant Gliomas Targeted Drug Delivery. *Current Pharmaceutical Biotechnology*. 2012; **13**(12): 2380-2387.

79. Kreuter, J., et al., Passage of peptides through the blood-brain barrier with colloidal polymer particles (nanoparticles). *Brain Research*. 1994; **674**: 171-174.

80. Azad, T.D., et al., Therapeutic strategies to improve drug delivery across the blood-brain barrier. *Neurosurg Focus*. 2015; **38**(3): E9.

81. Pardridge, W.M., Drug transport across the blood-brain barrier. *J Cereb Blood Flow Metab*. 2012; **32**(11): 1959-1972.

82. Kreuter, J., Nanoparticulate systems for brain delivery of drugs. *Advanced Drug Delivery Reviews*. 2001; **47**: 65-81.

83. Chen, Y. and L. Liu, Modern methods for delivery of drugs across the blood-brain barrier. *Adv Drug Deliv Rev*. 2012; **64**(7): 640-665.

84. Orive, G., et al., Biomaterial-based technologies for brain anti-cancer therapeutics and imaging. *Biochim Biophys Acta*. 2010; **1806**(1): 96-107.

85. Kunwar, S., et al., Phase III randomized trial of CED of IL13-PE38QQR vs Gliadel wafers for recurrent glioblastoma. *Neuro Oncol*. 2010; **12**(8): 871-881.

86. Vogelbaum, M.A. and M.K. Aghi, Convection-enhanced delivery for the treatment of glioblastoma. *Neuro Oncol*. 2015; **17 Suppl 2**: ii3-ii8.

87. Szvalb, A.D., et al., Ommaya reservoir-related infections: clinical manifestations and treatment outcomes. *J Infect*. 2014; **68**(3): 216-224.

88. De Bonis, P., et al., Safety and efficacy of Gliadel wafers for newly diagnosed and recurrent glioblastoma. *Acta Neurochir (Wien)*. 2012; **154**(8): 1371-1378.

89. Kemper, E.M., et al., Modulation of the blood-brain barrier in oncology: therapeutic opportunities for the treatment of brain tumours? *Cancer Treat Rev*. 2004; **30**(5): 415-423.

90. Goldwirt, L., et al., Enhanced brain distribution of carboplatin in a primate model after blood-brain barrier disruption using an implantable ultrasound device. *Cancer Chemother Pharmacol*. 2016; **77**(1): 211-216.

91. Choi, J.J., et al., Molecules of various pharmacologically-relevant sizes can cross the ultrasound-induced blood-brain barrier opening in vivo. *Ultrasound Med Biol*. 2010; **36**(1): 58-67.

92. Kovacs, Z.I., et al., Disrupting the blood-brain barrier by focused ultrasound induces sterile inflammation. *Proc Natl Acad Sci U S A*. 2017; **114**(1): E75-E84.

93. Hjouj, M., et al., MRI study on reversible and irreversible electroporation induced blood brain barrier disruption. *PLoS One*. 2012; **7**(8): e42817.

94. Lorenzo, M., C. Arena, and R.V. Davalos, Maximizing Local Access to Therapeutic Deliveries in Glioblatoma. Part III: Irreversible Electroporation for the Eradication of Glioblastoma, in D.V. S, Editor. *Glioblastoma*. Codon Publications: Brisbane, Australia; 2017.

95. Bobo, R.H., et al., Convection-enhanced delivery of macromolecules in the brain. *Proceedings of the National Academy of Sciences of the United States of America*. 1994; **91**: 2076-2080.

96. Morrison, P.F., et al., High-flow microinfusion: tissue penetration and pharmacodynamics. *Am J Physiol*. 1994; **266**(1 Pt 2): R292-305.

97. Bosch, D.A., et al., Intraneoplastic administration of bleomycin in intracerebral gliomas: a pilot study, in F. Gillingham, et al., Editors. *Advances in Stereotactic and Functional Neurosurgery 4. Acta Neurochirurgica Supplementum*. Springer: Vienna; 1980: 441-444.

98. Lieberman, D.M., et al., Convection-enhanced distribution of large molecules in gray matter during interstitial drug infusion. *J Neurosug*. 1995; **82**: 1021-1029.

99. Vandergrift, W.A., et al., Convection-enhanced delivery of immunotoxins and radioisotopes for treatment of malignant gliomas. *Neurosurg Focus*. 2006; **20**(4): E13.

100. Ferguson, S. and M.S. Lesniak, Convection Enhanced Drug Deliver of Novel Therapeutic Agents to Malignant Brain Tumors. *Curr Drug Deliv*. 2007; **4**: 169-180.

101. Degen, J.W., et al., Safety and efficacy of convection-enhanced delivery of gemcitabine or carboplatin in a malignant glioma model in rats. *J Neurosurg*. 2003; **99**(5): 893-898.

102. Kunwar, S., Convection enhanced delivery of IL13-PE38QQR for treatment of recurrent malignant glioma: presentation of interim findings from ongoing phase I studies. *Acta Neurochir Suppl.* . 2003; **88**: 105-111.

103. Laske, D.W., R.J. Youle, and E.H. Oldfield, Tumor regression with regional distribution of the targeted toxin TF-CRM107 in patients with malignant brain tumors. *Nat Med*. 1997; **3**: 1362-1368.

104. Lieberman, D.M., et al., Convection-enhanced distribution of large molecules in gray matter during interstitial drug infusion. *J Neurosurg*. 1995; **82**: 1021-1029.

105. Bidros, D. and M.A. Vogelbaum, Barriers to delivery of therapeutics to brain tumors, in R.H. Winn, Editor. *Youman's Neruological Surgery*. Elsevier Saunders: Philadelphia; 2011: 1172-1117.

106. Lonser, R.R., et al., Successful and safe perfusion of the primate brainstem: in vivo magnetic resonance imaging of macromolecular distribution during infusion. *J Neurosurg*. 2002; **97**(4): 905-913.

107. Gill, S.S., et al., Direct brain infusion of glial cell line-derived neurotrophic factor in Parkinson disease. *Nat Med*. 2003; **9**(5): 589-595.

108. Slevin, J.T., et al., Improvement of bilaterial motor functions in patients with Parkinson disease through the uniteral intraputaminal infsion of glial cell line-derived neurotrophic factor. *J Neurosug*. 2005; **102**: 216-222.

109. Rogawski, M.A., Convection-enhanced delivery in the treatment of epilepsy. *Neurotherapeutics*. 2009; **6**(2): 344-351.

110. Barua, N.U., et al., Convection-Enhanced Delivery of Neprilysin: A Novel Amyloid-β-Degrading Therapeutic Strategy. *J Alzheimers Dis*. 2012; **32**(1): 43-56.

111. Miners, J.S., et al., AB-Degrading Enzymes: Potential for Treatment of Alzheimer Disease. *J Neuropathol Exp Neurol*. 2011; **70**(11): 944-959.

112. Sampson, J.H., et al., Intracerebral infusate distribution by convection-enhanced delivery in humans with malignant gliomas: Descriptive effects of target anatomy and catheter positioning. *Neurosurgery*. 2007; **90**(2): 89–99.

113. Debinski, W. and S.B. Tatter, Convection-enhanced delivery for the treatment of brain tumors. *Expert Rev Neurother.* 2009; **9**(10): 1519-1527.

114. Lidar, Z., et al., Convection-enhanced delivery of paclitaxel for the treatment of recurrent malignant glioma: A Phase I/II clinical study. *Journal of Neurosurgery*. 2004; **100**(3): 472-479.

115. Yang, W., et al., Convection enhanced delivery of carboplatin in combination with radiotherapy for the treatment of brain tumors. *J Neurooncol*. 2011; **101**(3): 379-390.

116. Patchell, R.A., et al., A phase I trial of continuously infused intratumoral bleomycin for the treatment of recurrent glioblastoma multiforme. *J Neurooncol*. 2002; **60**(1): 37-42.

117. Patel, S.J., et al., Safety and Feasibility of Convection-enhanced Delivery of Cotara for the Treatment of Malignant Glioma: Initial Experience in 51 Patients. *Neurosurgery*. 2005; **56**(6): 1243-1253.

118. Rand, R.W., et al., Intratumoral Administration of Recombinant Circularly Permuted Interleukin-4-Pseudonomas Exotoxin in Patients with High-Grade Glioma. *Clin Cancer Res*. 2000; **6**: 2157-2165.

119. Sampson, J.H., et al., Progress report of a Phase I study of the intracerebral microinfusion of a recombinant chimeric protein composed of transforming growth factor (TGF)-α and a mutated form of the Pseudomonas exotoxin termed PE-38 (TP-38) for the treatment of malignant brain tumors. *J Neurooncol*. 2003; **65**(1): 27-35.

120. Bruce, J.N., et al., Intracerebral Clysis in a Rat Glioma Model. *Neurosurgery*. 2000; **46**(3): 683-691.

121. Kaiser, M.G., et al., Tissue Distribution and Antitumor Activity of Topotecan Delivered by Intracerebral Clysis in a Rat Glioma Model. *Neurosurgery*. 2000; **47**(6): 1391-1399.

122. Bruce, J.N., et al., Regression of recurrent malignant gliomas with convection-enhanced delivery of topotecan. *Neurosurgery*. 2011; **69**(6): 1272-9; discussion 1279-1280.

123. Voges, J., R. Reszka, and A. Gossman, Image-guided convection-enhanced delivery and gen therapy of glioblastoma. *Ann Neurol*. 2003; **54**(4): 479-487.

124. Barua, N.U., et al., Convection-enhanced delivery of AAV2 in white matter--a novel method for gene delivery to cerebral cortex. *J Neurosci Methods*. 2013; **220**(1): 1-8.

125. Bernal, G.M., M.J. LaRiviere, and N. Mansour, Convection-enhanced delivery and in vivo imaging of polymeric nanoparticles for the treatment of malignant glioma. *Nanomed*. 2014; **10**(1): 149-157.

126. Debinski, W., et al., Human Glioma Cells Overexpress Receptors for Interleukin 13 and are Extremely Sensitive to a Novel Chimeric Protein Composed of Interleukin 13 and *Pseudonomas* Exotoxin. *Clin Cancer Res*. 1995; **1**: 1253-1258.

127. Debinski, W., et al., Receptor for Interleukin 13 Is a Marker and Therapeutic Target for Human High-Grade Gliomas. *Clin Cancer Res*. 1999; **5**: 985-990.

128. Debinski, W., N.I. Obiri, and R. Puri, A Novel Chimeric Protien Composed of Interleukin 13 and Pseudomonas Exotoxin is Highly Cytotoxic to Human

Carcinoma Cells Expressing Receptors for Interleukin 13 and Interleukin 4. *J Biol Chem*. 1995; **270**(28): 16775-16780.

129. Kunwar, S., et al., Direct intracerebral delivery of cintredekin besudotox (IL13-PE38QQR) in recurrent malignant glioma: a report by the Cintredekin Besudotox Intraparenchymal Study Group. *J Clin Oncol*. 2007; **25**(7): 837-844.

130. Sampson, J.H., et al., Poor drug distribution as a possible explanation for the results of the PRECISE trial. *J Neurosurg*. 2010; **113**(2): 301-309.

131. Mueller, S., et al., Effect of imaging and catheter characteristics on clinical outcome for patients in the PRECISE study. *J Neurooncol*. 2011; **101**(2): 267-277.

132. Brady, M.L., et al., In vivo performance of a microfabricated catheter for intraparenchymal delivery. *J Neurosci Meth.* 2014; **229**: 76-83.

133. Gill, T., et al., In vitro and in vivo testing of a novel recessed-step catheter for reflux-free convection-enhanced drug delivery to the brain. *J Neurosci Meth.* 2013; **219**(1): 1-9.

134. Seunguk, O., et al., Improved distribution of small molecules and viral vectors in the murine brain using a hollow fiber catheter. *J Neurosurg*. 2007; **107**(3): 568-577.

135. Olson, J.J., et al., Assessment of a balloon-tipped catheter modified for intracerebral convection-enhanced delivery. *J Neurooncol*. 2008; **89**(2): 159-168.

136. Lonser, R.R., et al., Convection-enhanced delivery to the central nervous system. *J Neurosurg*. 2015; **122**(3): 697-706.

137. Schwartz, H.S. and D.M. Spengler, Needle tract recurrences after closed biopsy for sarcoma: three cases and review of the literature. *Annals of surgical oncology*. 1997; **4**(3): 228-236.

138. Denton, K.J., et al., Secondary tumour deposits in needle biopsy tracks: an underestimated risk? *Journal of clinical pathology*. 1990; **43**(1): 83.

139. Krauze, M.T., et al., Reflux-free cannula for convection-enhanced high-speed delivery of therapeutic agents. *J Neurosurg*. 2005; **103**(5): 923-929.

140. Vazquez, L.C., et al., Polymer-coated cannulas for the reduction of backflow during intraparenchymal infusions. *J Mater Sci Mater Med.* 2012; **23**(8): 2037-2046.

141. Yin, D., J. Forsayeth, and K.S. Bankiewicz, Optimized cannula design and placement for convection-enhanced delivery in rat striatum. *J Neurosci Meth*. 2010; **187**(1): 46-51.

142. Mut, M., et al., Cintredekin besudotox in treatment of malignant glioma. *Expert Opin Biol Th*. 2008; **8**(6): 805-812.

143. Tocagen, *A Phase 1 Ascending Dose Trial of the Safety and Tolerability of Toca 511 in Patients With Recurrent High Grade Glioma*, in *In: ClinicalTrials.gov [Internet]*. 2010, National Library of Medicine (US). NLM Identifier: NCT01156584: Bethesda (MD).

144. Vogelbaum, M.A., *A Pilot Trial of Intraparenchymally-Administered Topotecan Using Convection-Enhanced Delivery (CED) in Patients With Suspected Recurrent/Progressive WHO Grade III or IV (High Grade) Glioma Requiring Stereotactic Biopsy*, in *In: ClinicalTrials.gov [Internet]*. 2014, National Library of Medicine (US). NLM Indentifier: NCT02278510: Bethesda (MD).

145. Vogelbaum, M.A., et al., First-in-human evaluation of the Cleveland Multiport Catheter for convection-enhanced delivery of topotecan in recurrent high-grade glioma: results of pilot trial 1. *J Neurosurg*. 2018: 1-10.

146. Barua, N.U., et al., A novel implantable catheter system with transcutaneous port for intermitten convection-enhanced delivery of carboplatin for recurrent glioblastoma. *Drug Delivery*. 2016; **23**(1): 167-173.

147. Debinski, W., et al., New agents for targeting of IL-13RA2 expressed in primary human and canine brain tumors. *PLoS One*. 2013; **8**(10): e77719.

148. Varenika, V., et al., Detection of infusate leakage in the brain using real-time imaging of convection-enhanced delivery. *J Neurosurg*. 2008; **109**: 874-880.

149. Andriani, R.T., *Design and Validation of Medical Devices for Photothermally Augmented Treatments*. 2014, Virginia Tech: Blacksburg (VA).

150. Elenes, E.Y. and C.G. Rylander, Maximizing Local Access to Therapeutic Deliveries in Glioblastoma. Part II: Arborizing Catheter for Convection-Enhanced Delivery in Tissue Phantoms, in S. De Vleeschouwer, Editor. *Glioblastoma*: Brisbane (AU); 2017.

151. Fiandaca, M.S., et al., Image-guided convection-enhanced delivery platform in the treatment of neurological diseases. *Neurotherapeutics*. 2008; **5**(1): 123-127

152. Gill, H.S. and M.R. Prausnitz, Does Needle Size Matter? *Journal of Diabetes Science and Technology*. 2007; **1**(5): 725-729.

153. Cormier, M., et al., Transdermal delivery of desmopressin using a coated microneedle array patch system. *J Control Release*. 2004; **97**(3): 503-511.

154. Kaushik, S., et al., Lack of Pain Associated with Microfabricated Microneedles. *Anesth Analg*. 2001; **92**: 502-504.

155. Jiang, J., et al., Intrascleral drug delivery to the eye using hollow microneedles. *Pharm Res*. 2009; **26**(2): 395-403.

156. Hood, R.L., et al. *Augmenting convection-enhanced delivery through simultaneous co-delivery of fluids and laser energy with a fiberoptic microneedle device*. in *SPIE BiOS*. 2013. International Society for Optics and Photonics.

157. Hood, R.L., et al., Fiberoptic microneedle device facilitates volumetric infusate dispersion during convection-enhanced delivery in the brain. *Lasers Surg Med*. 2013; **45**(7): 418-426.

158. Morrison, P.F., et al., Focal delivery during direct infusion to brain: role of flow rate, catheter diameter, and tissue mechanics. *Am J Physiol*. 1999; **46**: R1218-R1229.

159. Chen, M.Y., et al., Variables affecting convection-enhanced delivery to the striatum: a systematic examination of rate of infusion, cannula size, infusate concentration, and tissue–cannula sealing time. *Journal of Neurosurgery*. 1999; **90**: 315-320.

160. Hood, R.L., et al., Effects of Microneedle Design Parameters on Hydraulic Resistance. *J Med Device*. 2011; **5**(3): 31012-31016.

161. Roxhed, N., et al., Painless Drug Delivery Through Microneedle-Based Transdermal Patches Featuring Active Infusion. *IEEE T BME*. 2008; **55**(3): 1063-1071.

162. Martanto, W., et al., Transdermal Delviery of Insulin Using Microneedles *in Vivo*. *Pharm Res*. 2004; **21**(6): 947-952.

163. Otsu, N., A Threshold Selection Method from Gray-Level Histograms. *IEEE T Sys Man Cyb*. 1979; **9**(1): 62-66.

164. Sabliov, C.M., et al., Image Processing Method to Determine Surface Area and Volume of Axi-Symmetric Agricultural Products. *Int J Food Prop*. 2002; **5**(3): 641-653.

165. Zhang, X.Y., et al., Interstitial hydraulic conductivity in a fibrosarcoma. *am J Physiol Heart Circ Physiol*. 2000; **279**: H2726-H2734.

166. Basser, P.J., Interstitial Pressure, Volume, and Flow during Infusion into the Brain Tissue. *Microvascular Ressearch*. 1992; **44**: 143-165.

167. Barry, S.I. and G.K. Aldis, Flow-induced Deformation from Pressurized Cavities in Absorbing Porous Tissues. *Bulletin of Mathematical Biology*. 1992; **54**(6): 977-997.

168. Chen, X. and M. Sarntinoranont, Biphasic finite element model of solute transport for direct infusion into nervous tissue. *Ann Biomed Eng*. 2007; **35**(12): 2145-2158.

169. Linninger, A.A., et al., Computational methods for predicting drug transport in anisotropic and heterogeneous brain tissue. *J Biomech*. 2008; **41**(10): 2176-2187.

170. Valles, F., et al., Anatomic compression caused by high-volume convection-enhanced delivery to the brain. *Neurosurgery*. 2009; **65**(3): 579-585.

171. Garcia, J.J. and J.H. Smith, A biphasic hyperelastic model for the analysis of fluid and mass transport in brain tissue. *Ann Biomed Eng*. 2009; **37**(2): 375-386.

172. Netti, P.A. and F. Travascio, Coupled Macromolecular Transport and Gel Mechanics: Poroviscoelastic Approach. *Bioengineering, Food and Natural Products*. 2003; **49**(6): 1580-1596.

173. Smith, J.H. and J.J. Garcia, A nonlinear biphasic model of flow-controlled infusion in brain: fluid transport and tissue deformation analyses. *J Biomech*. 2009; **42**(13): 2017-2025.

174. Smith, J.H. and J.J. Garcia, A nonlinear biphasic model of flow-controlled infusions in brain: mass transport analyses. *J Biomech*. 2011; **44**(3): 524-531.

175. Smith, J.H., K.A. Starkweather, and J.J. Garcia, Implications of transvascular fluid exchange in nonlinear, biphasic analyses of flow-controlled infusion in brain. *Bull Math Biol*. 2012; **74**(4): 881-907.

176. Mauck, R.L., C.T. Hung, and G.A. Ateshian, Modeling of Neutral Solute Transport in a Dynamically Loaded Porous Permeable Gel: Implications for Articular Cartilage Biosynthesis and Tissue Engineering. *J Biomech Eng*. 2003; **125**(5): 602-614.

177. Ateshian, G.A., M. Likhitpanichkul, and C.T. Hung, A mixture theory analysis for passive transport in osmotic loading of cells. *J Biomech*. 2006; **39**(3): 464-475.

178. Ateshian, G.A., et al., Finite Element Implementation of Mechanochemical Phenomena in Neutral Deformable Porous Media Under Finite Deformation. *Journal of Biomechanical Engineering*. 2011; **133**: 0810051-08100512.

179. Maas, S., et al., *FEBio: Finite Elements for Biomechanics Theory Manual*. 2015.

180. Gu, W.Y., W.M. Lai, and V.C. Mow, A Mixture Theory for Charged-Hydrated Soft Tissues Containing Multi-electrolytes: Passive Transport and Swelling Behaviors. *J Biomech Eng*. 1998; **120**: 169-180.

181. Maas, S., et al., FEBio: Finite Elements for Biomechanics. *Journal of Biomechanical Engineering*. 2012; **134**: 0110051-01100510.

182. Normand, V., et al., New insights into agarose gel mechanical properties. *Biomacromolecules*. 2000; **1**: 730-738.

183. Pluen, A., et al., Diffusion of macromolecules in agarose gels: comparison of linear and globular configurations. *Biophysical Journal*. 1999; **77**: 542-552.

184. Holmes, M.H. and V.C. Mow, The nonlinear characteristics of soft gels and hydrated connective tissues in ultrafiltration. *Journal of Biomechanics*. 1990; **23**(11): 1145-1156.

185. Tao, L. and C. Nicholson, Diffusion of Albumins in Rat Cortical Slices and Relevance to Volume Transmission. *Neuroscience*. 1996; **75**(3): 839-847.

186. Rausch, M.K. and J.D. Humphrey, A Computational Model of the Biochemomechanics of an Evolving Occlusive Thrombus. *Journal of Elasticity*. 2017; **129**(1-2): 125-144.

187. Chittiboina, P., et al., Magnetic resonance imaging properties of convective delivery in diffuse intrinsic pontine gliomas. *J Neurosurg Pediatr*. 2014; **13**(3): 276-282.

188. Polivka, J., Jr., et al., Advances in Experimental Targeted Therapy and Immunotherapy for Patients with Glioblastoma Multiforme. *Anticancer Res*. 2017; **37**(1): 21-33.

189. Touat, M., et al., Glioblastoma targeted therapy: updated approaches from recent biological insights. *Ann Oncol*. 2017; **28**(7): 1457-1472.

190. Xu, Y.Y., et al., Development of targeted therapies in treatment of glioblastoma. *Cancer Biol Med*. 2015; **12**(3): 223-237.

191. Chen, Z.J., et al., Intraparenchymal Drug Delivery via Positive-Pressure Infusion: Experimental and Modeling Studies of Poroelasticity in Brain Phantom Gels. *IEEE Trans Biomed Eng*. 2002; **49**(2): 85-96.

192. Chen, Z.J., et al., A realistic brain tissue phantom for intraparenchymal infusion studies. . *J Neurosurg*. 2004; **101**: 314-322.

193. Debinski, W., W. Priebe, and S.B. Tatter, Maximizing Local Access to Therapeutic Deliveries in Glioblastoma. Part I: Targeted Cytotoxic Therapy, in S. De Vleeschouwer, Editor. *Glioblastoma*. Codon Publications: Brisbane (AU); 2017: 341-358.

194. Hood, R.L., et al., Characterizing Thermal Augmentation of Convection-Enhanced Drug Delivery with the Fiberoptic Microneedle Device. *Engineering*. 2015; **1**(3): 344-350.

195. Dickinson, P.J., et al., Canine model of convection-enhanced delivery of liposomes containing CPT-11 monitored with real-time magnetic resonance imaging: laboratory investigation. *J Neurosurg*. 2008; **108**(5): 989-998.

196. Summers, B.A., J.F. Cummings, and A. De Lahunta, Tumors of the central nervous system. *Veterinary Neuropathology*. Mosby-Year Book Publishers, Inc.: St. Louis, MO; 1995: 364.

197. Koestner, A. and R.J. Higgins, Tumors of Domestic Animals, in D.J. Meuten, Editor. *Tumors of the nervous system*. Iowa State University Press: Ames, IA; 2002: 697.

198. LeCouteur, R.A., Tumors of the nervous system, in S.J. Withrow and E.G. MacEwen, Editors. *Small Animal Clinical Oncology*. WB Saunders Co: Philadelphia, PA; 2001.